



# Cardiovascular X-ray Imaging: Physics, Equipment, and Techniques

*Arnold R. Cowen*

## **11.1 Introduction – 149**

### **11.2 Reprise of X-Ray Physics – 149**

- 11.2.1 What Are X-Rays? – 149
- 11.2.2 How Are X-Rays Produced? – 150
- 11.2.3 X-Ray Spectrum – 151
- 11.2.4 Rotating Anode X-Ray Tube – 151

### **11.3 Interaction of X-Rays with Matter – 152**

- 11.3.1 Physics of X-Ray Interactions – 152
- 11.3.2 Photoelectric Absorption – 153
- 11.3.3 Compton Scatter – 153
- 11.3.4 Beer–Lambert’s Law (Exponential Attenuation) – 153

### **11.4 X-Ray Image Formation – 154**

- 11.4.1 Iodine Signal – 154
- 11.4.2 Subject X-Ray Contrast – 155
- 11.4.3 X-Ray Scatter and Contrast Degradation – 157
- 11.4.4 Antiscatter Grid – 157
- 11.4.5 Imaging Geometry – 158

### **11.5 Signal-to-Noise Ratio Description of X-Ray Images – 159**

- 11.5.1 Definition of Signal-to-Noise Ratio – 160
- 11.5.2 Detail Signal-to-Noise Ratio – 160

### **11.6 Digital X-Ray Imaging – 161**

- 11.6.1 The Digital Image – 161
- 11.6.2 Digital X-Ray Imaging System – 163

11.6.3	Digital Subtraction Angiography – 165
11.6.4	Rotational Angiography – 166
11.6.5	Three-Dimensional Reconstruction Imaging – 168
<b>11.7</b>	<b>X-Ray Equipment – 168</b>
11.7.1	Direct Heat Removal from the Anode – 168
11.7.2	Grid-Controlled X-Ray Source – 170
11.7.3	High-Frequency Power Generator – 170
11.7.4	Spectral Filter – 171
11.7.5	Automatic Dose Rate Control – 173
<b>11.8</b>	<b>Dynamic X-Ray Image Detectors – 175</b>
11.8.1	X-Ray Image Intensifier Television System – 175
11.8.2	Solid-State X-Ray Image Detector – 175
11.8.3	Indirect-Conversion Dynamic Flat-Panel Detector – 176
<b>11.9</b>	<b>Image Quality of Dynamic Flat-Panel Detectors – 178</b>
11.9.1	Dynamic Range – 178
11.9.2	Geometry and Vignetting – 179
11.9.3	Veiling Glare (Low-Frequency Drop) – 179
11.9.4	Spatial Resolution – 180
11.9.5	Lag and Memory Effect – 182
11.9.6	Detective Quantum Efficiency – 183
<b>11.10</b>	<b>Digital Image Processing – 185</b>
11.10.1	Generic Image Enhancement – 186
11.10.2	Targeted Image Enhancement – 187
11.10.3	Three-Dimensional Enhanced Imaging – 188
<b>11.11</b>	<b>Flat-Screen Displays – 190</b>
<b>11.12</b>	<b>Technique Considerations – 191</b>
11.12.1	Projections – 192
11.12.2	Field of View and Magnification – 192
11.12.3	Zoom Mode and Detail Resolution – 192
11.12.4	Spectral Filters and Wedge Filters – 192
11.12.5	Motion Artifacts and Positioning – 193
11.12.6	Recommended Approach – 193
11.12.7	Case Documentation – 193
11.12.8	Contrast Media – 194
	<b>References – 195</b>

## 11.1 Introduction

---

Cardiovascular diagnosis and interventional therapy have a fundamental need for dynamic X-ray images of suitable quality. These images are typically used to visualize blood flow, in order to diagnose diseased vessel segments, stenoses, aneurysms, etc. It is an unhelpful (but currently unavoidable) characteristic of standard-projection imaging with X-rays that blood is indistinguishable from the soft-tissue structures in which the vessel is embedded. Therefore, visualization of a blood vessel demands the administration of an artificial contrast agent, normally an iodine-loaded solution. The contrast medium is injected into the vessel to mix with the blood and provide the absorption of the X-ray beam needed to depict the vessel lumen and therefore any associated disease. Furthermore X-ray image guidance and visualization are indispensable in current interventional practice. Therefore, dynamic X-ray imaging is required to image devices such as guide wires, catheters, balloons, stents, coils, cutters, or any other items on a burgeoning list of interventional tools. In order to minimize any consequent radiation risks, the imaging must be performed at dose levels consistent with the ALARA (as low as reasonably achievable) principle, at all times.

Real-time dynamic X-ray imaging at low dose rates, typically for the purpose of guiding a clinical procedure, is known as *fluoroscopy*. Historically, in this role, fluoroscopy has been accepted to be an impermanent imaging medium, requiring no storage of images for later review. The permanent recording of images—for example, to document clinical findings—has normally relied upon the acquisition (and storage) of dynamic image sequences of superior quality to fluoroscopy. Image acquisition in this form therefore has to be performed at significantly higher radiation dose rates than in fluoroscopy to ensure that this is achieved. At various times in the past, serial images were recorded on radiographic film, small-format film, cine film, or even video tape (as clinically appropriate). Today, *all* dynamic X-ray images, both in fluoroscopy and serial acquisition, are acquired in digital form using computerized X-ray imaging equipment. Hence, terms such as *digital fluoroscopy* and *digital acquisition* are now used to differentiate these dynamic X-ray imaging modalities. The high-speed acquisition of images

in cardiology examinations is often referred to as *digital cine acquisition*.

This chapter aims to provide the practicing interventionalist with an update on the physical and technical aspects of prevailing cardiovascular X-ray imaging equipment. Special attention is paid to the new generation of (solid-state) image detectors, their physical characteristics, and how they can augment clinical service. The aim is to provide the interventionalist with a cogent understanding of these influential technologies. Such a working knowledge can have many benefits. A better understanding of these physical and technical principles should lead to fuller utilization of equipment resources and facilities. For example, the interventionalist should be empowered to optimize fluoroscopic and image acquisition strategies. It should also add to a better appreciation of how equipment utilization impacts on radiation safety, potentially to the benefit of both patients and staff. This knowledge may also contribute to better-informed selection of digital X-ray imaging equipment during the purchase process. This should aid in future-proofing the selection of equipment against continuing advances in digital imaging technologies and new developments in interventional techniques, which will no doubt require even more sophisticated X-ray image guidance.

## 11.2 Reprise of X-Ray Physics

---

Before considering cardiovascular imaging equipment in detail, this section reprises the basic physics of X-rays and their production for medical use. Building upon this, the sections that follow go on to explore how X-rays interact with matter (tissue) and in turn how the basic X-ray image is formed and then recorded using a suitable detector. For further background, the interested reader is referred to the many excellent textbooks on the physics of medical X-ray imaging (e.g., [1, 2]).

### 11.2.1 What Are X-Rays?

---

To cut a long story short, X-rays are a form of electromagnetic radiation, like many other more familiar physical phenomena such as visible light, ultraviolet light, infrared radiation, microwaves, and radio waves. X-rays are subject to the

vagaries of quantum physics and therefore exhibit the properties of (electromagnetic) waves while at the same time behaving like particles. To date, the potentially very effectual wave-like properties of X-rays [3] are unrealized in clinical routine and therefore are not discussed further here. The X-ray beam used in medical X-ray imaging is better described as a stream (deluge) of individual packets of X-ray energy or X-ray photons. If the temporal frequency or wavelength of the X-ray is known, the equivalent X-ray photon energy ( $\varepsilon_p$ ) can be calculated using the simple equation:

$$\varepsilon_p = h \cdot f = h \cdot c / \lambda$$

where:

$f$  is the temporal frequency (in cycles  $s^{-1}$ )

$\lambda$  is the wavelength

$h$  is Planck's constant ( $\sim 6.626 \times 10^{-34}$  J s)

$c$  is the speed of light ( $3 \times 10^8$  m  $s^{-1}$  in vacuo)

X-rays share many physical properties with the electromagnetic phenomena listed above, but have one notable distinguishing feature: X-rays have much greater photon energy. An X-ray photon is typically several tens of thousands of times more energetic than a light photon. Therefore, unlike light, an X-ray photon has the potential to penetrate a comparatively large thickness of matter, such as the human body. On the other hand, the X-ray photon also has the capacity to interact with an atom that makes up the tissue, via one of the mechanisms described in ► Sect. 11.3. When such an interaction occurs, the X-ray photon delivers whole or part of its energy to the tissue. X-ray photons (like the similarly energetic  $\gamma$ -rays) have sufficient energy to ionize an atom; therefore, not surprisingly, X-rays are said to be *ionizing radiation*. Absorption of X-ray energy in body tissue results in the ionization of biomolecules, which can result in cell damage or death. The resultant biological risk increases with the magnitude of the X-ray dose delivered (and hence the degree of ionization produced). Radiation dose and its measurement are discussed in ► Chap. 15.

## 11.2.2 How Are X-Rays Produced?

In medical imaging, X-rays are produced by bombarding a high-atomic-number ( $Z$ ) metal target with a stream of high-speed electrons. Tungsten (W) ( $Z = 74$ ) is the target metal used

in cardiovascular X-ray imaging; in practice, tungsten is alloyed with a small quantity ( $\sim 5\%$ ) of rhenium (Re) to increase target longevity. Free electrons are derived by heating a filament coil (again made of tungsten) by passing an electric current through it; this process is known as *thermionic emission*. The number of electrons freed and therefore the intensity of the X-ray beam produced are controlled by adjusting the filament current and thereby the filament temperature. The intensity of the X-ray beam is defined by the X-ray energy per unit area and unit time passing a defined plane in the beam. The application of a suitably high voltage (HV) between the (–) cathode filament and the (+) tungsten anode target, typically in the range of a 50–150 kilovolt (kV) peak (kVp), accelerates the electrons up to a kinetic energy suitable for producing X-rays. The peak value of the accelerating voltage (kVp) that is applied controls the energy content of the X-ray beam and therefore its propensity to penetrate the thickness of the body. At the same time, however, kVp also affects the intensity of the X-ray beam. The electrical current that flows from the cathode to the anode as a result of applying the accelerating voltage is the tube current in milliamperes (mA). For a given kVp, the X-ray beam intensity is proportional to the mA. Electrons accelerated across the X-ray tube collide with tungsten atoms on the anode surface. X-rays are produced via one of two physical mechanisms: bremsstrahlung and characteristic X-ray production. Production of X-rays by these two mechanisms is signally inefficient, viz.,  $<1\%$  of the electrical energy used is converted to X-rays. The balance of electrical energy ( $>99\%$ ) is converted unproductively to heat. The management and disposal of heat remains one of the main constraints of modern X-ray tube design, and this is discussed in ► Sect. 11.7.1.

Bremsstrahlung production occurs when a high-speed electron collides with the strong (+) coulomb field surrounding the nucleus of a target atom. The energy of the resulting X-ray photon depends upon the proximity of the collision to the nucleus itself (viz., the local strength of the electric field). A consequence of the bremsstrahlung mechanism is that during an exposure, a wide range of X-ray photon energies is produced.

Characteristic X-ray production occurs when an incoming electron collides with a K-shell electron; the K-shell contains the electrons that are most tightly bound to the nucleus. The

resulting ejection of a K-shell electron produces a highly unstable atom. This is promptly followed by the transition of an electron from an L- or M-shell to fill the K-shell vacancy. As a result, the atom relaxes to a much lower energy state, emitting the excess energy in the form of an X-ray photon. This X-ray photon has a characteristic energy defined by the energy difference between the L- and K-shells or the M- and K-shells, as appropriate. Characteristic X-ray emission for a tungsten anode target actually occurs at four specific energies, in two groupings in the range of 57–70 keV (approximately). In routine cardiovascular imaging, characteristic X-ray production is of secondary importance to the bremsstrahlung production.

### 11.2.3 X-Ray Spectrum

The physical characteristics of an X-ray beam can be conveniently described as a spectrum, which represents the intensity of the beam at each contributing X-ray photon energy. The exact form of the X-ray spectrum is principally dependent upon the electrical characteristics of the exposure, the tube current (mA) and the peak tube voltage (kVp) settings. A change in mA produces a proportionate change in the intensity (height) of the X-ray spectrum, but otherwise, no detailed change in spectral shape occurs. On the other hand, an increase in kVp has a more powerful effect on the X-ray spectrum, materially changing both the intensity of the X-ray beam and its energy content (hence, spectral shape). The maximum photon energy of the X-ray spectrum is defined by the kVp applied across the X-ray tube.

Spectra produced by a tungsten anode X-ray tube are polyenergetic, as shown in **Fig. 11.1**; this figure includes three computed X-ray spectra for exposures at 60 kVp (red), 80 kVp (blue), and 100 kVp (green), respectively. The 60 kVp spectrum describes a continuous bremsstrahlung envelope up to a maximum photon energy of 60 keV. An exposure at 80 kVp produces a spectrum describing a broader bremsstrahlung envelope up to a maximum photon energy of 80 keV; superimposed upon this are the X-ray emission lines of tungsten (at their characteristic energies). By comparison, the 100 kVp spectrum contains X-ray photons up to the higher maximum energy of 100 keV. This increases the complement of

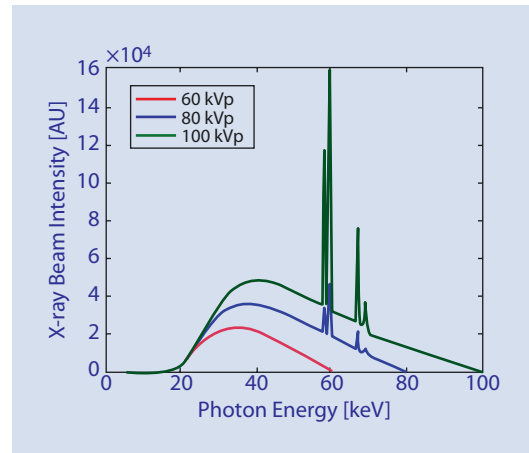


**Fig. 11.1** X-ray spectra produced by a tungsten anode X-ray tube (3.5 mm aluminum filter): exposures at 60 kVp (red), 80 kVp (blue), and 100 kVp (green). kVp peak kilovoltage. (See «Acknowledgments»)

high-energy X-ray photons, making the X-ray beam more penetrative.

### 11.2.4 Rotating Anode X-Ray Tube

The production of X-rays takes place inside an evacuated metal (previously glass) enclosure, which houses the cathode filament (in its focusing block), the rotating anode, and insulating fixtures. In metal enclosures, the insulating fixtures are often made of ceramic material. The anode target comprises a disc-shaped metal structure attached to a rotor assembly. Around the anode disc is the circumferential track, which is bombarded with electrons during the X-ray exposure. The cathode block is mounted off-axis to accurately align the filament with this track. Anode disks have a multilayer (or composite) construction, with the actual tungsten (target) layer superimposed upon a molybdenum (Mo) alloy substrate. The anode disk is often backed by a thick layer of graphite to increase the heat storage capacity and aid heat dissipation via thermal radiation. During an X-ray exposure, the anode is typically rotating at 3000 revolutions per minute (but this rate can be significantly greater). Some anodes contain a set of narrow radial slots to condition the anode against the mechanical stress of repeated heating and cooling cycles. A beryllium (Be) window is built into the metal envelope to provide a low-attenuation exit port for the X-ray beam. The

X-ray tube is housed inside an earthed metal shield and surrounded by oil. The oil not only acts as an electrical insulator but also aids heat transfer from the tube to the shield via convection. Except for the region adjacent to the exit port of the X-ray tube, the shield is lined with lead (Pb) foil to prevent leakage of X-rays. Heat sensors are often used to monitor the temperature of the oil to ensure safe operation of the X-ray tube.

During the X-ray exposure, electrons flow across the tube and impact upon the (rotating) anode. The instantaneous impact of electrons occurs over a rectangular zone on the anode target known as the *actual X-ray focus* (or *line X-ray focus*); this represents the nascent source of X-rays. With respect to the emerging beam, the projected line X-ray focus is foreshortened by the angled surface of the anode target. As a result, the effective focus or focal spot, which contributes to X-ray image formation, has (roughly) a square format. The anode target is typically beveled at an angle of between 8° and 12°. A shallower anode angle provides greater foreshortening of the line focus, and hence a smaller effective focal spot is realized. At the same time, however, the shallow anode angle limits the available X-ray field coverage. In cardiac imaging, which requires restricted anatomical coverage, this is usually not a problem. On the other hand, vascular imaging often requires coverage of quite large body sections. Therefore, in general, vascular applications favor the use of a larger anode target angle to increase field coverage. To a first approximation at a given distance from the X-ray focal spot, the field of X-rays incident upon the patient is approximately uniform. In practice, there is a 20–30% reduction in X-ray intensity across the beam in the cathode–anode direction due to the *anode heel effect*. This effect is ignored here, as modern image detectors can compensate for this.

The size and shape of the effective focal spot influences the spatial resolution of the X-ray image that is formed. The finite size of the X-ray source potentially represents a source of geometrical blur (unsharpness) in the recorded images. Ideally for sharp (high-resolution) X-ray images, the effective focal spot should be as small as possible. Unfortunately, there is a limit to the degree to which the focal spot can be reduced in area. This limit is defined by the maximum instantaneous power (defined by the product  $P = kVp \times mA$ ) that can be tolerated by the anode target. Excessive

power delivery will overheat the anode surface and cause permanent damage. X-ray tubes typically offer two or three X-ray focal spot selections, each with a different size and power capability. In a bifocus X-ray tube, the smaller *fine focus* typically has a size in the range of 0.3–0.5 mm, while the larger more powerful *broad focus* is typically 0.6–1 mm in size. Associated with each focal spot size selection is a filament of matched scale, smaller-gauge filaments being used with the fine focus and more robust filaments with the broad focus. The fine focus is commonly reserved for use in fluoroscopy applications, which operate at lower levels of X-ray tube current. For adult patients, the X-ray broad focus is normally reserved for use in serial image acquisition. However, the fine focus may be used in pediatric image acquisition. Some modern cardiovascular X-ray imaging systems automatically select the optimum X-ray focal spot size, depending upon the patient size, exposure requirements, power limits, etc.

## 11.3 Interaction of X-Rays with Matter

### 11.3.1 Physics of X-Ray Interactions

Individual X-ray photons that are incident upon the patient during an X-ray exposure can subsequently undergo a variety of different interaction histories. It should be noted that the mechanisms defining these interactions are probabilistic in nature. For example, a small but important complement of the incident X-ray photons can travel unperturbed through a thickness (of even many centimeters) of tissue. These photons exit the patient and contribute to the primary X-ray image, which is recorded by the image detector. Much more commonly, an X-ray photon will interact with an atom in the tissue and be removed from the X-ray beam either completely or partially. Over the range of energies used in cardiovascular imaging, X-ray photons can interact via one of two mechanisms: photoelectric absorption (PA) and Compton scatter (CS), which have distinctive properties. The combined effect of these two interaction mechanisms reduces the intensity of the X-ray beam as it penetrates increasing thicknesses of tissue. This process is known as *X-ray beam attenuation*. The attenuation produced by a material is described by the linear X-ray



attenuation coefficient ( $\mu$ ). The greater the value of  $\mu$ , the more strongly an X-ray beam will be attenuated by a given thickness of material.

### 11.3.2 Photoelectric Absorption

An interaction via the PA mechanism occurs when an incoming X-ray photon is fully absorbed by a tightly bound orbital electron in an atom. This results in the ejection of a photoelectron, which travels through adjacent tissue, depositing its kinetic energy via ionization. The attenuation of an X-ray beam due to the PA interaction ( $\mu_{\text{PA}}$ ) strongly increases with the mass density ( $\rho$ ) and the atomic number ( $Z$ ) of the attenuating material, but falls rapidly with increasing X-ray photon energy ( $\epsilon_p$ ), viz.:

$$\mu_{\text{PA}} \propto \rho \cdot Z^3 / \epsilon_p^3$$

The PA interaction mechanism contributes strongly to X-ray beam attenuation for tissue material with a higher  $Z$  value, such as bone (typical mean  $Z = \sim 14$ ), but particularly so for iodine ( $Z = 53$ ), which is used in most cardiovascular X-ray contrast media. By comparison, the atomic number of soft tissue is much lower (typical mean  $Z = \sim 7$ ). At low X-ray photon energies, PA is the dominant interaction mechanism, but its influence falls rapidly with increasing energy. The absorption of X-ray photon energy in tissue via the PA mechanism is a significant contributor of radiation dose to the patient.

### 11.3.3 Compton Scatter

An interaction via the CS mechanism occurs when the incoming photon collides with a loosely bound (peripheral orbital) electron in an atom. This causes the electron to be ejected from the atom, accompanied by the emission of a secondary X-ray photon of lower energy. Attenuation of an X-ray beam via the CS mechanism ( $\mu_{\text{CS}}$ ) increases with the tissue mass density and the ratio of the atomic number ( $Z$ ) to the atomic weight ( $A$ ) of the tissue, but falls (slowly) with X-ray photon energy, viz.:

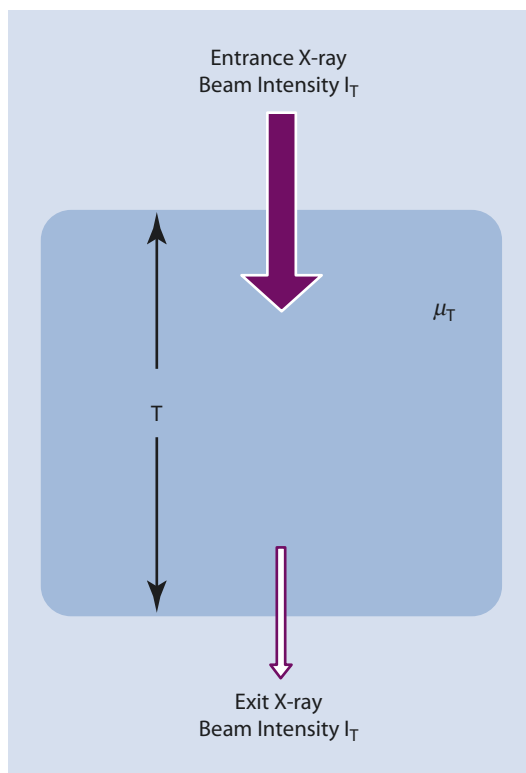
$$\mu_{\text{CS}} \propto \rho \cdot (Z/A) / \epsilon_p^Z$$

For most elements, the ratio  $Z/A$  is approximately constant, having a value of  $\sim 0.5$ . Uniquely, however, hydrogen has a  $Z/A$  value of unity; this enhances the sensitivity of the CS mechanism to hydrogen-loaded materials, notably water and hence soft tissue. Indeed, CS is the dominant X-ray interaction process in soft tissue, but is less influential in bone. X-ray attenuation due to CS falls much less rapidly with increasing photon energy than for PA, and therefore CS tends to dominate X-ray image formation at increasing photon energies. The dynamics of the CS process are governed by the laws of momentum and energy conservation, but these details need not trouble the reader. It is important however to note that the secondary X-ray photon is emitted in an arbitrary (random) direction with respect to the primary photon and is said to be *scattered*. This X-ray photon can be scattered at any angle, from a slight deflection through to full back scatter (viz., over  $180^\circ$ ). Again, subsequent absorption of the scattered photon in tissue will contribute to the patient dose. Should the scattered X-ray photon exit the patient altogether, it may then go on to irradiate clinical staff who are in close proximity.

### 11.3.4 Beer–Lambert’s Law (Exponential Attenuation)

The physical description of the attenuation of an X-ray beam by tissue can be more easily appreciated by first considering a simple phantom model, rather than the much more complex problem of a patient. This phantom model assumes that parallel ray geometry is applicable (viz., divergence of the X-ray beam does not occur), that the X-ray beam is monoenergetic, and that X-ray scatter can be ignored. Making these simplifying assumptions unburdens the analysis but still provides some useful insights. Such a phantom model (see [Fig. 11.2](#)) typically comprises a given thickness  $T$  of tissue of linear X-ray attenuation  $\mu_T$  (where  $\mu_T$  results from the sum of the PA and CS interactions, therefore  $\mu_T = \mu_{\text{PA}} + \mu_{\text{CS}}$ ). If the intensity of the X-ray beam incident on the phantom is  $I$ , the resulting exit beam intensity  $I_T$  is predicted by Beer–Lambert’s law, viz.:

$$I_T = I \exp(-\mu_T \cdot T)$$



■ **Fig. 11.2** Phantom model illustrating the attenuation of an X-ray beam by thickness of matter (tissue)

where  $\mu_T$  (for soft tissue) typically has a value of  $\sim 0.22 \text{ cm}^{-1}$ ; however, the value does vary with X-ray beam energy. Exponential attenuation describes a nonlinear function, where equal increments in thickness of a material produce disproportionate reductions in the intensity of the transmitted X-ray beam.

Rearranging this equation shows that if the values of  $I$  and  $\mu_T$  are known, then the effective thickness of the body section can be estimated by measuring the transmitted X-ray intensity ( $I_T$ ) where:

$$T = (\log_e I / I_T) / \mu_T$$

This result can be used to estimate the equivalent water thickness of a body section. Computation of this parameter is often used by fluoroscopy automatic dose rate control systems to select X-ray exposure factors.

Another useful parameter that can be derived from Beer–Lambert’s law is the half-value thickness (HVT) of a material. The HVT of tissue (the thickness required to attenuate the X-ray beam by a factor of 2) can be estimated using the equation:

$$\text{HVT} = \log_e 2 / \mu_T = 0.693 / \mu_T$$

Under typical cardiovascular imaging conditions, the HVT of soft tissue is therefore  $\sim 3 \text{ cm}$ . In other words, adding an extra 15 cm thickness of soft tissue to a body section (say, in an overweight patient) would reduce the X-ray beam intensity not by a factor of 5 (from 15/3) but by the much larger factor of 32 (from  $2^5$ ). When recording images, this reduction in exit beam intensity would have to be balanced by a compensatory increase in patient radiation dose in order to re-establish the calibrated detector operating dose.

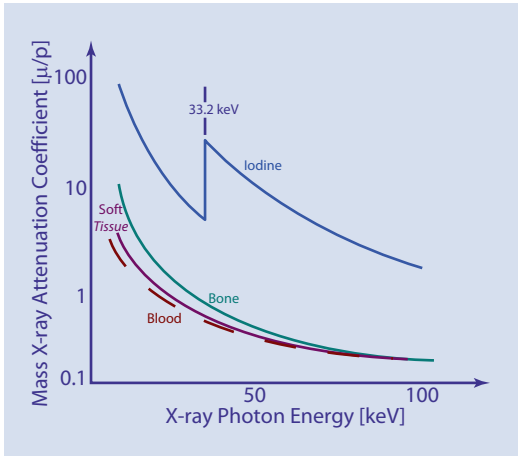
## 11.4 X-Ray Image Formation

A body section comprises a complex melange of differing tissue materials of varying thickness. Interaction of X-ray photons with such a body section results in a modulated (nonuniform) field of X-rays at the exit of the patient. The pattern of X-rays is defined by the distribution of tissue materials intercepting each ray through the body section. The modulated field of X-rays carries the information that can be recorded in the image. Because of these complexities of a patient, we again turn to a phantom model. Obviously imaging the simple phantom shown in ■ Fig. 11.2 would result in a featureless (uniform) X-ray image. The analysis of X-ray image formation becomes much more informative if a signal detail is included in the phantom. In other words, a specific *signal* with different X-ray attenuation characteristics to the background is considered.

### 11.4.1 Iodine Signal

In cardiovascular imaging, a signal is conveniently represented by a blood vessel opacified with iodinated contrast medium. The presence of the contrast medium causes stronger attenuation of the X-ray beam than the background tissue alone. The X-ray attenuation properties of iodine, soft tissue, blood, and bone are compared across the relevant X-ray photon energy range in ■ Fig. 11.3. Note that here the attenuation is expressed in terms of the mass X-ray attenuation coefficient ( $\mu/\rho$ ) (which is equal to the linear X-ray attenuation ( $\mu$ ) divided by the mass density ( $\rho$ )). Referring to this figure, we see that the





■ **Fig. 11.3** Mass X-ray attenuation of iodine (contrast medium), soft tissue, blood, and bone: variation of mass attenuation with X-ray photon energy

mass X-ray attenuation of blood and soft tissue is approximately the same, so it should come as no surprise that in projection imaging, arteries are indistinguishable from the surrounding soft tissue. On the other hand, if an iodinated X-ray contrast medium is injected into a blood vessel, the X-ray attenuation is markedly increased compared with surrounding soft tissue and bone. This is due to the very strong PA of iodine. X-ray attenuation by iodine is also influenced by the presence of a K-absorption edge in the relevant energy range. The K-edge enhances the absorption of X-ray photons with energies exceeding 33.2 keV and is another major contributor to X-ray image formation for iodinated contrast agents.

### 11.4.2 Subject X-Ray Contrast

Local variations in the primary X-ray beam intensity exiting a patient can be quantified in terms of *subject X-ray contrast*. To better understand this concept, let us refer to a phantom model that includes a signal feature—for example, a blood vessel of diameter  $d$  containing the iodinated contrast medium, as illustrated in ■ Fig. 11.4. This figure also shows the corresponding X-ray intensity profile across the background and behind the signal (iodinated blood vessel). The linear X-ray attenuation coefficient of the contrast medium mixed with blood is given by  $\mu_C$  (where  $\mu_C \gg \mu_T$ ). The X-ray beam intensity exiting the background tissue is given by:

$$I_T = I \exp(-(\mu_T \cdot T))$$

and in the shadow of the iodinated vessel:

$$\begin{aligned} I_C &= I \exp(-(\mu_T \cdot [T-d] + \mu_C \cdot d)) \\ &= I \exp(-(\mu_T \cdot T + [\mu_C - \mu_T] \cdot d)) \end{aligned}$$

The subject X-ray contrast  $C_X$  of the iodinated vessel can then be calculated using the equation:

$$C_X = (I_C - I_T) / I_T$$

Substituting for  $I_C$  and  $I_T$  from above gives:

$$\left[ C_X = \exp(-([\mu_C - \mu_T] \cdot d) - 1 \right]$$

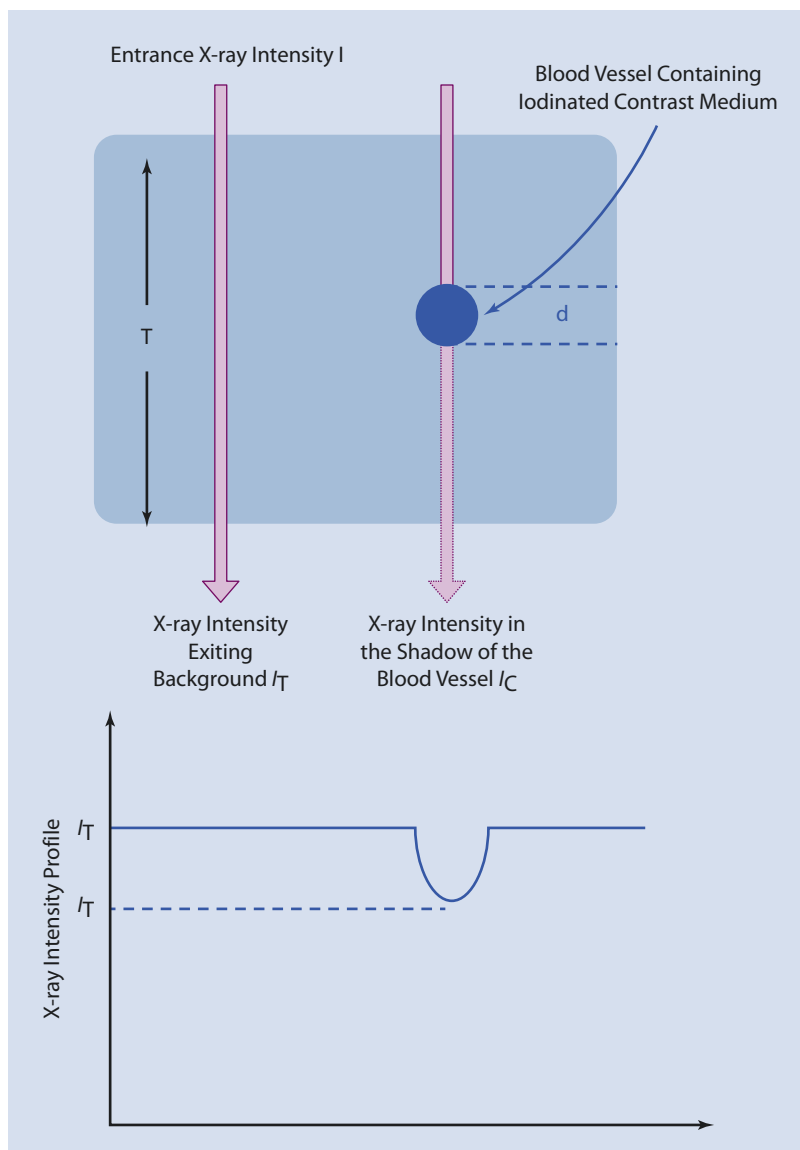
Assuming a modest level of subject X-ray contrast, viz.,  $(I_T - I_C) \ll I_T$ , the limiting result  $\{\exp. -x \rightarrow (1 - x), \text{ as } x \rightarrow 0\}$  can be used to simplify the analysis such that:

$$C_X \sim -([\mu_C - \mu_T] \cdot d)$$

This simple equation carries several interesting messages. First, the subject X-ray contrast of the opacified vessel is negative as  $\mu_C > \mu_T$  (note: this physical convention must not be confused with the clinical use of the terms *negative contrast medium* and *positive contrast medium*). The magnitude of the contrast is proportional to the difference in the values of the linear X-ray attenuation coefficient of the opacified vessel and the background tissue. This difference, and hence vessel visibility, can be enhanced by reducing the X-ray beam energy, typically by reducing the kVp. This inevitably comes at a cost of increased X-ray absorption in background tissue and hence an increased patient dose. Subject X-ray contrast is also proportional to the diameter (projected thickness) of the vessel. In other words, for the same level of iodine concentration, a larger-diameter vessel naturally produces greater subject contrast. Therefore, in principle, a reduced concentration of contrast medium may be suitable for imaging larger-diameter vessels. On the other hand, an increased concentration of contrast medium may be required to ensure adequate visualization of small-diameter vessels.

The X-ray attenuation of the iodinated blood vessel ( $\mu_C$ ) can be more fully described using an

Fig. 11.4 Phantom model including a signal feature (blood vessel)



equation that takes account of the properties of the contrast medium:

$$\mu_C = (\mu/\rho)_I \cdot X_I \cdot f$$

where:

$(\mu/\rho)_I$  describes the mass X-ray attenuation of iodine—this factor varies with X-ray beam energy, but typically has a value of  $\sim 15 \text{ cm}^2 \text{ gm}^{-1}$

$X_I$  defines the iodine concentration of the contrast medium—this varies with design and manufacture, but  $300 \text{ mg iodine ml}^{-1}$  is representative

$f$  is the fractional contrast medium content—this will vary with the patient's condition, clinical technique, injection site, and target vessel

Substituting for  $\mu_C$  and  $\mu_T$  in the equation for subject X-ray contrast yields:

$$C_X \sim -\left[(\mu/\rho)_I \cdot X_I \cdot f - \mu_T\right] \cdot d$$

If we assume that  $f = 1/5$ , then this equation predicts that a contrast medium-enhanced vessel 1.5 mm in diameter will yield a subject X-ray contrast of  $\sim 0.1$  (viz.,  $\sim 10\%$ ).

### 11.4.3 X-Ray Scatter and Contrast Degradation

The description of subject X-ray contrast developed here has focused upon the primary X-ray beam and ignored the influence of scattered X-rays. X-ray scatter, which is an inevitable consequence of Compton interactions particularly in soft tissue, produces a fog of X-rays across the image field. These scattered X-rays are geometrically uncorrelated with the body structures and contribute no useful information to the image. In practice, the primary subject X-ray contrast is reduced by the scattered X-rays, and hence the quality of the recorded image is degraded. The contribution of X-ray scatter can be quantified in terms of the scatter-to-primary ratio (SPR), viz., the ratio of the intensities of the scatter and primary content of the X-ray beam. SPR varies with a number of characteristics of the X-ray image formation process. Important factors include the area of the X-ray beam entering the patient and the thickness of the body section, essentially the volume of tissue irradiated. SPR also increases with increasing X-ray beam energy (principally the kVp). The reduction in subject X-ray contrast produced by scatter is described by the simple equation:

$$C_s = C_x \cdot [1 + \text{SPR}]^{-1}$$

where the term  $[1 + \text{SPR}]^{-1}$  has a value less than unity and therefore is often referred to as the *scatter degradation factor*.

SPR varies with the radiographic exposure technique, the body section imaged, and the patient size. In abdominal angiography, SPR can measure 4:1 or so; in other words, ~80% of the X-ray beam exiting the patient comprises (unproductive) X-ray scatter. Consequently, subject X-ray contrast will be reduced significantly (by around a factor of 5) unless remedial measures are taken. In the very large-sized patient, the SPR can be some 100% larger than that for the average-sized patient; hence, subject X-ray contrast can be reduced by a factor of 2 or so. Fortunately, the contribution of X-ray scatter can be reduced via a number of technique and equipment refinements. Minimizing the volume of the patient exposed to X-rays by using tight collimation of the X-ray beam decreases SPR and hence boosts the subject X-ray contrast; at the same time, the patient radiation dose will be reduced. Another method

of rejecting scatter includes the introduction of an air gap between the patient and the image detector. This allows (some of) the X-ray scatter to bypass the image detector. The air gap technique is commonly used in pediatric imaging.

### 11.4.4 Antiscatter Grid

The scatter rejection technique most commonly used in adult cardiovascular imaging is the X-ray antiscatter grid. The grid is positioned after the patient and mounted adjacent to the image detector. A grid comprises an array of thin, parallel slats of strongly absorptive material, typically lead, interleaved with thin spacers made of a radiolucent material, such as fiber or aluminum (Al). The grid is covered with a low-attenuation material (e.g., carbon fiber). The grid preferentially allows primary X-ray photons to pass between the lead slats and therefore to contribute to the recorded image. Scattered X-rays, on the other hand, which are deflected at an arbitrary angle, have a much greater probability of striking a lead slat and hence being removed from the beam.

The degree of scatter rejection by a grid is described by the grid selectivity:

$$\Sigma_G = T_G \{P\} / T_G \{S\} > \text{unity}$$

where:

$T_G \{P\}$  is the (fractional) transmission of the grid for primary X-ray photons

$T_G \{S\}$  is the (fractional) transmission of the grid for scattered X-rays

The selectivity of a grid used in fluoroscopic applications typically lies in the range from 5:1 to 8:1.

When an antiscatter grid is present, the SPR is decreased, and therefore the subject X-ray contrast is improved (increased), viz.:

$$C_G = C_x [1 + \text{SPR} \cdot 1 / \Sigma_G]^{-1} > C_s$$

At the same time, however, some primary X-ray photons are absorbed by the grid, and therefore the patient dose must be increased to compensate for this. When an X-ray antiscatter grid is used, the fluoroscopy dose rate must be increased by a factor of ~1.5–3. Fluoroscopy equipment should offer the operator the option of removing the grid, as circumstances demand. Grid removal is

accepted practice in pediatric imaging, but may also have a role in adult procedures [4]. Larger savings in dose would accrue if the grid could be removed during examinations of larger patients. Unfortunately, this benefit comes at a cost of a marked deterioration in subject X-ray contrast (and hence image quality). This problem can be ameliorated somewhat if an air gap is used to partially offset the loss of the grid selectivity.

### 11.4.5 Imaging Geometry

The geometry used in standard-projection X-ray imaging is depicted schematically in **Fig. 11.5**. The X-ray beam emanates from a quasi-point source of radiation, and the resulting field of X-ray photons diverges with increasing distance from

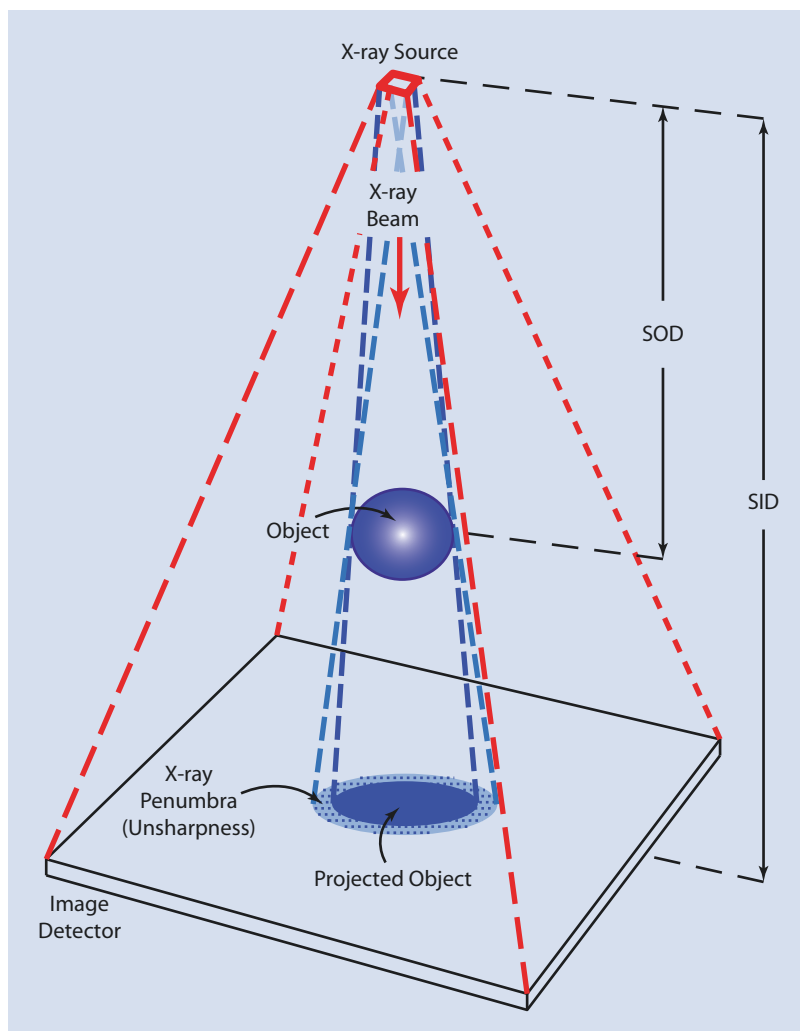
the source. Associated with the divergence of the X-ray beam is a reduction in intensity, which is described by the familiar inverse square law, viz.:

$$\text{Intensity} \propto 1/D^2$$

Doubling the distance of the X-ray source to the imaging plane by a factor of 2 decreases the incident X-ray beam intensity by a factor of 4 (viz.,  $2^2$ ). The (attenuating) object intercepts the X-ray beam and produces a projection image of the object in the plane of the detector.

From the standpoint of X-ray physics, the body section essentially represents a three-dimensional (3D) framework of attenuating structures. A diverging cone beam of radiation is used to address these structures and form the basic X-ray image. The image is typically recorded

**Fig. 11.5** Schematic diagram of the geometry used in standard-projection X-ray imaging



as a two-dimensional (2D) projection of the patient volume on an area detector. As a result, structures lying along a given ray are superimposed, and information as to their exact depth within the body is essentially lost. This superposition of body structures can lead to ambiguities when interpreting the final image. This can only be avoided if a more sophisticated X-ray imaging geometry is adopted, as we will see ▶ Sect. 11.6.3.

The divergent nature of the X-ray beam means that an object (in the body) projected on the image detector is subject to geometrical magnification, defined by the ratio:

$$M = \text{SID} : \text{SOD}$$

where SOD is the X-ray source-to-object distance and SID is the X-ray source-to-image-detector distance.

Objects in the body situated at different distances from the X-ray source are subject to differing degrees of geometrical magnification. For example, iodinated vessels of the same diameter at the front and back of the body section will be projected onto the image detector with differing widths. This geometrical process can distort the pattern of body structures that are recorded. Obviously, provided that absolute estimates of size–scale are not required, as is the case in many imaging tasks, this need not be a problem. Where quantitative estimates of size are important, however, calibration of scale against a device of known size is essential.

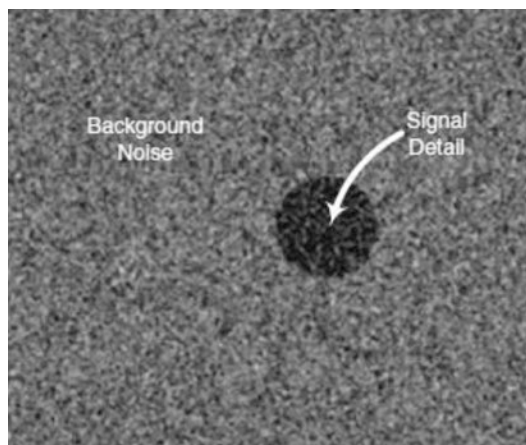
When geometrical magnification is used, the finite size of the X-ray focus produces an X-ray penumbra around projected objects, as illustrated in ■ Fig. 11.5. This can lead to blurring of signals recorded in the image, particularly those that are very small in size and/or fine in texture. However, larger structures with sharp discontinuous edges will also be affected. This blurring process, known as *geometrical unsharpness*, can result in a visible loss of spatial resolution in the images. Geometrical unsharpness can be kept to a minimum by correct choice of X-ray focus, combined with minimizing the degree of magnification. The latter can be achieved by keeping the body section in close contact with the image detector and by keeping the detector at some distance from the X-ray source. Contact geometry is also favorable from the standpoint of minimizing the patient dose. Geometrical unsharpness is only one of several potential sources of blur in an X-ray image.

X-ray image detectors also have a limiting spatial resolution. Factors affecting the spatial resolution of a modern dynamic X-ray image detector are discussed in ▶ Sect. 11.9.4. For contact geometry (minimum geometrical magnification), the unsharpness of the X-ray image detector normally dominates spatial resolution.

The recording of time-resolved information is essential in cardiovascular imaging. The imaging of dynamic structures and devices however may be subject to a further source of blur due to motion unsharpness. The degree of motion unsharpness depends upon the speed of the moving structure and the temporal resolution of the image acquisition process. This issue can be particularly important when imaging the heart and coronary vessels and, of course, in pediatric patients. Today, modern dynamic X-ray image detectors exhibit negligible temporal unsharpness (lag); therefore, high-fidelity recording of dynamic structures is essentially limited by the duration of the X-ray exposure pulses. In turn, this encourages the use of powerful X-ray sources that can deliver sequences of very intense X-ray pulses of suitably short duration. Such arguments apply equally well to (low-dose) pulsed fluoroscopy and (high-dose) serial image acquisition.

## 11.5 Signal-to-Noise Ratio Description of X-Ray Images

Quantum physics reveals that an X-ray beam comprises a stream of individual packets of energy or photons, not a continuum of energy. Consequently, the interaction mechanisms that underpin the formation of the X-ray image are statistical in nature. Inevitably, the fabric of the recorded X-ray image is perturbed by random fluctuations in the photon count contributing to each of the picture elements forming the image. These fluctuations are often referred to as *X-ray quantum noise*. In fluoroscopy, the noise fluctuations are a function of both space and time, subjectively giving the appearance of a scene viewed during a heavy snowstorm. These dynamic noise fluctuations overlay the useful signal information and are most obvious in regions of uniform tissue background. The presence of noise fluctuations sets a fundamental limit to the quality of the image that can be formed using X-rays, as illustrated in ■ Fig. 11.6.



■ Fig. 11.6 X-ray image illustrating a signal detail and background noise

### 11.5.1 Definition of Signal-to-Noise Ratio

To evaluate noise, it is necessary to consider the number of X-ray photons that are incident upon the image detector after exiting the patient. Noise fluctuations are quantified in terms of the standard deviation of the count of primary X-ray photons contributing to the picture elements [1]. Given that Poisson statistics apply, the standard deviation of the noise is simply given by the square root of the mean photon count:

$$\sigma \sim N^{1/2}$$

The magnitude of the background signal is the corresponding mean photon count:

$$S \sim N$$

These quantities make it possible to define the signal-to-noise ratio (SNR) of the incident X-ray beam, viz.:

$$\text{SNR} = S / \sigma = N^{1/2}$$

This equation shows that the SNR increases (improves) with the square root of the count of X-ray photons incident upon the image detector. In other words, increasing the photon count (and hence the radiation dose) by, say, a factor of 4 will only increase the SNR by a factor of 2 (viz.,  $\sqrt{4}$ ), while a 100-fold increase in the photon count (and hence the radiation dose) will only increase the SNR by a factor of 10 (viz.,  $\sqrt{100}$ ). These

values highlight the fact that any improvement in the SNR (image quality) can only come at the price of an increased photon count and ultimately an increased radiation dose to the patient.

It must be emphasized that the SNR referred to here is that delivered by the X-ray beam at the image detector. In practice, this *input* SNR is degraded by the technical shortcomings in the X-ray image recording system. For example, the image detector cannot record the full complement of primary X-ray photons incident upon it. In addition, the detector exhibits other intrinsic deficiencies that degrade the signal and boost the noise. As a result, in practice, the SNR in the recorded image is always less than that in the incident (input) X-ray beam. The SNR performance of modern designs of dynamic X-ray image detectors is discussed further in ▶ Sect. 11.9.6.

### 11.5.2 Detail Signal-to-Noise Ratio

The definition of the SNR developed above applies to a featureless background signal ( $S$ ). For a more realistic imaging model, a differential (or detail) signal is required; again this might, for example, represent an opacified blood vessel. The resulting detail signal ( $\Delta S$ ) is described by the product:

$$\Delta S \sim C_X \cdot N$$

where  $C_X$  is the primary subject X-ray contrast of the signal detail.

Again, rather than considering the signal detail and the noise separately, it is more instructive to evaluate the balance between these quantities, viz., the detail signal-to-noise ratio ( $\Delta\text{SNR}$ ). For example, a comparatively high level of image noise may not in itself be intolerable, provided that the relevant detail signal has sufficiently high subject X-ray contrast. Alternatively, a detail signal with comparatively low contrast may still be detectable provided that the noise fluctuations are appropriately small. Increasing the  $\Delta\text{SNR}$  will improve the overall subjective quality of the image and at the same time will improve the visibility of low-contrast details. Degrading the  $\Delta\text{SNR}$  has the opposite effects. The  $\Delta\text{SNR}$  is defined as follows:

$$\Delta\text{SNR} = \Delta S / \sigma = [C_X \cdot N] / N^{1/2} = C_X \cdot N^{1/2}$$



This equation confirms that the  $\Delta\text{SNR}$  increases with the square root of the primary photon count. Improving the  $\Delta\text{SNR}$  therefore demands an increase in the dose to the patient. The definition also shows that the  $\Delta\text{SNR}$  is proportionate to the signal contrast. Therefore, an alternative strategy for improving the  $\Delta\text{SNR}$  might be to boost the subject X-ray contrast of the signal, say, by reducing the X-ray beam energy. Again, however, any improvement would come at a cost of an increased patient dose.

The  $\Delta\text{SNR}$  and hence the image quality achievable in dynamic X-ray imaging can be traced to the dose per frame used by the image detector. In cardiovascular X-ray imaging, a wide range of values of dose per frame are needed for the various different imaging modalities. Fluoroscopy uses a comparatively low dose per frame, and therefore the images are formed with a low X-ray photon count. Not surprisingly, therefore, fluoroscopy images have low  $\Delta\text{SNRs}$ , are subject to strong noise, and offer only modest visualization of low-contrast details. On the other hand, in serial image acquisition, the dose per frame is usually increased by a factor of 10, 100, or even 1000 (depending upon the modality involved). As a result, the  $\Delta\text{SNR}$  will ramp up, reducing noise and progressively improving the visibility of low-contrast details.

It is also useful to appreciate that the  $\Delta\text{SNR}$  is strongly linked to a physical interpretation of information. Increasing the count of primary X-ray photons will increase the quantity of information available in the image. Obviously, such a gain in information, however, must be balanced against the increase in radiation dose incurred by the patient. Clearly, there is no justification for increasing the radiation dose beyond the minimum level required to derive the information needed to perform the clinical task (in accordance with the ALARA principle). On the other hand, this model also illustrates the risk associated with overenthusiastic reductions in the dose and hence in the X-ray photon count. Reducing the photon count to too low a level will seriously degrade the  $\Delta\text{SNR}$  and, as a result, the image quality. This will reduce the information content of the images, potentially beyond the point where it is possible to successfully perform the clinical task.

The trade-off between the image quality and the patient dose can be explored systematically using a suitable figure of merit (FOM) [5]. The

FOM can be used to quantify how effectively the dose delivered to the patient is converted to X-ray image information. The FOM is typically defined by a quantity such as:

$$\text{FOM} = \Delta\text{SNR}^2 / \text{Dose}$$

Here the dose to the patient can be categorized in a number of ways depending upon the nature of the study—for example, the entrance surface dose, the total energy imparted, and the effective dose. Such an FOM model has been successfully used to explore the optimum X-ray exposure factors (including the kVp and beam filtration) in both adult and pediatric fluoroscopic imaging scenarios [5, 6].

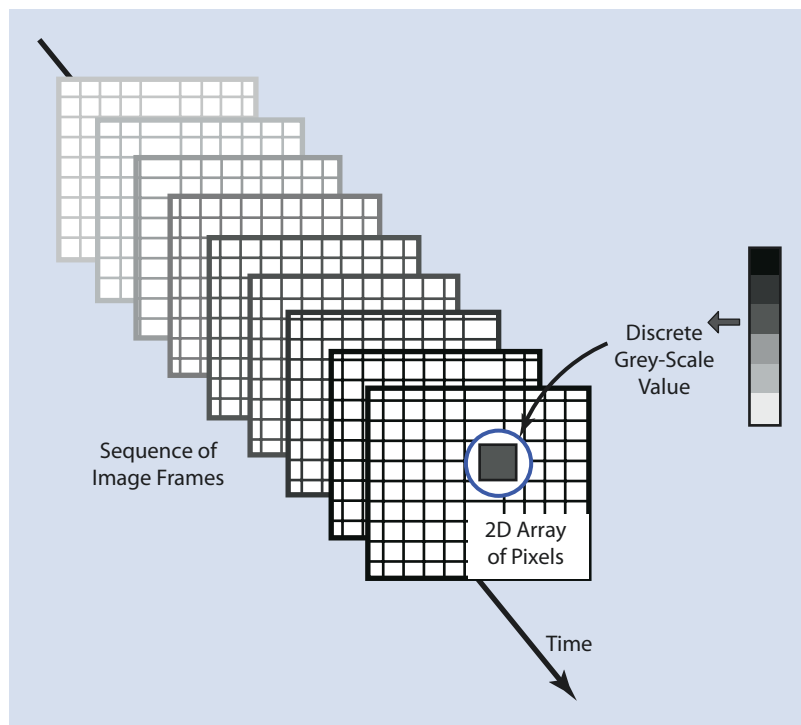
The  $\Delta\text{SNR}$  model developed here can be extended to take account of scattered X-ray photons. In theory, scattered X-ray photons actually degrade the image quality by increasing the noise, rather than by reducing signal contrast, as indicated in ► Sect. 11.4.3. The  $\Delta\text{SNR}$  model can be developed further to take account of the antiscatter grid. As a result, FOM analysis can also be used to evaluate the viability of X-ray scatter rejection strategies (such considerations, however, go beyond the needs of this chapter).

## 11.6 Digital X-Ray Imaging

### 11.6.1 The Digital Image

All modern cardiovascular X-ray image detectors record images in digital form. The use of the term *digital* implies a number of attributes, which are briefly reviewed in this section. A digital image is an electronic image represented in a data format compatible with computer hardware and software protocols. As such, the image can be captured, processed, stored, and communicated rapidly and efficiently. It should be understood that dynamic X-ray images comprise a sequence of individual frames over time, as illustrated schematically in ■ Fig. 11.7. Hence, dynamic processes are discretely sampled in time at a frame rate that can hopefully depict relevant moving structures and devices within the body. The acquired image sequences are often viewed as a movie presentation. A modern imaging system incorporates a digital video frame buffer, making it possible to display movie images at a rate independent of the

■ **Fig. 11.7** Schematic diagram of dynamic X-ray imaging: sequence of individual digital image frames acquired over time



acquisition rate. Image frames in the sequence may also be stepped through individually and viewed as a static display. Salient image frames may then be selected to document clinical findings.

Each frame in the image sequence is a spatially sampled (discretized) representation of the input X-ray image, not a continuously varying (or analog) version. The image frame is represented as a regular 2D array of minute, square picture elements or pixels. For a square-format image, the matrix contains  $[N \times N]$  pixels (for example  $[1024 \times 1024]$  pixels). A rectangular format image contains  $[N \times M]$  pixels where  $N \neq M$  (for example  $[2560 \times 2048]$  pixels). As we see in ► Sect. 11.8.2, these pixels are built into the electronic superstructure of modern solid-state digital X-ray image detectors. The size of the pixels has a strong influence upon the fidelity of the images. The smaller the pixel size, the greater the spatial resolution of the recorded images, but the greater the quantity of data that have to be managed, stored, processed, displayed, etc.

The pixel-sampling interval of a detector  $\Delta p$  can be calculated from the number of pixels along a dimension  $N$  and the equivalent field of view  $W$  such that:

$$\Delta p = W / N$$

The equivalent pixel resolution of the detector is expressed in terms of the linear density of pixel pairs and is normally expressed in line pairs (lp) per millimeter. This spatial frequency is commonly referred to as the *Nyquist frequency*  $f_N$  where:

$$f_N = 1 / 2\Delta p = N / 2W$$

For example, if  $N = 1024$  pixels and  $W = 20$  cm, then  $f_N = 1024/400 = 2.56$  lp mm<sup>-1</sup>

Dynamic detectors have been developed with different fields of view, form factors, and pixel resolutions to match the differing needs of the various types of cardiac and vascular imaging application. The total number of pixels forming an image frame can be calculated from the ratio of the active area of the detector to the area of an individual pixel. In a modern dynamic digital detector, an image frame can contain anything between 1 million and over 5 million pixels.

Associated with each pixel in the image is a grayscale value that represents the intensity of the image at that pixel location. This grayscale value is selected from a set of discrete levels, not a continuum of intensity values. By convention, digitization of the overall grayscale range is expressed as a power of 2 and quantified in terms of the number

of bits (binary units) of information per pixel. Increasing the number of bits per pixel improves the grayscale resolution of the image data. The grayscale resolution is defined by the specification of the analog-to-digital converter (ADC), which digitizes the analog input signal (e.g., to 8, 10, 12, 14, or greater bit resolution). The number of grayscale levels  $G$  allocated per pixel for digitization with  $g$  bit resolution is given by the simple equation:

$$G = 2^g$$

Modern (solid-state) image detectors typically digitize the image to 14 bits of grayscale resolution. Substituting in the above equation, we see that a 14-bit image enjoys a generous choice from some  $2^{14} = 16,384$  grayscale levels at each pixel site. Such a specification is adequate for standard dynamic X-ray imaging applications. More sophisticated image acquisition schemes such as 3D reconstructive imaging may require improved grayscale resolution (e.g., 16 or even 18 bits per pixel).

The acquisition of a sequence of digital images generates copious quantities of data. The total quantity number of bits of data ( $N$ ) acquired in a single run of  $\tau$  seconds duration and at frame rate  $f$  is given by the product:


$$N = g \times N \times M \times f \times \tau$$

Total data content is often expressed as bytes of data, where 8 bits equals 1 byte. A single digital cardiac image acquisition run can generate hundreds of megabytes of data, where 1 megabyte equals 1 million bytes of data. Obviously, acquisition of multiple runs increases the data load proportionately, unless data compression is used.

As described so far in this section, a digital X-ray image is represented as a simple bitmap. Such an image format is too primitive to be reliably used to communicate and display image files in a clinical department. The image file must also contain relevant administrative and technical information. This typically takes the form of metadata in a header to the raw image data. Such a file format has been developed specifically for medical imaging applications, known as the DICOM (Digital Imaging and Communications in Medicine) standard. The DICOM header defines not only the basic image specification

(including pixel array size and bit depth) but also contains patient demography plus other technical information about the image acquisition device, the radiographic examination, and display characteristics. In the future, the header will explicitly include patient radiation dose information. The DICOM structures used in cardiac and vascular digital X-ray imaging share common features—for example, both organize image files into *runs* and *studies*. DICOM also supports both lossless and lossy image compression—for example, via the JPEG compression standard. Compliance with the DICOM standard facilitates interfacing image acquisition system(s) with a picture archiving and communication system (PACS) environment and should ensure portability of image data across different hardware platforms.

## 11.6.2 Digital X-Ray Imaging System

A modern cardiovascular digital X-ray imaging system is an assemblage of several key high-technology components. The overall layout of a typical imaging system is illustrated schematically in  Fig. 11.8. The components identified in this block diagram each make a conspicuous contribution to the dynamic imaging process: from X-ray production to image acquisition to computer processing and storage, through to final display.

Successful interventions rely upon (among many other things) the matched and synergetic operation of the key components of the imaging equipment. Powerful but also flexible production of X-rays is essential to ensure dose-efficient recording of high-quality dynamic images. Important technological developments in this area include X-ray tubes with a much-improved anode heat capacity and management, and also grid-controlled X-ray tubes. These developments have had a significant impact on fluoroscopy-guided cardiovascular interventions in particular. To facilitate dose-efficient system operation, imaging systems utilize increasingly sophisticated automatic dose rate control (ADRC). ADRC systems are designed to automatically set optimized X-ray exposure factors for each individual patient and type of examination [7].

Image detectors play a pivotal role in the capture of high-quality X-ray image sequences and their conversion into a stream of digital data. Recent years have seen a paradigm shift in

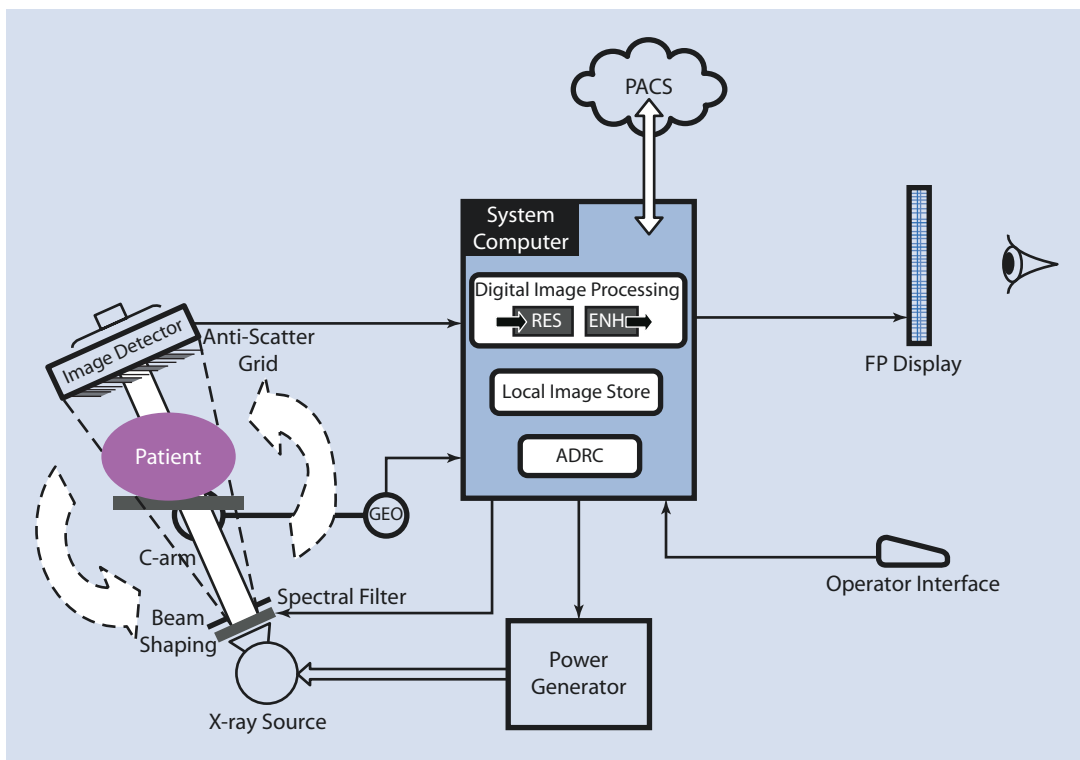


Fig. 11.8 Schematic diagram of a modern cardiovascular X-ray imaging system

image detector technology from electron-optical television-based devices to the new generation of solid-state image detectors [8, 9]. All acquired images must undergo digital image processing to ensure optimum image quality. In modern detectors, this includes digital image calibration to correct for cosmetic deficiencies in the image detector and to restore the physical integrity of the acquired data. In addition, digital image enhancement is used to ensure that the visual quality of the images presented to the clinician is also optimized. Today, images are viewed on high-quality flat-screen (FS) monitors. To meet the immediate and short-term image storage needs of the interventionalist, the system must provide access to high-speed data storage (of medium capacity), typically a magnetic hard disc. To meet the long-time image storage needs, the system must provide access to a secure, large-capacity archive; this is typically achieved via an institutional (or possibly a dedicated) PACS network. Some environments also use portable archive media, such as recordable optical disks, to store results of individual procedures.

The X-ray source and image detector are affixed to a C-arm (or a similar design) attached to a floor- or ceiling-mounted stand. The C-arm can be rotated to different positions around the patient [10] to optimize the projection geometry at each stage of the procedure. The geometry of the C-arm is calibrated (GEO), enabling the X-ray projection angle(s) to be set up automatically by the system if required. Continuous motorized rotation of the C-arm (plus the source and detector) about the isocenter is also used to acquire a set of projections over a wide angular sweep around the patient. The resulting set of images can be viewed on the display as a rotating panorama. Alternatively, the acquired projection data can be used to compute a 3D image. The system described is a single-plane C-arm unit. Biplane configurations, which incorporate two C-arms and two orthogonal X-ray imaging channels, are also widely used in cardiovascular imaging, particular for pediatric examinations. The economic cost and clinical role of single- and biplane configurations may differ, but the physics and technologies remain the same.

Salient enabling technologies that underpin modern cardiovascular imaging, from the X-ray equipment to the final display, are reviewed in ► Sects. 11.7, 11.8, 11.9, 11.10 and 11.11. Preparatory to this, however, the basic physics of three widely used cardiovascular imaging techniques—digital subtraction angiography, rotational angiography (RA), and 3D reconstruction imaging—are briefly discussed.

### 11.6.3 Digital Subtraction Angiography

A digital image is represented by an array of numbers that encode pixel locations and associated intensity values. Outputting the arrays of numbers to a suitable display device such as a solid-state FS monitor makes it possible to view dynamic image sequences and/or selected image frames. Prior to viewing the display image, the data are subject to digital enhancement (numerical manipulation of the image data) to optimize the presented subjective quality. This is widely used in dynamic grayscale imaging in order to improve contrast and spatial resolution and to reduce noise fluctuations. Other imaging algorithms can be used to process the image data to achieve more fundamental improvements in the presentation of clinical information. A typical example of such an algorithm is digital subtraction angiography (DSA) [11–13].

The aim of DSA is to generate a sequence of images that clearly depicts the flow of iodinated contrast medium through the arteries of interest, unencumbered by overlying anatomical structures. Here the contrast medium-enhanced vessel is the signal of interest. This is achieved by first acquiring a mask image of the background anatomy. The contrast medium is then injected into the vessel, and a sequence of images is acquired, which records the inflow and washout phases. In a standard grayscale presentation, X-ray beam attenuation due to the competing background anatomy represents a powerful source of noise. Fortunately, this anatomical structured noise can, in principle, be eliminated by subtracting the contrast medium-enhanced image frames ( $I_{\text{Contrast}}$ ) and the mask image ( $I_{\text{Mask}}$ ) [14]. Following digital subtraction, the static (common mode) image content is eliminated, leaving an impression of the changing opacification of the vessels due to

the transit of the contrast medium. Clinical experience has shown that optimum DSA imaging requires logarithmic (rather than linear) subtraction of image frames; this algorithm is described by the equation:

$$\Delta S = \log I_{\text{Contrast}} - \log I_{\text{Mask}} \text{ or alternatively } \log \left\{ I_{\text{Contrast}} / I_{\text{Mask}} \right\}$$

This result indicates that DSA actually represents the (log) division of images rather than (linear) subtraction. Contrast enhancement is then (normally) applied to the log-subtracted image to optimize detail visibility in the final display. The overall DSA algorithm is summarized in ► Fig. 11.9.

Logarithmic subtraction eliminates the imprint of the background anatomy, depicting the opacified vessels (in either black or white polarity) laid out upon a uniform (gray) background. In practice, this is not quite correct as DSA produces on the gray background a heterogeneous field of random noise; this artifact is known as the *DSA noise print*. The noise print reflects the varying contributions of quantum and electronic noise over regions of different X-ray attenuation (defined by the background anatomy). Random noise in the mask and contrast medium-enhanced image frames is uncorrelated and therefore adds (rather than subtracts). Therefore, DSA eliminates the anatomical structure noise but boosts the overlay of random noise. Assuming that the variance of the noise in the contrast-enhanced image ( $\sigma_{\text{Contrast}}^2$ ) and the mask images ( $\sigma_{\text{Mask}}^2$ ) are of similar magnitude, the DSA algorithm will amplify the noise variance (power) by a factor of 2, viz.:

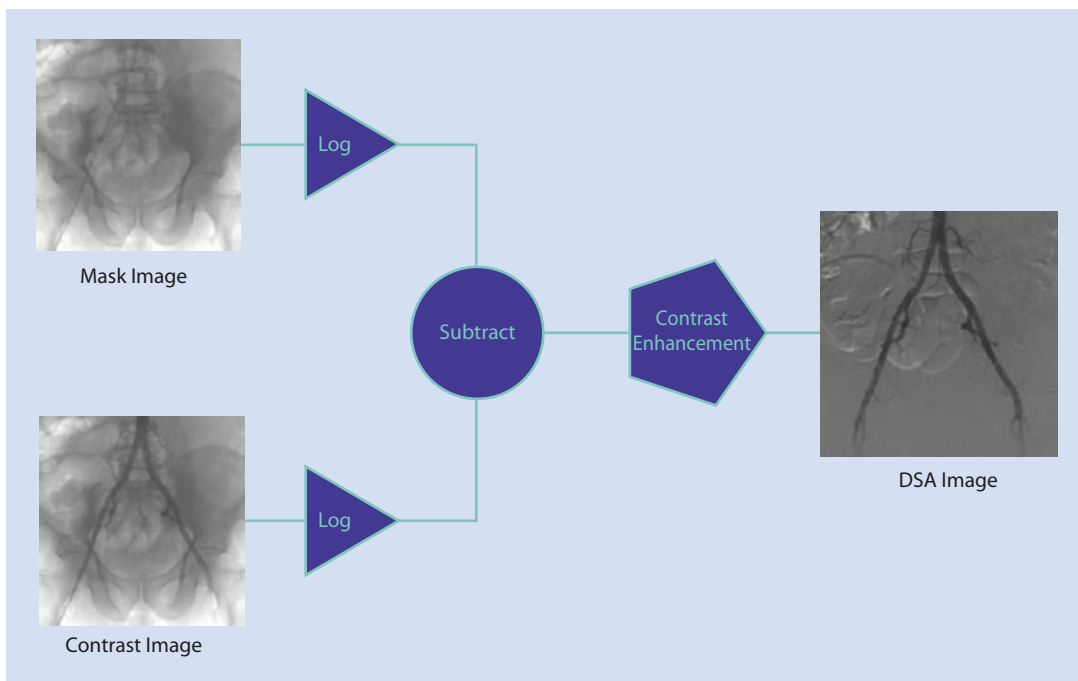
$$\sigma_{\text{DSA}^2} = \left[ \sigma_{\text{Contrast}^2} + \sigma_{\text{Mask}^2} \right] \sim 2 \cdot \sigma^2$$

Correspondingly, DSA reduces the  $\Delta \text{SNR}$  (of the opacified vessel) by a factor of  $\sqrt{2}$ , viz.:

$$\Delta \text{SNR}_{\text{DSA}} = \Delta S / \sigma \sqrt{2} = \Delta \text{SNR} / \sqrt{2}$$

Despite this, provided that the X-ray dose per frame is sufficiently high, the conspicuity of the opacified vessel will be significantly improved by the subtraction of the background anatomy, compared with an individual grayscale image (which retains this structured noise). The dose per frame used in DSA can be a factor of 10 (or so) greater than that used in grayscale image acquisition.





■ Fig. 11.9 Schematic diagram of the digital subtraction angiography (DSA) imaging algorithm

DSA is a temporal subtraction algorithm, as the image frames are subtracted across time. Therefore, in principle, DSA relies upon the patient remaining immobile during image acquisition to prevent (minimize) spatial misregistration. In practice, this is not always achievable; therefore, remedial postprocessing may be needed to ameliorate motion-related artifacts; techniques include remasking, pixel shifting, and automatic reregistration. To date, DSA has proved to be successful in all clinical areas apart from coronary artery imaging. This is due to the rapid and sometimes irregular motion of the heart plus lung motion due to respiration, which can overlap the heart. Recent advances in computer processing, however, may resolve this issue. Nevertheless, in all other clinical areas, DSA has been the imaging yardstick in vascular diagnosis and intervention for well over a quarter of a century.

Alternative algorithms to DSA include energy subtraction, whereby images acquired at two different X-ray beam energies are digitally subtracted. Energy subtraction has certain attractions in cardiovascular imaging as it is potentially less susceptible to movement misregistration, as no precontrast mask image is required. However, in practice, the subtraction of the background

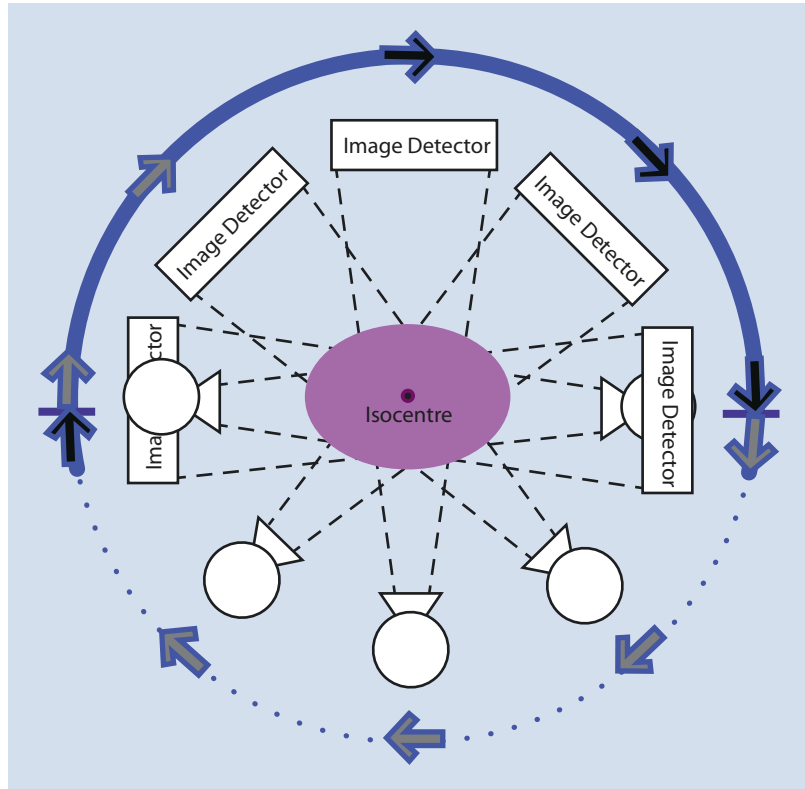
anatomy still may not be complete. As a result, hybrid subtraction has also been investigated as it potentially combines the benefits of temporal and energy subtraction [15]. To date, however, neither the energy subtraction nor the hybrid subtraction algorithms have proved to be a suitable replacement for DSA in clinical routine.

#### 11.6.4 Rotational Angiography

The 2D projection images routinely produced in fluoroscopy and digital image acquisition (including DSA) provide an incomplete geometrical representation of cardiovascular structures. Individual projection images of opacified vessels are susceptible to overlapping and foreshortening, which limit the precision of the clinical information that is derived. Recording two orthogonal views (in biplane imaging) offers an improved, but still incomplete, perspective on target vascular structures. Even better-quality clinical information is derived if multiple angular views are acquired (■ Fig. 11.10). For example, a set of digital images can be acquired at equiangular intervals over a semicircular sweep of the C-arm around the body section. In its most



■ **Fig. 11.10** Schematic diagram of the geometry of rotational angiography (RA) X-ray image acquisition



In its basic form, this imaging technique is known as *rotational angiography* (RA). In RA, the C-arm typically rotates at a constant angular speed of 30–60 degrees  $s^{-1}$  and describes a sweep of 180–240° around the body. A single bolus of contrast medium is injected for the duration of the acquisition phase. Reasonably rapid data acquisition is essential to ensure maximum vessel filling and minimum motion blur. Projection images are typically acquired at a frame rate of 10–30 frames  $s^{-1}$ . A higher frame rate than this, such as 60 frames  $s^{-1}$ , may occasionally be required, but this usually requires a compensatory reduction in pixel resolution (to balance the quantity of data acquired). Projection images are often acquired at dose levels suitable for grayscale acquisition rather than for DSA; the dose per frame in RA can be 4–10 times lower than that used in DSA exposures.

The C-arm is rotated around a fixed reference point, known as the *isocenter*. The clinical region of interest must be accurately positioned at the isocenter before the image acquisition begins. The acquired image sequence can then be viewed on the display screen as a movie loop, depicting

a rotating panorama of the vasculature. RA relies upon motion parallax to engender an impression of depth, which otherwise is missing in 2D projection images. Either a grayscale or a subtractive approach can be adopted in RA imaging. The latter requires a double sweep of the C-arm with projection images acquired at equivalent angular positions. A set of mask images is acquired during the first sweep, and this is followed by a second (reverse) acquisition sweep while the bolus of contrast medium is injected. RA has proved to be particularly useful in neurovascular imaging—for example, in improving the depiction of the shape, location, and orientation of intracranial aneurysms [16, 17]. Over the years, RA has found a role in other clinical areas, including abdominal interventions [18] and renal artery assessment, and also in improved visualization of coronary arteries. For example, three studies have investigated the safety and clinical utility of RA in coronary artery procedures, reporting significant reductions in the contrast medium load, radiation dose, and procedure time, compared with standard 2D digital cardiac imaging [19–21].

### 11.6.5 Three-Dimensional Reconstruction Imaging

RA images are now normally viewed not as a movie presentation but as a 3D (volume) reconstruction [22, 23]. The wide-angle cone-beam geometry that prevails in RA means that specialized computer reconstruction algorithms must be used. 3D data sets are typically reconstructed using an algorithm such as the Feldkamp–Davis–Kress (FDK) cone-beam filtered back-projection method or something similar [24–26]. Computed tomography (CT) imaging in 3D using an area detector and cone-beam geometry is inevitably more susceptible to X-ray scatter than multislice CT (MSCT); the latter benefits from tight collimation of the X-ray beam both at the source and at the detector array. Reportedly, the X-ray scatter-to-primary ratio found in C-arm-based cone-beam CT can exceed 3:1, while the SPR of an MSCT scanner typically measures 0.2:1 [27] or less. The presence of X-ray scatter reduces the  $\Delta$ SNR and degrades the visibility of low-contrast sensitivity in 3D reconstructed images. In addition, scatter induces artifacts in the reconstructed images, such as cupping (in regions of homogeneous attenuation) and streaks between high-attenuation structures. The presence of scatter also perturbs the calibration of reconstruction in terms of Hounsfield units (HUs). A variety of strategies is employed to reduce X-ray scatter in C-arm-based cone-beam CT. These include use of an antiscatter grid and/or air gap and a bow tie or wedge-shaped beam-compensating filter. In addition, software corrections are often applied to correct for quantitative estimates of the X-ray scatter. Together, these techniques improve image quality and reduce the artifacts induced by X-ray scatter in C-arm-based cone-beam CT (but cannot correct for them completely).

Cone-beam CT images are reconstructed offline using a dedicated workstation, typically as a 3D array containing  $512^3$  or  $256^3$  voxels (volume cells). Implementation of surface-shaded display (or volume rendering) is then used to achieve a photorealistic representation of the vessels in 3D. Such 3D visualization techniques can help the clinician interpret complex webs of overlapping vessels [22, 23]. For example, vessel segments can be rotated on the workstation display and viewed from different perspectives. Access to 3D vascular

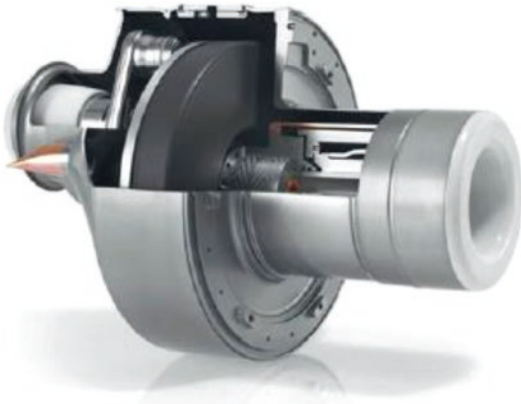
information should enable better-informed decisions to be made regarding treatment planning, implementation, and evaluation. Reportedly, in cardiovascular interventions, referral to a 3D reconstruction can replace multiple DSA and fluoroscopy runs, therefore leading to reduced procedure times, contrast medium loads, and radiation doses. Early applications of 3D cardiovascular imaging were aimed at the reconstruction of contrast medium-filled vessels, which exhibit strong subject X-ray contrast. Given recent advances in dynamic X-ray image detector technologies (discussed in ▶ Sect. 11.10.3), it is now also possible to reconstruct 3D images of low-contrast (soft-tissue) structures.

## 11.7 X-Ray Equipment

### 11.7.1 Direct Heat Removal from the Anode

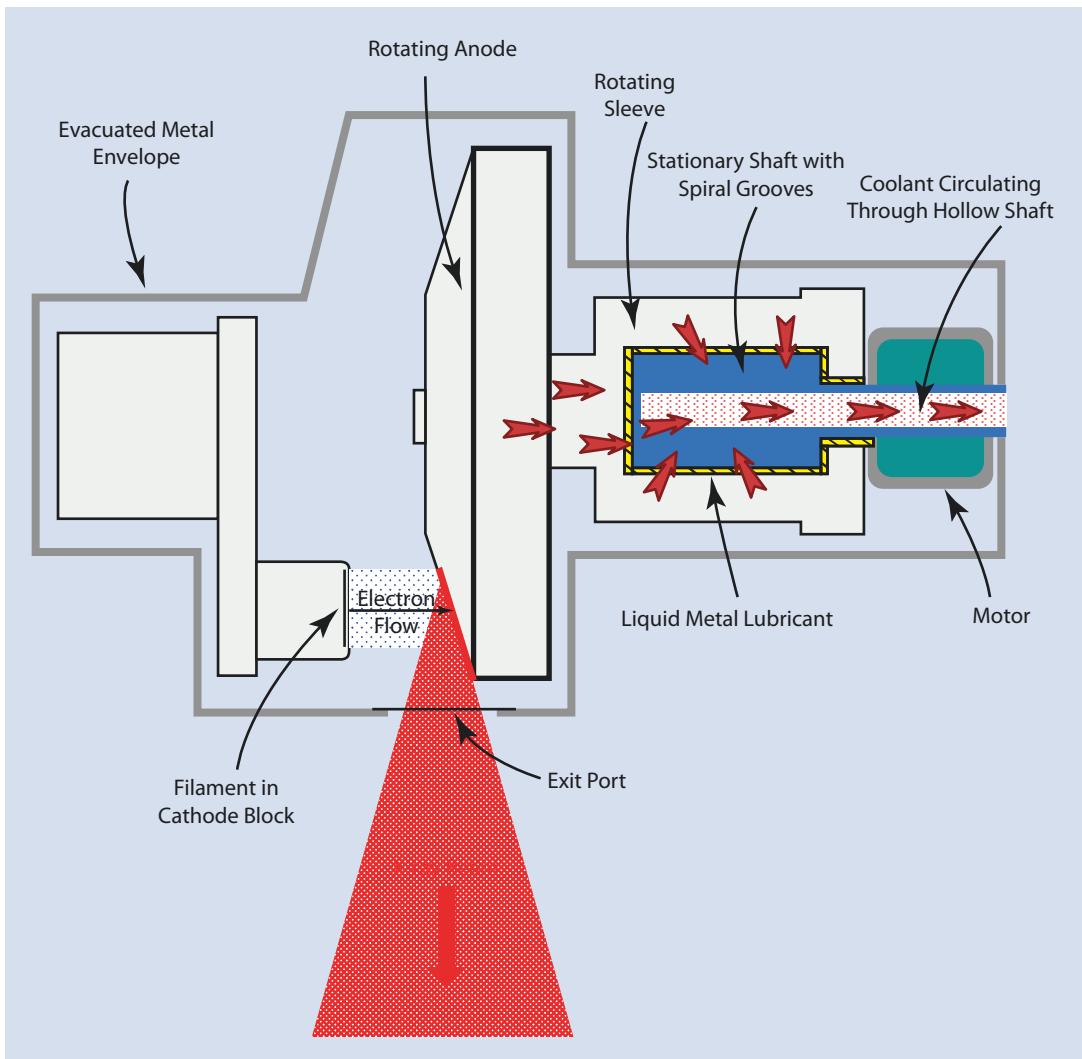
During extended periods of fluoroscopy and/or acquisition of multiple runs of serial images, the anode disk of the X-ray tube accumulates a considerable quantity of heat. Build-up of heat in the anode limits the duration and frequency of the fluoroscopy and associated exposure runs that can be implemented. Early designs of the X-ray tube relied upon thermal (infrared) radiation from the anode to dissipate the accumulated heat. More efficient heat management is achieved by direct removal of heat from the anode disk, and this strategy is now exploited by leading equipment manufacturers. One notable example of such a design is the Philips Maximus Rotalix Ceramic (MRC) X-ray tube [28], shown in ■ Fig. 11.11. This design of X-ray tube is well matched to the demanding exposure conditions prevailing in cardiovascular interventions, being able to sustain high X-ray tube output for extended periods of time.

The MRC X-ray tube utilizes a liquid metal-lubricated rotating sleeve. The anode disc and sleeve are mounted upon a stationary hollow metal shaft. Spiral grooves are machined on the outside surface of the shaft, as illustrated in ■ Fig. 11.12. The rotating sleeve glides over the thin film of liquid metal lubricant that separates the sleeve and shaft. The lubricant comprises a eutectic gallium–indium–tin (Ga–In–Sn) metal



■ **Fig. 11.11** Modern high-performance X-ray tube featuring a spiral groove bearing and liquid metal lubrication. (See «Acknowledgments»)

alloy, which is liquid at room temperature. The spiral groove bearing and liquid metal lubrication produce a friction-free interface between the two metal surfaces. This mechanism is analogous to a car aquaplaning on a wet road, whereby tire traction is lost when a driver (unwisely) drives at high speed. The rotating sleeve spins around the support shaft at 4200 revolutions per minute. The anode need only be accelerated up to full running speed once a day, via a motor contained within the tube itself. Having reached the running speed, the anode continues to rotate throughout the working day. The bearing supports a large-diameter (viz., 200 mm) anode disk, affording both high X-ray tube output and a large anode heat storage capacity.



■ **Fig. 11.12** Schematic diagram of an X-ray tube featuring a spiral groove bearing and liquid metal lubrication

Heat accumulating in the anode is removed not only by thermal radiation, but importantly also via a second direct heat transfer pathway. This pathway allows heat to be directly transferred through the rotating anode assembly to the coolant (oil), which is circulated through the hollow shaft. The hot oil is cooled via an external heat exchanger, before recirculation through the shaft. The resulting improvement in heat removal facilitates interventional imaging, eliminating unwelcome time delays between and/or during clinical procedures, which were frequently experienced in the past [29].

### 11.7.2 Grid-Controlled X-Ray Source

The traditional X-ray tube utilized only two electrodes: the cathode (filament) and the anode (target). With this design of X-ray tube, exposure switching had to be applied externally in the electrical power generator. As a result, during pulsed fluoroscopy X-ray exposure, pulses were subject to charge storage effects due to the capacitance of the long lengths of HV cables. Consequently, the exposure pulses had substandard characteristics, with a slow kV rise at the front edge and a slow decay at the end of the pulse. This prolonged the duration of the X-ray pulses and delivered spurious low-energy radiation. The former degraded the spatio-temporal resolution of moving vessels, while the latter increased the patient skin dose unnecessarily.

Modern X-ray tubes used in cardiovascular fluoroscopy now incorporate a third electrode, known as a *control grid* [30]. This control grid comprises a fine wire mesh mounted in the gap between the cathode and anode. Exposure switching is implemented directly at the X-ray source by applying a suitable bias voltage to the control grid either allowing tube current to flow or extinguishing the flow. The response of the grid-controlled X-ray tube to the control signal is instantaneous, essentially producing X-ray pulses with a perfectly square kV profile. This enables rapid sequences of precise X-ray pulses to be reliably generated. Pulsed fluoroscopy is the standard fluoroscopy technique in modern cardiovascular X-ray imaging. Pulsed fluoroscopy improves the spatiotemporal resolution of rapidly moving blood vessels and saves the radiation dose [31].

In adult coronary vessel imaging, fluoroscopy is commonly performed at a pulse rate of 15 frames  $s^{-1}$ , but very occasionally at

30 frames  $s^{-1}$ . For certain applications, particularly pediatric cardiac imaging, a frame rate of 60 frames  $s^{-1}$  may be used. In examinations where motion is less prevalent and/or dose reduction is paramount, fluoroscopy may be carried out with a lower pulse rate such as 10, 7.5, 6, or 3.75 frames  $s^{-1}$  (or even as low as 0.5 frames  $s^{-1}$ ). The low pulse rates are used in cardiac electrophysiology and in many areas of vascular fluoroscopy. Pulsed fluoroscopy at low frame rates requires digital gap filling to suppress the disturbing flicker that otherwise would appear in the displayed images. Gap filling signifies the repeated presentation of successive image frame(s) to achieve an apparent increase in the displayed frame rate.

### 11.7.3 High-Frequency Power Generator

Power generators are the devices used to generate electrical power and to control its delivery to the X-ray tube (see Fig. 11.8). Generators used in modern cardiovascular X-ray imaging systems typically have a maximum power rating of 80–100 kW. The generator supplies the X-ray tube with electrical power, as a rapid sequence of precise pulses. The resulting X-ray exposures must be tailored to the requirements of (high-dose) serial image acquisition and (low-dose) pulsed fluoroscopy as appropriate. Modern power generators utilize high-frequency (HF) power inverter technology [32]. HF generators are powerful and flexible, but compact in design and economical to manufacture. The HF generator functions by taking mains voltage and up-converting the frequency and delivering the HF power to the primary coils of the HV transformer. In practice, this is achieved in two steps: firstly, mains frequency is stepped down from 50 Hz (in the UK and Europe) to direct current (DC), which is then up-converted to the operating frequency, typically in a range from tens to hundreds of kilohertz. At these frequencies, the HV transformer works very efficiently, stepping up the voltage to the required peak anode voltage with minimum power loss. The amplified HF voltage is then rectified and smoothed before application across the X-ray tube. HF generators use fast-response closed-loop regulation of exposure factors (kV and mA). The kV pulses applied across the tube approximate a constant potential waveform, apart from a few percent of HF ripple.

The values of the tube voltage used in cardiovascular examinations typically fall in the range of 50–125 kVp, in either pulsed fluoroscopy or serial digital image acquisition. HF generators use fast-response, closed-loop feedback control to automatically regulate the X-ray tube voltage. A potential divider is used to continually sense the kV generated and measure the divergence from the reference kV. The reference kV in this case will be defined by the ADRC system. A device known as a *voltage-controlled oscillator* (VCO) is used to generate the kV correction signal. The correction signal consists of a series of trigger pulses, which have a frequency proportional to the divergence of the actual kV from the reference kV. These trigger pulses are fed back to the power converter to re-establish the reference tube voltage. As a result, the closed-loop regulation system enables the peak tube voltage (kVp) to be rapidly and accurately established and maintained throughout the imaging sequence. In DSA, the kVp must remain constant (within 1% or so) throughout the image acquisition sequence to prevent artifacts following image subtraction.

During pulsed fluoroscopy, the X-ray exposure is delivered as a rapid series of pulses of short duration. The tube current value typically used in pulsed fluoroscopy is ~150 mA. An even higher tube current (from hundreds up to 1000 mA or so) is commonly required in digital image acquisition. A separate fast-response closed-loop regulation circuit is used to control and stabilize the filament current. A sensing voltage is measured across a reference resistor and is used to monitor the actual X-ray tube current. The measured current is compared with the reference current (mA) selected by the automatic exposure regime. Again, any divergence from the reference current is compensated for via a VCO feedback loop. The VCO supplies charge pulses to update the filament current control circuit and stabilize the tube current. Closed-loop regulation of mA automatically compensates for filament aging and the space-charge effect of the X-ray tube, ensuring accurate and reliable dose calibration.

Pulsed fluoroscopy and image acquisition both rely upon the production of a sequence of precise X-ray pulses, sometimes delivered over an extended time period. In the case of fluoroscopy, the run can be many minutes long. In image acquisition, the run is typically 10–20 s long. The duration of the individual X-ray

pulses must be kept as short as possible, consistent with power loading restrictions. In principle, minimum switching times of 1 ms can be achieved using quartz-controlled switching of the electrical power. In cardiac image acquisition, the runs are often captured at a similar frame rate to that used in pulsed fluoroscopy—for example, 15 frames  $s^{-1}$ . In cardiac image acquisition, the dose per frame will typically be 10 (or so) times greater than that used in pulsed fluoroscopy. In vascular applications, image acquisition is often performed at a comparatively low frame rate, say, from a maximum of 6 frames  $s^{-1}$  down to 1 or 0.5 frames  $s^{-1}$ . Again, the optimum frame rate varies with the clinical application. At the same time, the dose per frame, certainly in DSA, has to be increased by a factor of 100 (or so) compared with that used in cardiac acquisition. This is necessary to ensure that the subtracted images have a suitably high  $\Delta$ SNR and therefore low-contrast resolution. X-ray pulse durations in vascular image acquisition are significantly longer than those used in cardiac image acquisition.

#### 11.7.4 Spectral Filter

X-ray imaging systems incorporate hardware in the X-ray tube head to shape and condition the X-ray beam (see [■ Fig. 11.8](#)) [33, 34]. This is required to optimize the radiation field and X-ray spectrum for each type of clinical examination. The X-ray field is shaped using rectilinear lead collimators and semitransparent wedge filters. The former are automatically set to delimit the X-ray field of view (FOV) against changes in the zoom field and the source-to-image detector distance. The operator is also able to manually collimate the X-ray beam to delineate a smaller FOV matched to the clinical region of interest. This is good practice as it both avoids unnecessary patient (and staff) dosing and improves image quality by reducing X-ray scatter. Wedge filters are used to equalize the radiation field incident on the detector across the body section. This reduces flare and contrast loss at interfaces between anatomical regions of comparatively low and high X-ray transmission (e.g., the heart/lung border). Similar techniques are also used in DSA to minimize overexposure of the detector in regions of very high X-ray transmission.



Referring back to the X-ray spectra shown in **Fig. 11.1**, these curves were computed assuming that a standard 3.5 mm-thick aluminum ( $Z = 13$ ) filter was placed in the X-ray beam. The resulting X-ray spectra still contain a complement of low-energy X-ray photons, increasing the patient entrance surface dose but contributing little to the formation of the X-ray image. These low-energy X-ray photons can be reduced further by filtering the X-ray beam (more aggressively) with a thickness of metal of a higher atomic number than aluminum, such as copper (Cu) ( $Z = 29$ ). **Figure 11.13** illustrates the changes to the 80 kVp X-ray spectrum produced by adding 0.1, 0.2, and 0.4 mm-thick copper filters to the X-ray beam. Increasing the thickness of the copper filter attenuates the low-energy photons to an increasing degree. A supplementary copper filter added to the X-ray beam is known as a *spectral filter (shaping filter)*. Spectral filters are used to reduce the risk of deterministic skin injuries, and their use has become standard radiation protection practice in interventional fluoroscopy. Copper spectral filters of a thickness between 0.1 and 0.9 mm are well established in cardiovascular fluoroscopy. Copper spectral filters are also increasingly being used in cardiac and vascular image acquisition. Successful implementation of spectral filters demands the availability of very powerful X-ray tubes with excellent heat management properties, as discussed in **Sect. 11.7.3**.

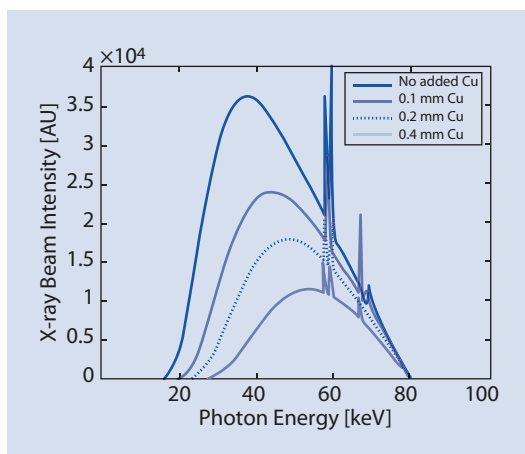


**Fig. 11.13** X-ray spectra for 80 kVp exposure: effects of 0.1, 0.2, and 0.4 mm copper spectral filters. *kVp* peak kilovoltage. (See «Acknowledgments»)

In cardiovascular fluoroscopy of adult patients, the addition of a 0.1 mm-thick copper spectral filter to the X-ray beam can reduce the patient skin dose by ~30–40% (depending upon exact exposure factors and patient size, etc.). In pediatric fluoroscopy, the equivalent dose saving can be up 50%. Addition of a 0.2 mm-thick copper spectral filter in adult fluoroscopy can reduce the skin dose by ~40–60%. As the spectral filter thickness is increased, further dose savings will accrue; for example, a copper filter 0.9 mm-thick can reduce the skin dose by ~60–80%. Beyond this filter thickness, however, the law of diminishing returns applies, and little further dose reduction is to be gained.

It must be noted however that if the *kVp* is kept constant, the addition of a spectral filter will progressively harden the X-ray beam, as shown in **Fig. 11.13**. This will increase X-ray beam penetration and as a result will reduce subject X-ray contrast. For example, addition of a 0.1 mm-thick copper spectral filter reduces vessel subject X-ray contrast by up to 5%. Provided there is sufficient X-ray tube power and heat loading capacity in reserve, this loss of contrast can be ameliorated by retuning the X-ray exposure factors. Typically, this would be achieved by reducing the *kVp* to soften the X-ray beam (somewhat) and boosting the *mA* to compensate for the fall in X-ray tube output.

Rare earth series elements (such as gadolinium (Gd) and erbium (Er)) have been considered as possible alternatives to copper as spectral filter material. For example, recently, a gadolinium spectral filter was investigated for use in pediatric cardiac angiography [35]. One commercial cardiovascular imaging system currently employs a tantalum (Ta) ( $Z = 73$ ) spectral filter. Tantalum has a K-absorption edge at 67.4 keV and as a result reduces not only the contribution of low-energy X-ray photons but also the high-energy X-ray photons that exceed the K-absorption edge. Reportedly, tantalum filters preferentially transmit photons in the midenergy range of the X-ray spectrum (at energies below 67.4 keV), providing good dose savings while better preserving subject X-ray contrast [36]. Currently, however, copper remains the spectral filter material of choice in the majority of cardiovascular imaging installations.



### 11.7.5 Automatic Dose Rate Control

Cardiac and vascular imaging systems incorporate specialized hardware and software to automatically select and stabilize the X-ray exposure factors (and hence operating dose rates) during clinical operation. Until recently, this type of control facility was referred to as *automatic brightness control* (ABC) [37]. Today, the term *automatic dose rate control* (ADRC) is more commonly used (see ■ Fig. 11.8) [38]. To a certain extent, this change in name also marks the increased sophistication of modern automatic dose rate control facilities. ADRC applies to both pulsed fluoroscopy and digital image acquisition. An ADRC system is designed to maintain a constant (target) dose rate at the image detector entrance independently of the patient size (age), the thickness of the body section, the projection angle, the degree of X-ray beam collimation and filtration, and the details of the clinical procedure (e.g., the use of a contrast medium or otherwise). During fluoroscopy, the ADRC typically measures the mean value of the detector signal over a defined (dominant) area at the center of the image field. Feedback control is then used to automatically adjust the X-ray exposure factors to stabilize the detector entrance dose rate. Factors controlled by the ADRC include the peak tube voltage (kVp), the tube current (mA), and the exposure pulse duration. Certain designs of ADRC also automatically select the spectral filter. ADRC ensures that the displayed fluoroscopic images have stable brightness, with no need for the operator to adjust exposure factors manually. In addition, stabilizing the detector entrance dose rate ensures that the level of X-ray quantum noise in the image is constant to help maintain a consistent level of displayed image quality. In fluoroscopy, the operator can normally select a target dose rate, typically from two ADRC settings (say, providing *low dose rate* versus *standard dose rate* options) or three settings (say, *low dose rate* versus *standard dose rate* versus *high image quality* options). These selections typically step the dose rate in increments of a factor of 2 (or so). The operator is free to change the ADRC target dose rate to meet the evolving image quality and dose constraints of each patient examination.

The technical details of an ADRC system vary with the design philosophy adopted by individual manufacturers. Often this information is proprietary and must be solicited from the relevant

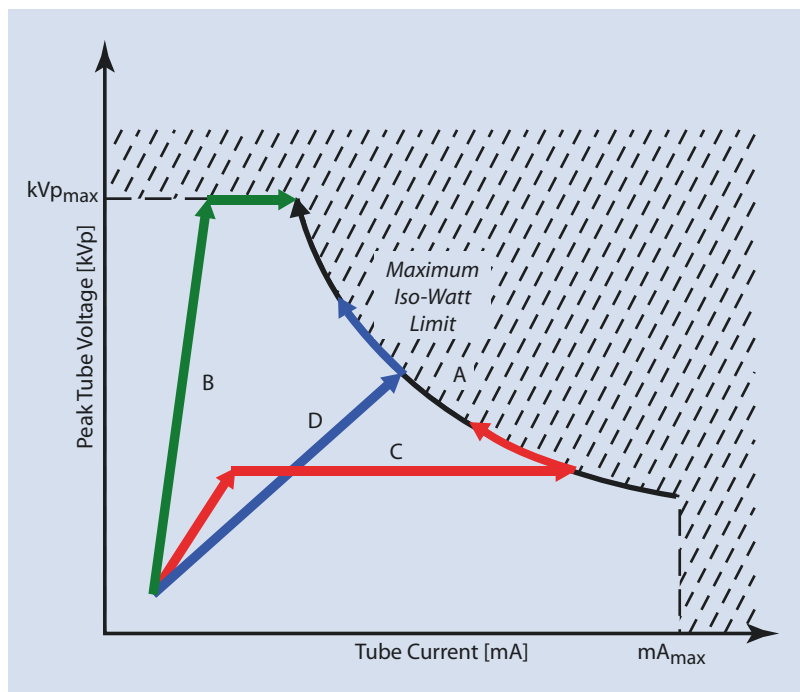
manufacturer. Nevertheless there are some shared principles, which are worth reviewing here. Obviously the ADRC system must operate within the appropriate maximum heat load restrictions and power limits of the X-ray tube and generator. In addition, there are legal limits on the maximum patient dose rates in fluoroscopy, which must never be exceeded. For example, in the USA, the Food and Drug Administration (FDA) prescribes a maximum entrance surface dose rate in fluoroscopy of  $8.8 \text{ cGy min}^{-1}$ ; however, such limits vary in different parts of the world. Within these restrictions, however, the ADRC can be designed to function in a variety of different ways by exploiting different exposure parameter trajectories. These parameter trajectories are designed to achieve particular performance outcomes in clinical use. Four potential fluoroscopic ADRC trajectories are depicted in ■ Fig. 11.14. These trajectories essentially describe the kVp versus mA response of the ADRC to patients of increasing thickness (as indicated by the directions of the arrows in the graph). The periphery of the zone delineating the ADRC response, given by the hatched area, is defined by the maximum electrical limits of the X-ray source and generator.

Curve A (in black) represents the so-called *isowatt ADRC algorithm*, which functions by holding the  $[\text{kVp} \times \text{mA}]$  product at the constant maximum value. As patient thickness increases, the kVp increases monotonically, while the mA falls, following the maximum isowatt limit curve. This ADRC algorithm makes maximum use of the power capabilities of the X-ray source.

Curve B (in green) represents a *low-dose ADRC algorithm* where the kVp (and the penetration of the X-ray beam) increases rapidly as the patient thickness increases, keeping the entrance surface dose rate at a minimum. It is only after the maximum kVp limit is reached that the mA increases significantly, and this can only continue until the maximum isowatt rating curve is intersected. Associated with the rapid increase in kVp is a reduction in subject X-ray contrast however. This ADRC algorithm might be used where dose reduction is the overriding consideration and image quality is secondary.

Curve C (in red) represents a *high-contrast* (iodine-sensitive) ADRC algorithm, which is often used in vascular imaging. Here the kVp is held at a value in the range of 63–66 kV to maximize subject X-ray contrast of iodinated contrast media.

**Fig. 11.14** Typical automatic dose rate control (ADRC) parameter trajectories (peak kilovoltage (kVp) versus tube current in milliamps (mA)): curve A isowatt algorithm (black), curve B low-dose algorithm (green), curve C high-contrast (iodine-sensitive) algorithm (red), and curve D anti-isowatt algorithm (blue)



This kVp is used to exploit the K-absorption edge of iodine at 33.2 keV. An increase in patient thickness inevitably demands an increase in mA up to the point where the maximum isowatt curve is intersected. Beyond this, the kVp must increase and the mA must fall, again following the maximum isowatt curve. This ADRC algorithm maximizes subject X-ray contrast but potentially at a cost of an increased patient dose.

Curve D (blue) is a so-called *anti-isowatt ADRC algorithm* where the kVp and mA increase together, up to the point where the maximum isowatt curve is intersected. Beyond this, the kVp increases, and the mA falls and follows the maximum isowatt curve. This curve represents a compromise between algorithms B and C, with a balanced trade-off between the patient dose and image quality.

ADRC systems designed for cardiovascular imaging may also feature automatic selection of the thickness of the copper spectral filter against patient size [38]. This facility uses a motorized wheel containing a set of copper plates of different thickness, mounted in the collimator housing. Automatic copper spectral filter selection is integrated with the more familiar autoregulation of kV and mA (discussed above). Arguably, this arrangement can further refine the trade-off

between dose and image quality, across the range of patient sizes. Such designs of ADRC algorithm may measure/estimate the image quality and dose, and derive an FOM to use in parameter selection. Such efforts are aimed at further improving the congruence of ADRC (and hence imaging system) operation with the ALARA principle.

In serial image acquisition, the selection of exposure factors (and potentially the spectral filter) by the ADRC is typically founded upon the parameters set up in the preceding fluoroscopy run. The fluoroscopic exposure factors are typically first used to estimate an equivalent water thickness for the patient. It should be noted that identical factors are not used, but a suitable transformation is required to cross over from optimum fluoroscopy to optimum acquisition parameters. Finally, adaptive tuning of exposure factors occurs during the early frames of the acquisition run to compensate for the actual patient attenuation characteristics (including composition of the body section). In practice, dose stabilization is achieved within the first few frames of the start of the run and is therefore not normally a distraction to the viewer. Significantly, the dose overhead is therefore also kept to a minimum. This ADRC approach is adequate for purpose in

cardiac X-ray image acquisition, where constancy of the exposure factors throughout the run is not essential.

In DSA, however, the image signal, and hence exposure factors, must be held constant within tight limits, throughout both the mask (precontrast) and the contrast medium-enhanced phases of the exposure run. Even modest variations in exposure can result in unacceptable artifacts in the viewed image sequence following digital subtraction. Consequently, ADRC algorithms designed for DSA often use initial *low-dose* test shots to estimate the exposure factors to be used in the acquisition run proper. The selected exposure factors are then held constant (locked) throughout the image acquisition sequence. Locked exposure factors are also required during RA image acquisition.

Fluoroscopy systems normally incorporate a second feedback control, which automatically stabilizes electronic gain, *not* the dose rate. This facility is known as *automatic gain control* (AGC). The AGC is particularly helpful under conditions where the ADRC is no longer able to achieve the target detector dose rate; this condition is sometimes referred to as «running out of steam» and can occur, for example, when imaging the bariatric patient and where the maximum patient dose rate limit has been reached. The AGC automatically adjusts the electronic gain to compensate for the shortfall in signal amplitude. This maintains the brightness of the displayed image, so the interventionalist can continue the examination, albeit that the image quality is degraded by increased noise fluctuations.

## 11.8 Dynamic X-Ray Image Detectors

### 11.8.1 X-Ray Image Intensifier Television System

Up to the turn of the new millennium, the dynamic image detector used in cardiovascular imaging was the X-ray image intensifier television (IITV) system [39, 40]. This system comprised a chain of electron-optical components, including an X-ray image intensifier tube plus a high-specification closed-circuit TV channel, along with coupling lenses [41, 42]. Historically, TV images were recorded via a vacuum electron-tube

camera such as a Plumbicon, Chalnicon, Saticon, or Newvicon. More modern X-ray IITV systems replaced the electron-tube camera with a semiconductor sensor known as a *charge-coupled device* (CCD). CCD sensors are solid-state TV cameras with superior, more stable technical characteristics than the earlier electron-tube camera [43]. The resulting video images can be presented live on a display monitor and/or digitized prior to image processing and viewing. A number of review articles have described the design characteristics of X-ray IITV (including CCD)-based fluoroscopy systems.

The emergence of DSA imaging equipment in the early 1980s established the clinical benefits of integrating computerized video processors and magnetic disk storage with X-ray IITV systems. The success of DSA established digital serial image acquisition in vascular diagnosis and treatment. This subsequently led to further important innovations, such as dedicated digital grayscale X-ray imaging devices for cardiac applications. Advances in digital X-ray IITV detectors led to the demise of film as the principal recording medium in cardiac and vascular imaging. Digital X-ray IITV imaging made it possible to acquire, access, and replay sequences of images online and view the images in a digitally enhanced form. At the same time, image-processing algorithms to facilitate patient dose savings—such as digital recursive filtering, last image hold, and 2D road mapping—boosted the clinical utility and acceptance of digital fluoroscopy [42, 44, 45]. By the turn of the millennium, digital X-ray image-intensified CCD (IICCD) systems had proved to be an effective and flexible platform for cardiovascular imaging [46]. Around this time, however, a new generation of dynamic X-ray image detectors emerged, based upon solid-state electronics. In the intervening decade, these detectors have gone on to replace digital X-ray IITV technologies in many cardiovascular facilities across the world.

### 11.8.2 Solid-State X-Ray Image Detector

Solid-state detectors were originally designed for use in standard-projection radiography [47]. These digital radiography (DR) detectors provided online access to the electronic data, so the

images became available for viewing in a matter of seconds after the exposure (rather than after the lengthy delay more typical of film-based radiography). Significantly, researchers found that with suitable adaptation, solid-state DR detectors could equally well be used to record images at rates high enough to support fluoroscopy [48, 49]. Prototype clinical dynamic solid-state detector systems started to appear toward the end of the 1990s [50–56]. The first commercial solid-state detector-based digital fluoroscopy products appeared in 2001; these dynamic flat-panel detectors (FDs) were designed specifically for cardiac imaging [57–59]. Since then, all newly installed cardiac catheterization laboratories have utilized dynamic solid-state detectors (ousting the X-ray IITV from one of its pre-eminent roles). With the subsequent introduction of dynamic solid-state detectors of a much larger FOV, a rapid shift away from digital X-ray IITV systems is now occurring in vascular imaging [60–65].

Dynamic solid-state detectors used in cardiovascular imaging comprise a layer of X-ray-sensitive material (viz., either an X-ray phosphor scintillator or an X-ray photoconductor) coated upon a layer of semiconductor material, which contains the active matrix array of electronic components. These two layers are mounted on a glass substrate and housed in an evacuated container. The whole detector assembly—including power supplies, amplifiers, and readout electronics—is housed within a compact flat-panel enclosure. This gives rise to the commonly used term *flat-panel detector* (FD), which is applied to these devices. Currently, the majority of dynamic FDs used in cardiovascular imaging exploit the so-called *indirect-conversion principle*. Dynamic detectors exploiting direct conversion do exist but are less widely used in current systems and so are discussed only briefly here; however, the interested reader is referred to relevant review articles [66, 67]. Suffice it to say, direct-conversion FDs convert the incident X-ray photon energy (exiting the patient) directly into electronic charge carriers in a layer of amorphous selenium (a-Se). On the other hand, indirect-conversion FDs convert the X-ray photon energy into an electrical charge via an intermediary stage in which fluorescent light is emitted by the X-ray phosphor scintillator.

### 11.8.3 Indirect-Conversion Dynamic Flat-Panel Detector

Current indirect-conversion FDs utilize a layer of thallium (Tl)-activated cesium iodide (CsI:Tl) as a scintillator. This scintillator absorbs (a major proportion of) the incident X-ray photon energy. The absorbed X-ray energy is first converted to light photons, then this absorbed light energy in a photosensor is transferred to free charge carriers, which are used to form the electronic image. CsI:Tl is an excellent X-ray absorber, combining two elements—cesium (Cs) and iodine (I)—of (comparatively) high atomic numbers ( $Z = 55$  and  $53$ , respectively). The cesium and iodine atoms also exhibit strong K-absorption edges at (and above) 36 and 33 keV, respectively. These K-edges boost the absorption of X-ray photons at energies relevant to cardiovascular imaging with an iodinated contrast medium. Importantly, the CsI:Tl layer is manufactured in the form of densely packed, microscopic, needle-shaped crystals. As a result, the CsI:Tl layer acts like a fiber-optic plate channeling the fluorescent light along individual needle crystals down to the amorphous silicon (a-Si) sensor surface. The *channeled scintillator* structure helps to moderate the scattering of light photons and hence the blurring (unsharpness) of recorded image details. As a result, comparatively thick layers of CsI:Tl are used to maximize X-ray absorption efficiency, but importantly, image sharpness is not sacrificed (as occurred in traditional granular phosphor screens). Dynamic indirect-conversion FDs typically use a 550 to 650  $\mu\text{m}$ -thick layer of CsI:Tl. Such a layer will typically absorb 80–90% of the incident X-ray photons.

Each X-ray photon interaction in CsI:Tl gives rise to  $\sim 3000$  green light photons, of which around 50% will contribute to the electronic signal. A light reflector is often coated on the top surface of the CsI:Tl to maximize the signal. The light emitted by the CsI:Tl layer is converted to the electronic signal in a 2D array of picture elements (pixels) fabricated in a thin layer of (hydrogenated) amorphous silicon (a-Si:H). The amorphous (viz., unstructured) form of silicon (Si) is favored over the more familiar crystalline form (which is used in the fabrication of standard microchips, CCD sensors, etc.). Amorphous silicon can be used to fabricate semiconductor arrays of a large area

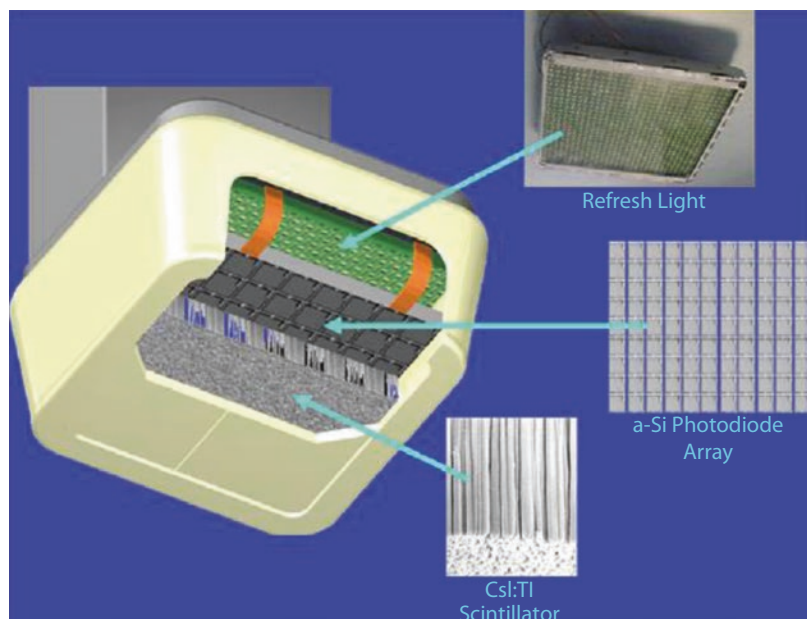
(equivalent to the size of a body section) at a reasonable cost. Additionally, amorphous silicon-based FDs are immune to damage from repeated exposure to high-intensity X-ray beams. Each pixel in the active matrix (AM) array comprises a light-sensitive cell (a photodiode) plus a switching component in the form of a thin film transistor (TFT) switch. The quantity of charge carriers released in each photodiode is proportional to the intensity of the X-ray beam at that location. Each TFT switch in the array is addressed via a matrix of (horizontal) gate control lines and (vertical) data transfer lines. During the X-ray exposure, all of the TFT switches in the array are held «open» so that packets of electronic charge accumulate in local storage capacitors. At the end of the X-ray exposure, the resulting 2D pattern of the electrical charge is read out by gating each row of pixels in the AM array in turn. The readout charge is amplified prior to digitization and transfer to the system computer. The dynamic FD is exposed to repeated pulses of X-rays, and the resulting patterns of charge are read out, producing a sequence of frames. Depending upon the dose levels used, the sequence of frames will constitute fluoroscopy or serial image acquisition.

The internal construction of a commonly used dynamic FD is shown in [Fig. 11.15](#). The components of the detector identified in this figure include the CsI:Tl X-ray absorption layer, the surface light reflector, the amorphous silicon

AM electronics array, and the glass substrate. This design of dynamic FD also incorporates a refresh light source (comprising an array of light-emitting diodes (LEDs)), whose function is discussed in [▶ Sect. 11.9](#). The FD depicted is the Pixium 4800 (Trixell SAS, Moirans, France). This FD is manufactured specifically for use in cardiac imaging applications and has a square FOV of a maximum diagonal size of  $\sim 25$  cm (248 mm to be precise), with two zoom field modes of  $\sim 202$  mm and 156 mm diagonal size, respectively. The pixel-sampling interval is 184  $\mu\text{m}$ , and the bit resolution of the ADC is 14 bits. This detector can support an imaging rate of up to 30 frames  $\text{s}^{-1}$  at full pixel resolution and 60 frames  $\text{s}^{-1}$  with pixel binning (binning is explained in [▶ Sect. 11.9.4](#)).

A biplane dynamic FD-based vascular interventional lab is shown in [Fig. 11.16](#); this is a mock-up but clearly shows salient equipment component. The digital imaging channels that are featured incorporate the Pixium 4700 dynamic FD (Trixell SAS), which also exploits the indirect-conversion principle. This FD has a nominal maximum FOV of [38 cm  $\times$  30 cm] ([381.9 cm  $\times$  294.1 cm] to be precise). The FD also provides multiple zoom field options; details of the available zoom field modes vary with the equipment manufacturer. For the system presented, seven zoom selections are provided, covering from [30 cm  $\times$  30 cm] through [19 cm  $\times$  19 cm] down to [11 cm  $\times$  11 cm] in the maximum zoom

**Fig. 11.15** Construction of a dynamic flat-panel detector (FD) designed for cardiac imaging. (See «Acknowledgments»)





■ **Fig. 11.16** Biplane neurovascular interventional lab (mock-up) featuring large field-of-view (FOV) dynamic flat-panel detectors (FDs). (See «Acknowledgments»)



field selection. The pixel-sampling interval is  $154\ \mu\text{m}$ , and the bit resolution of the ADC is 14 bits. The zoom field selections present images with a square format. Square-format images are also used in fluoroscopy. High-frame-rate pulsed fluoroscopy is achieved by using pixel binning.

The Pixium 4700 detector is incorporated into several vascular (and some cardiac) imaging systems manufactured by Philips Healthcare (shown in ■ Fig. 11.16) and Siemens Medical Solutions in Europe. Other major manufacturers of (indirect-conversion) dynamic FD-based imaging systems include GE Healthcare and Varian Medical Systems in the USA. Certain other manufacturers use direct-conversion solid-state detector systems in their cardiovascular imaging products.

## 11.9 Image Quality of Dynamic Flat-Panel Detectors

All of the diagnostic and interventional cardiovascular imaging roles traditionally supported by the X-ray IITV chain are now reproduced—indeed improved upon—by dynamic FDs. These detectors are much more compact and lighter in weight than the bulky IITV imaging chain. The compact nature of the FD streamlines C-arm design, increasing maneuverability around and accessibility to the patient. FDs are electrically and opto-mechanically much more stable than

IITV channels and therefore less susceptible to changes in performance over time—for example, due to thermal drift. They are also insensitive to the magnetic and environmental effects that can adversely affect IITV systems. For cardiovascular imaging applications, overall, the dynamic FD represents a superior imaging platform to the digital X-ray IITV system.

The physical image quality of medical X-ray image detectors including dynamic FDs can be evaluated using a measurement tool kit including the dynamic range, geometrical distortion, vignetting and veiling glare, spatial resolution, lag (memory effect), and detective quantum efficiency (DQE). These measures are transportable across different designs of X-ray image detector, and the results can be used to compare performance on an objective basis. ▶ Sects. 11.9.1, 11.9.2, 11.9.3, 11.9.4, 11.9.5, and 11.9.6 focus on the physical imaging performance of the new dynamic FDs, where appropriate results are compared with those produced by a digital X-ray IITV system.

### 11.9.1 Dynamic Range

In basic terms, the dynamic range of an FD describes the range of the detector entrance dose over which information can be usefully recorded. The dynamic range is related to the ratio of the



maximum to the minimum entrance dose levels that the detector can accommodate. More specifically, the former is defined by the maximum signal capability of the detector and the latter by the noise base. A dynamic FD normally operates as a multifunctional image receptor and, as such, must be capable of operating over a wide range of dose levels [68]. For example, low-dose pulsed fluoroscopy demands effective image recording down to a mean detector entrance dose of only 10 nGy per frame (or so). In high-quality dynamic image acquisition, the mean detector entrance dose is typically increased to  $\sim 100$  nGy or 1  $\mu\text{Gy}$  per frame, depending upon the imaging mode. The former (lower) value is typical of the dose per frame used in cardiac digital image acquisition; these images are commonly acquired at a frame rate of 15 frames  $\text{s}^{-1}$ . The higher dose value is typical of that used in vascular grayscale image acquisition. In DSA, the mean detector entrance dose can reach radiographic dose levels, viz., up to 4 or 5  $\mu\text{Gy}$  per frame or so. FDs have a maximum dose capability somewhat greater than this (by a factor of  $\sim 10$ ); above this dose, overload of the FD will occur, producing signal saturation. Tube camera-based X-ray IITV systems were particularly susceptible to highlight overloads and blooming (the spurious spread of the saturated signal); these effects would, for example, occur between the lower limbs during peripheral angiography or over the lungs in pulmonary artery studies. Semitransparent wedge filters were developed to ameliorate these effects; this facility has been retained with FD-based imaging equipment.

For dynamic FDs, signals are normally digitized with 14 bits of grayscale resolution (corresponding to 16,384 levels). FDs used in fluoroscopy reportedly offer a dynamic range 10–100 times wider than an X-ray IITV system [8, 69]. In order to accommodate this range of dose levels, dynamic FDs incorporate more than one preamplifier gain setting. The appropriate gain setting is selected automatically to scale the signal range achieved in each imaging mode. This ensures that the signal digitization yields optimum grayscale resolution and the impact of the noise injected by the readout electronics is kept to minimum. Dynamic FDs have an accurate linear signal response across the dynamic range and can support accurate logarithmic subtraction of image data during DSA [61]. Dynamic FDs are increasingly being used in 3D reconstructive

imaging, an application that places even heavier demands on detector dynamic range. For example, the dynamic range of an MSCT scanner approaches  $10^6:1$  with 20-bit equivalent digitization. To compete with this, future designs of FD are likely to implement 16- or 18-bit digitization plus signal-sensitive gain selection [70, 71]. FDs employing such an *extended dynamic range* design will improve the depth of information in the projection images and hence the quality of the 3D reconstructions.

### 11.9.2 Geometry and Vignetting

Images acquired with an X-ray IITV system are susceptible to certain field-dependent artifacts, which can degrade their cosmetic quality. Geometrical distortion in an X-ray IITV image arises from the electron-optical design of the X-ray image intensifier tube. The mapping of electrons from the concave photocathode onto a planar output screen results in a form of geometrical distortion known as *pincushion distortion*. Pincushion distortion describes the progressive increase in geometrical magnification toward the periphery of the image field. At the same time, the luminance of the image field falls off toward the periphery, producing a nonuniform distribution in brightness (so-called *vignetting*). Image intensifiers are also subject to a characteristic form of geometrical distortion due to extraneous magnetic fields, which is known as *S-distortion*. The impact of S-distortion on image quality is compounded by the fact that it varies with the changing angulation of the C-arm; this effect is felt most strongly in RA and related reconstructive imaging applications. FDs are subject to none of these forms of geometrical distortion and therefore can record images with excellent field homogeneity. FDs are insensitive to magnetic fields and therefore can be successfully implemented in hybrid X-ray/MR imaging laboratories [72] or in conjunction with magnetic catheter navigation equipment [68].

### 11.9.3 Veiling Glare (Low-Frequency Drop)

Images produced by an X-ray IITV system are subject to the scatter of X-rays, electrons, and light over a large area, which arise at various stages of

image conversion. The term *veiling glare* is used to describe the overall effect of these scatter mechanisms. The presence of veiling glare degrades the contrast of recorded images. Veiling glare is often quantified in terms of the low-frequency drop (LFD); this concept is derived from the modulation transfer function (MTF). MTF is used to describe the detailed spatial resolution properties of X-ray image detectors [47]. The LFD measures the deterioration in MTF that is attributable to the large-area scatter mechanisms. A high value of LFD implies poor reproduction of large-area contrast by the image detector, and vice versa. Dynamic FDs naturally exhibit a much lower-value LFD and therefore less contrast loss than an X-ray IITV system; contrast is typically improved by a factor of 5–10 with the FD [55]. Consequently, dynamic FDs produce 2D projection and 3D reconstruction images with superior low-contrast sensitivity (and a wider dynamic range) than X-ray IITV systems.

#### 11.9.4 Spatial Resolution

The spatial resolution of an X-ray image detector measures its capacity to resolve small and fine-detail structures in an image. The spatial resolution of a dynamic FD is influenced by a number of physical and technical factors. For example, the sizes of the FD pixel-sampling interval and effective aperture plus the bandwidth of the readout

electronics all contribute to this. In the case of an indirect-conversion dynamic FD, the scatter and diffusion of fluorescent light in the X-ray absorption layer also contribute to image blur, albeit to a moderate degree due to the channeled structure of the CsI:Tl scintillator. Typical spatial resolution properties of indirect-conversion dynamic FDs designed for cardiac and vascular applications are summarized in Table 11.1. Equivalent values for a digital X-ray IITV system are included for reference. Comparing results in the largest FOV selection, the spatial resolution of a large-FOV dynamic FD typically exceeds that of a digital X-ray IITV system by over a factor of 2 or so. The excellent spatial resolution of the FD is maintained across the whole image field. For the digital X-ray IITV system, the spatial resolution is only maintained within a quality area at the center of the image field and deteriorates toward the periphery.

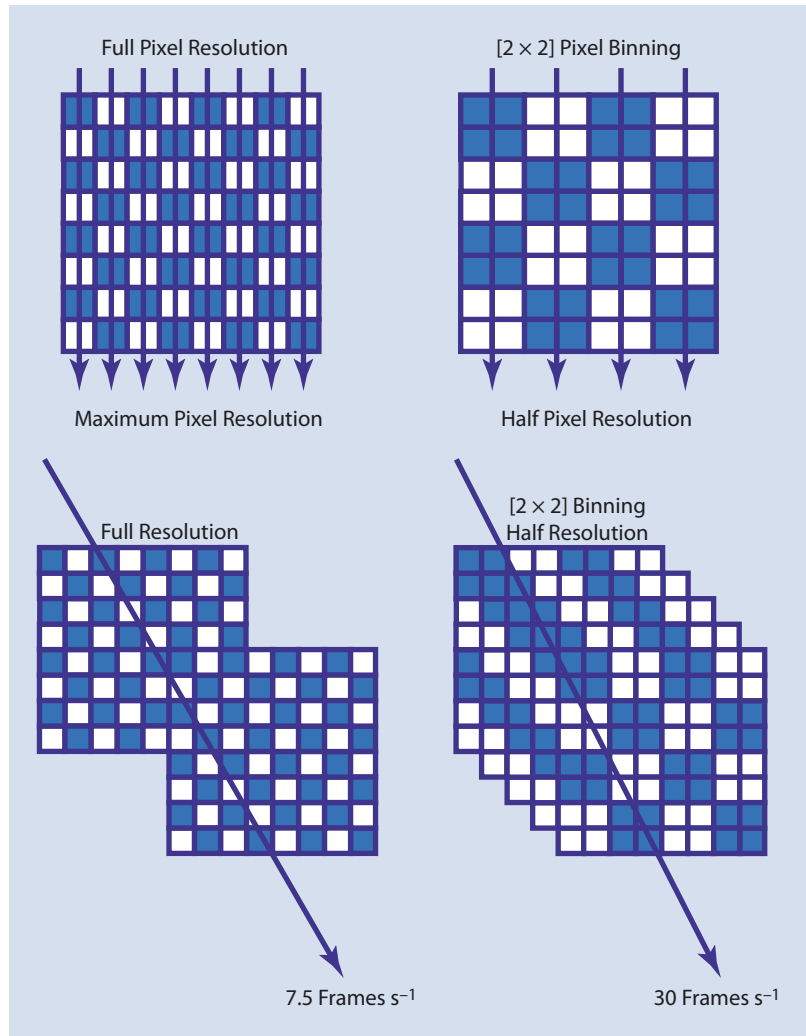
*lp* line pairs

For a large-FOV dynamic FD, typical of that used in vascular imaging, the high frame rates (say, 15 or 30 frames  $s^{-1}$ ) sometimes required in fluoroscopy can usually only be achieved by binning (averaging) data over blocks of pixels. The process of binning pixel data over  $[2 \times 2]$  blocks is illustrated schematically in the top two diagrams in Fig. 11.17. It must be noted that binning inevitably reduces the spatial resolution (by a factor of 2 in each linear dimension) (see Table 11.1). At the same time, however, binning

Table 11.1 Spatial resolution of dynamic flat-panel detectors (FDs) designed for cardiac and vascular imaging: results compared with a large field-of-view (FOV) digital X-ray image intensifier television (IITV) system

	Cardiac FD	Vascular FD	Vascular FD	Digital IITV	Vascular FD	Digital IITV
	Maximum FOV	Maximum FOV	$[2 \times 2]$ pixel binning	Maximum FOV	Zoom field	Zoom field
FOV	Square field	Rectangular field	Square field	Circular field	Square field	Circular field
	[24.8 cm $\times$ 24.8 cm]	[38.2 cm $\times$ 29.4 cm]	[29.4 cm $\times$ 29.4 cm]	35 cm diameter	[13.5 cm $\times$ 13.5 cm]	14 cm diameter
Pixel-sampling interval ( $\mu\text{m}$ )	184	154	308	341	154	137
Pixel array	956 $\times$ 954	2480 $\times$ 1910	1240 $\times$ 955	1024 $\times$ 1024	1024 $\times$ 1024	1024 $\times$ 1024
Spatial frequency ( $\text{lp mm}^{-1}$ )	2.72	3.25	1.625	1.46	3.25	3.65

■ **Fig. 11.17** Schematic diagram of pixel binning (as used in flat-panel detectors (FDs)), illustrating its impact on spatial resolution and data transfer rates



reduces the total number of pixels to be read out in each fluoroscopic frame, by a factor of 4. As a result, the presentation of sequences of large-FOV images at a 4× higher frame rate becomes feasible (for the same readout bandwidth). In other words, if the maximum frame rate for full-resolution imaging is 7.5 frames  $s^{-1}$ , then if pixel binning is used, the maximum frame rate increases to 30 frames  $s^{-1}$ , as illustrated in the bottom two diagrams in ■ Fig. 11.17. Fortunately, in fluoroscopy the associated reduction in spatial resolution is usually not intrusive, as this is partially offset by the accompanying smoothing of noise fluctuations.

During fluoroscopy the interventionalist often needs to select a detector zoom field to magnify the presented image and therefore improve the visibility of fine-detail structures. (Obviously

accompanying this is a reduction in detector FOV and therefore anatomical coverage.) For a digital X-ray IITV system, the spatial resolution is materially improved when an electronic zoom field is selected; this is due to the rescaling of the image projected on the TV sensor. Selecting the maximum IITV zoom field can more than double the spatial resolution compared with that for the largest FOV selection. Dynamic FDs also provide multiple zoom field selections. In contrast to the digital X-ray IITV system, the intrinsic pixel resolution of an FD remains constant, independently of the zoom field that is selected. This obviously is not the case if pixel binning is applied; in this case, the spatial resolution is typically reduced by a factor of 2.

In IITV-based fluoroscopy, the selection of an electronic zoom field is invariably accompanied

by an increase in the X-ray dose per frame delivered at the image intensifier, II, entrance. In turn, this leads to an increase in the patient dose. In going from the largest FOV to the maximum zoom field selection, the II (and potentially patient) entrance dose may be increased by a factor of 4 or more. This is required (at least in part) to compensate for the fall in the II brightness gain with an increasing zoom factor. In a digital X-ray IITV system, the zoom-dependent increments in dose are fixed. In theory, for a dynamic FD, such zoom-dependent dose increments are not necessary; in practice, however, they are still often used to maintain the visual quality of the images. The dose increments used with an FD are often less severe than those required by an X-ray IITV system [69]. With an FD, these dose increments must be carefully matched to the image quality needs and dose constraints of the individual clinical examination. Some examinations may favor an FD entrance dose increment of, say, 20–40% (or so) between zoom field selections, while other examinations may not need an increment in dose with zoom field selection. The spatial resolution of a large-FOV dynamic FD can be gauged from the abdominal DSA image presented in **Fig. 11.18**. Small vessels in the vascular bed are uniformly depicted with excellent spatial resolution throughout the whole image field.



**Fig. 11.18** Sample abdominal digital subtraction angiography (DSA) image acquired with a large field-of-view (FOV) dynamic flat-panel detector (FD). (See «Acknowledgments»)

### 11.9.5 Lag and Memory Effect

Understandably, dynamic FDs must be capable of recording fluoroscopic images with sufficient temporal resolution to meet the needs of the target clinical examination(s). For example, in cardiac angiography, the mean velocity of a coronary vessel [73] typically measures  $\sim 50 \text{ mm s}^{-1}$ , while the peak velocity can exceed  $100 \text{ mm s}^{-1}$ ; clearly, high temporal resolution and frame rates are essential in coronary angiography. Imaging other types of vascular structures can often be performed satisfactorily using a lower temporal resolution and frame rate. The temporal response of a dynamic FD is determined by two physical mechanisms [74]: the *memory effect* (or *ghosting*) and *lag*. These mechanisms occur concurrently; under a given set of circumstances, a detailed experimental analysis is required to distinguish and quantify their contributions.

Memory effect refers to the production of a spurious frozen pattern (a so-called *ghost image*), which mirrors the image content present in the preceding X-ray exposure. This phenomenon can persist for some time (even for several minutes), particularly after an intense X-ray exposure of a high-contrast structure is made [75]. Memory effect reflects a variation in the detector response depending upon the exposure history. Both indirect- and direct-conversion FDs are susceptible to memory effect; however, they result from quite different physical mechanisms. In general, the latter design of FD is more susceptible to ghosting artifacts [32]. With regard to indirect-conversion FDs, memory effect represents an increase in CsI:Tl light emission and a-Si:H photodiode gain, following the X-ray exposure. These effects manifest themselves as a spurious increase in detector conversion efficiency, producing a so-called *bright-burn artifact* in images that are acquired subsequently. Memory effect can prove to be a particular problem in mixed-mode imaging applications, specifically where low-dose fluoroscopy might follow immediately after the acquisition of images at a high dose level—for example, as routinely occurs in DSA [68]. The X-ray dose per frame during fluoroscopy can be as low as one thousandth of that used during DSA image acquisition. Therefore, even a modest degree of memory effect can in principle impinge upon the fluoroscopic images that follow.

Lag is the property that quantifies the ability of an image detector to accurately record time-varying changes in image content. Lag can cause smearing of rapidly moving and time-varying image structures. The larger the detector lag, the poorer (slower) the temporal response, and vice versa. Lag results from the carry-over of a proportion of the recorded signal content into succeeding frames in the sequence. In indirect-conversion FDs, lag largely results from the relatively slow temporal response of the a-Si:H layer. More specifically, lag arises from the trapping and slow release (detrapping) of charge carriers in the photodiode array [76].

Dynamic FDs must incorporate measures to minimize lag and memory effect. Many modern dynamic FDs achieve this via a so-called *refresh light* (or *reset light*), which conditions the detector with a bright flash of light prior to each new image acquisition cycle [76, 77]. The refresh light takes the form of an array of light-emitting diodes, which instantaneously flood the FD with light photons, thereby saturating the charge traps in the a-Si:H prior to each new X-ray exposure. As a result, lag (and memory effect) is reduced to an acceptably low level, ensuring an acceptable detector response for most 2D and 3D imaging applications. Signal retention due to lag in a modern indirect-conversion FD is reportedly as low as 0.3% at a time 1 s after termination of the X-ray exposure; after 10 s, the lag reduces by a further order of magnitude [68]. This ensures that the temporal resolution is adequate even for high-speed imaging applications such as pediatric cardiac fluoroscopy. Equivalent values of lag for direct-conversion FDs are reportedly much higher [68]. In some vascular applications, a moderate degree of lag can be tolerated during fluoroscopy. Indeed, lag can sometimes help to improve fluoroscopic image quality by time-averaging (smoothing) noise fluctuations. In modern cardiovascular imaging systems, lag is synthesized via a computer processing algorithm (such as recursive filtering). This makes it possible to automatically adjust the degree of lag to maintain image quality, as circumstances demand.

The presence of lag and memory effects in a dynamic FD sets a limit on the maximum rate at which projection data can be usefully acquired for 3D reconstructive imaging. The spurious carry-over of signal content into subsequent projections gives rise to artifacts and unsharpness in the

reconstructed images. It should be noted that in these applications, afterglow in the CsI:Tl scintillator also becomes a significant factor. For these reasons, the maximum frame rate used in RA acquisition is often limited to 15 or 30 frames  $s^{-1}$ .

### 11.9.6 Detective Quantum Efficiency

Detective quantum efficiency (DQE) is currently the most influential physical parameter used to quantify (and compare) the performance of X-ray image detectors [78]. DQE describes the efficiency with which an X-ray image detector can record information delivered in the incident (input) X-ray beam. As such, the DQE of an X-ray image detector is defined by the ratio [47, 78]:

$$DQE_{\text{detector}} = \text{SNR}_{\text{recorded}}^2 / \text{SNR}_{\text{input}}^2$$

where:

$\text{SNR}_{\text{input}}^2$  is the square of the signal-to-noise ratio at the input of the image detector. This is defined by the fluence (number or count per unit area) of X-ray photons contributing to an individual frame in the fluoroscopic image sequence. The value of  $\text{SNR}_{\text{input}}^2$  can be calculated knowing the detector entrance dose per frame utilized and the energy spectrum of the incident X-ray beam.

$\text{SNR}_{\text{recorded}}^2$  is the square of the signal-to-noise ratio recorded by the image detector. The value of  $\text{SNR}_{\text{recorded}}^2$  can be computed from the output image data. In terms of counting statistics,  $\text{SNR}_{\text{recorded}}^2$  is an estimate of the fluence of information carriers (X-ray photons) that the recorded image is effectively worth. (Note: to simplify the discussion here, it is assumed that the fluoroscopic image detector exhibits zero lag, or that any lag that does exist is corrected.)

The information recorded by an image detector can never exceed that delivered by the input X-ray beam; therefore, DQE always has a value in the range:

$$0 \leq DQE_{\text{detector}} \leq 1$$

A DQE value of unity implies that the detector records the incoming X-ray information perfectly. At the other extreme, a DQE of zero implies that no information at all is recorded. Real-world X-ray image detectors, and obviously the DQE,

have a value falling somewhere between these two extremes. The deterioration in recorded information occurs for two principal reasons. Firstly, no detector can absorb all of the incident X-ray photons with 100% efficiency, and therefore some photons are lost to the image detection process. Inevitably, some X-ray photons pass straight through the X-ray absorber, while others that are absorbed may then be re-emitted and escape the detector. This loss in primary X-ray information is compounded by various other noise sources in the detector itself; an important example is the electronic noise that arises in the a-Si:H matrix array and the signal readout circuitry. The DQE of a modern indirect-conversion dynamic FD typically lies in the range of 0.70–0.80 for X-ray beam energies used in cardiovascular imaging [57, 58, 79]. Direct-conversion dynamic FDs typically have a somewhat lower DQE, with a value in the range of 0.50–0.60 [65].

The influence of electronic noise on detector DQE performance varies strongly with the signal level (and therefore the detector entrance dose).

Indeed, the variation of DQE with the incident detector dose is an important characteristic of dynamic detector performance. This can be analyzed by measuring how DQE varies as a function of the detector entrance dose per frame. In early designs of dynamic FD, the image quality in fluoroscopy fell below that of the digital X-ray IITV system; this was due to the comparatively powerful contribution of electronic noise in the FD designs at that time [48, 51, 63, 80]. Today, this is no longer an issue. Typical DQE performance for a modern indirect-conversion FD is summarized in Fig. 11.19. Equivalent results for a modern digital X-ray IITV system are included for reference. The ranges of the detector doses used in standard fluoroscopy, digital cardiac acquisition, digital grayscale angiography, and DSA (where the dose per frame may reach or even exceed that used in screen film radiography) are demarcated for reader orientation. The high DQE of the indirect-conversion FD is maintained across the majority of the dynamic range. At best, FD DQE

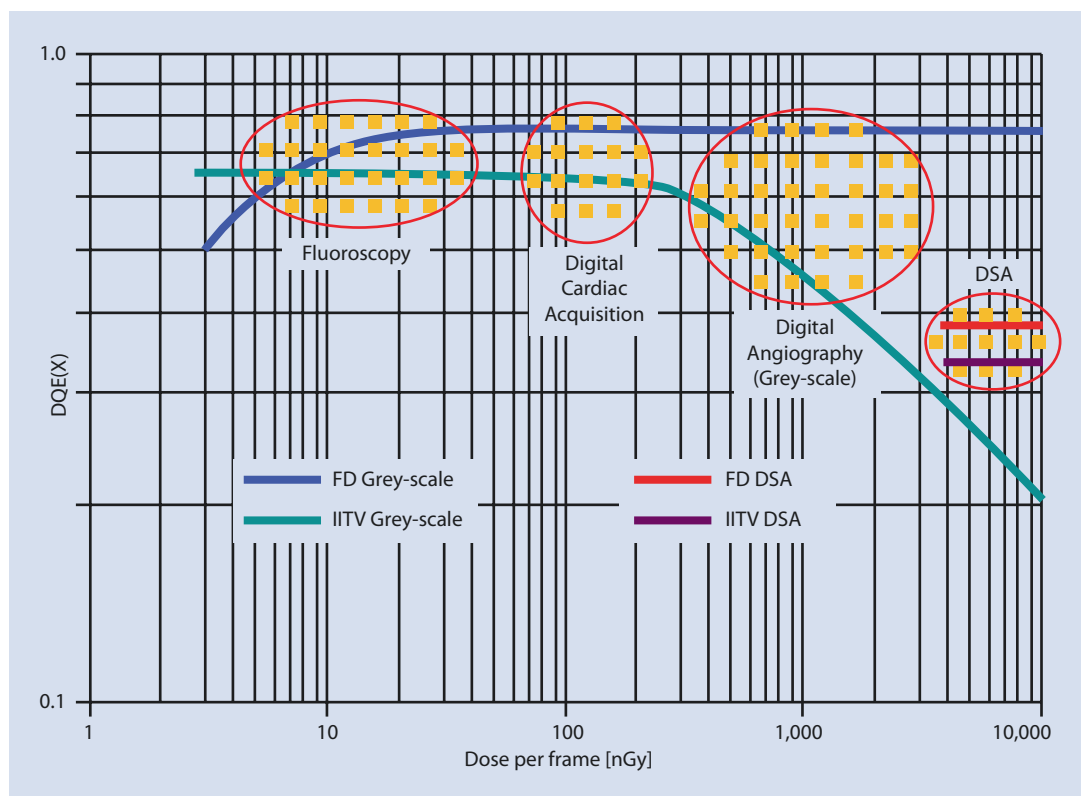




Fig. 11.19 Imaging performance of an indirect-conversion dynamic flat-panel detector (FD) compared with a digital image intensifier television (IITV) system:


variation of detective quantum efficiency (DQE) as a function of the detector entrance dose per frame in various imaging modalities



performance is typically 10–20% greater than that of a digital IITV-based digital fluoroscopy system [81, 82]. This finding would suggest that a modest (but *not* pronounced) improvement in image quality and/or saving in patient/staff dose should be expected when moving from digital IITV-based to dynamic FD-based fluoroscopy. This proposition has been supported by studies in cardio-angiography [83] and cardiac electrophysiology imaging [84]. However, other studies have reported increases in procedural dose with the FD detector [85–87], albeit that better image quality (spatial resolution) was also usually indicated. It is unclear from these studies to what extent the reported findings were dominated by differences in overall system design, calibration, and operator technique selection rather than the FD itself [88]. For example, it has been reported in the USA that when using FD-based cardiac systems, 90% reductions in dose are available for adult patients and 70–90% for pediatric patients by judicious selection of technique factors [89].

For modern indirect-conversion FDs in fluoroscopy, good DQE performance is maintained down to dose levels of less than 10 nGy per frame [57, 58, 60, 79]. At exceptionally low dose levels (say, well below 5 nGy per frame), a digital X-ray IITV system reportedly might offer better imaging performance; however, such a dose level would rarely be used in clinical practice. At higher dose levels (say, 1  $\mu$ Gy per frame and above), X-ray IITV systems exhibit a marked deterioration in DQE, and the superiority of the dynamic FD becomes clearly apparent. This deterioration in digital X-ray IITV system DQE results from the growing impact of the granular structure of the II input and output phosphor screens. This random structure acts as a fixed-pattern noise source, whose contribution becomes more pronounced as the X-ray quantum noise diminishes with increasing dose. The raw image data produced by an FD are subject to a number of (well-recognized) cosmetic imperfections. Therefore, FD systems incorporate automatic calibration and correction routines designed to remove these imperfections and therefore optimize detector response. These routines eliminate fixed-pattern noise in the FD plus other artifacts such as dark current offset, defective (and dead) lines and pixels in the AM array, and the memory effect (in some designs of system). (The overall image restoration process is identified as «RES» in  Fig. 11.8.)

In grayscale imaging, digital X-ray IITV systems do not benefit from the online correction of fixed-pattern noise, and hence, DQE is degraded at a high dose per frame. On the other hand, in DSA, fixed-pattern noise is eliminated (along with the patient background anatomy) by logarithmic subtraction. As such, for DSA applications, the DQE of the digital X-ray IITV at a high dose per frame is improved compared with that of the grayscale (nonsubtracted) images. However, following subtraction, the random noise fluctuations are more powerful than in an individual image frame, for reasons explained in  Sect. 11.6.3. Consequently, the DQE values produced during DSA for both dynamic FD and digital X-ray IITV are typically reduced by a factor of 2. However, at the dose levels used in DSA, the FD still exhibits superior DQE compared to the digital X-ray IITV system (albeit less markedly so than for the grayscale comparison). Over the dose range used in cardiovascular imaging, the FD exhibits a constant DQE, confirming that the indirect-conversion FD is a quantum-limited (and hence dose-efficient) image detector.

The set of graphs presented in  Fig. 11.19 implies that modern indirect-conversion FDs can comfortably support the full spectrum of clinical applications previously underwritten by digital X-ray IITV systems. Indeed, over the practical working dose range used in cardiovascular imaging, the FD is a more dose-efficient detector than the digital X-ray IITV. This becomes apparent when a dynamic FD is used to acquire X-ray projection data for 3D reconstruction imaging.

DQE is a powerful and versatile concept but can be augmented to take account of other image quality characteristics, such as unsharpness in space (blur) and temporal unsharpness (lag). This produces an even more comprehensive analysis of dynamic FD performance. However, such an analysis goes well beyond the scope of this chapter.

## 11.10 Digital Image Processing

---

Digital image processing has proved to be a powerful vector in the evolution of modern cardiovascular X-ray imaging equipment. Undoubtedly, continuing advances in digital image processing will be required to support the even more complex and exacting interventions that will emerge

in the future. Salient digital image-processing algorithms currently in use are reviewed in ► Sects. 11.10.1, 11.10.2, and 11.10.3.

### 11.10.1 Generic Image Enhancement

Generic digital image processing is needed to optimize the visual quality of the images presented to the clinician. Firstly, automatic digital restoration (identified as «RES» in ■ Fig. 11.8) is required to optimize the technical quality of the raw image data that are initially acquired. Such routines are embedded in dynamic FD-based imaging systems, as discussed in ► Sect. 11.9.6. Secondly, digital enhancement algorithms (identified as «ENH» in ■ Fig. 11.8) must then be applied to optimize the visual quality of the images finally presented on the display(s).

Standard image enhancement techniques include transformation of the image grayscale via a lookup table (LUT) in order to optimize the rendition of signals across the dynamic range. One familiar grayscale transformation is known as *white compression*, which is used to suppress signal highlights but amplify (stretch) signal contrast at indicative (normally lower) levels of mean signal [90]. This technique is particularly useful in cardiac grayscale imaging, where the heart is adjacent to the lungs, which exhibit regions of very high X-ray transmission. Application of a suitable LUT improves visibility of coronary structures while suppressing such highlights.

Digital image harmonization is another practical method of equalizing the display of signal contrast across the dynamic range. Here a heavily blurred (hence, unsharp) mask is created by convolving the input image with a large-area kernel. This operation averages the image data over large-area domains, producing a heavily blurred version of the original image. Subtraction of a fraction of this harmonization mask from the original image data removes large-area trends in the image that contain little (if any) relevant clinical information. This also equalizes the intensity of the image field, allowing a greater degree of contrast amplification to be applied to the images prior to display [91].

Digital contour enhancement is widely used to sharpen fine details, small structures, and edge discontinuities in the image. This has traditionally been achieved using the unsharp mask algorithm

[10, 91]. In this case, the original image is blurred not with a large-area kernel as used in image harmonization but with a small area kernel aimed at producing localized blurring. Subtraction of this unsharp mask image from the original image produces a contour map containing the fine-detail information. A weighted contribution of the contour image is then added back on to the original image, producing the contour-enhanced version of the original image. The form and degree of contour enhancement are controlled by the area of the unsharp mask and the weighting factor that is applied. The degrees of digital contrast and/or contour enhancement that can be applied to an image are ultimately limited by the noise fluctuations; these limitations are clearly apparent when processing low-dose fluoroscopy images.

The noise fluctuations visible during fluoroscopy can be reduced by temporal averaging of consecutive image frames. Each presented image frame may, for example, comprise the sum of the current frame with, say, the preceding  $\{N - 1\}$  frames in the fluoroscopic sequence. If the signal-to-noise ratio of an individual frame is given by  $\text{SNR}\{1\}$ , then the improvement in the signal-to-noise ratio resulting from time-averaging  $N$  frames, assuming 100% weighting for each frame ( $\text{SNR}\{N\}$ ) is described by:

$$\text{SNR}\{N\} = \text{SNR}\{1\} \cdot \sqrt{N}$$

In practice, temporal noise averaging is normally applied via a technique known as *recursive filtering*. This algorithm applies a weighted summation of the preceding frames; however, the recursive weighting factor progressively diminishes in magnitude for frames acquired earlier in the sequence. Recursive filtering acts like a computer-generated lag (temporal unsharpness), whose magnitude can be programmed. The recursion factor can be configured by the manufacturer's service engineer for each clinical application to achieve the desired degree of noise reduction. Inevitably, any target signal in the image that is moving—such as an opacified vessel, a guide wire, a catheter, or a stent—may however be blurred by generic recursive filtering. To be a clinically viable method, the recursive filter must be locally sensitive to the presence of target signal motion. Therefore, the algorithm must be primed to automatically reset the recursion factor to prevent signal blur, as circumstances demand.

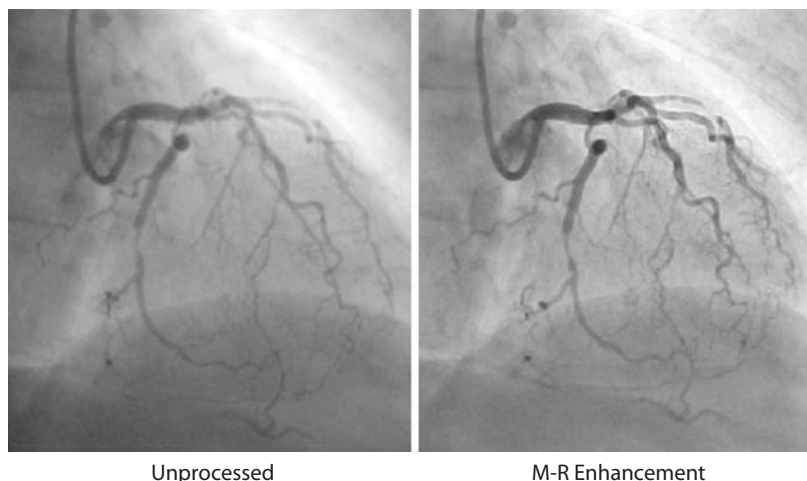
Multiresolution (M-R) processing of dynamic X-ray images is increasingly being used to optimize imaging performance in cardiovascular imaging [92, 93]. M-R processing is applied equally successfully in pulsed fluoroscopy and serial image acquisition. The M-R processing algorithm typically decomposes each image frame (in the sequence) into a set of sub-bands of differing spatial scale. These sub-bands encompass the range of scales from the finest details, through succeeding sizes, up to the coarsest structures. Each sub-band is processed independently using an intelligent filter design to separate (likely) vascular signals from random background noise at that scale. The algorithm adaptively processes each sub-band to enhance the identified signals but diminish the competing noise fluctuations. The processed sub-bands are then recomposed to produce the final enhanced image. ■ Figure 11.20 illustrates the improvement in image quality that is achievable with an M-R enhancement algorithm. The coronary angiogram on the left is subject to a grayscale optimization but is otherwise unprocessed. The image on the right is subject to spatial M-R enhancement; this image illustrates the improvement in the visualization of coronary vessels that is achievable. The M-R algorithm can also be adapted to take account of temporal (frame-to-frame) changes in image content. Temporal cues can then be used to improve the signal enhancement and noise suppression. In interventional fluoroscopy, the marked improvement in image quality attainable with M-R processing is often traded against a significant reduction in the patient dose.

### 11.10.2 Targeted Image Enhancement

Digital image processing can also be used to enhance the visualization of a specific target structure. Such algorithms are typically targeted at interventional devices such as stents, embolization coils, or atrial septal defect closure devices. Algorithms can also be targeted at the stenotic lesion itself. A commonly used implementation of targeted enhancement is designed to enhance the visibility of stents during coronary artery interventions [94, 95]. This algorithm, often referred to as *stent boost*, is briefly discussed here, as it represents a working example of targeted image processing.

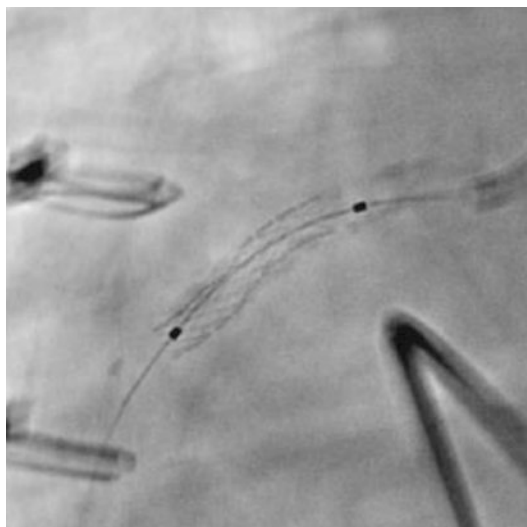
The optimum positioning and full expansion of a stent are important factors in ensuring the viability of a revascularization procedure. For example, mal-apposition and underexpansion of a stent are often associated with restenosis and late thrombosis. Correct deployment of the stent relies upon adequate visualization at each stage in the intervention. Coronary stents are often depicted with a low  $\Delta$ SNR due to the small diameter and low X-ray attenuation of the stent struts (typically only 100–50  $\mu\text{m}$  in size). In addition, the visibility of the stent may be compromised by the rapid movement of the host coronary vessel. This problem is compounded by the fact that cardiologists normally have to rely upon 2D projection images of what are often irregular 3D structures. Targeted digital image enhancement algorithms have therefore been developed to improve (boost) the visualization of the stent, independently of

■ **Fig. 11.20** Example of generic image enhancement: an unprocessed coronary artery acquisition image versus an image processed with the multiresolution (M-R) enhancement algorithm. (See «Acknowledgments»)



Unprocessed

M-R Enhancement



■ **Fig. 11.21** Example of targeted image enhancement: implementation of the stent boost algorithm, showing stent struts despite the presence of significant calcification. (See «Acknowledgments»)

cardiac and respiratory motion. This process requires the acquisition of a run of images of the deployed stent, lasting a few seconds. Images are typically acquired at rates of either 15 or preferably 30 frames  $s^{-1}$ . The processing software then automatically registers the position of the stent in succeeding image frames using translation, rotation, and stretching operations. The motion compensation is achieved by tracking the two radio-opaque markers on the (deflated) balloon, which remains in situ for reference. As a result, a registered set of images of the stent is generated, with the stent in a (quasi)-fixed position. Structures that are not synchronized with the balloon markers are consequently smeared out. The registered images are summed to improve the  $\Delta$ SNR and hence the visibility of the stent. ■ Figure 11.21 shows a typical implementation of stent boost in coronary angiography, which clearly shows stent struts despite the presence of significant calcification [96].

Results with the stent boost algorithm described above can be augmented by including a reference overlay of the vessel lumen in the image. This reference overlay can be derived from a contrast medium-filled image of the vessel, which is used as a subtraction mask [97]. All of the images needed for the process, including the contrast medium-filled vessels, can be acquired in the same acquisition run. The contrast medium is typically injected for the final couple of seconds

of the run. Following digital subtraction, the enhanced stent image is superimposed upon the contrast medium-filled vessel. Dynamic scrolling (or fading) between the enhanced stent image and the image of the opacified vessel lumen can be used to confirm the geometrical registration between the two and enables the cardiologist to more effectively evaluate the degree of stent engagement against the vessel wall. This algorithm has also been used to identify fractures in stents and gaps between adjacent stents [98].

In the future, the stent boost algorithm may be further improved by generating a 3D representation of the deployed stent. This can be achieved by acquiring a set of RA projection images of the stent and applying motion compensation to register these frames. A suitable cone-beam reconstruction algorithm can then be applied to the registered projection images to reconstruct a volumetric representation of the target stent [99].

### 11.10.3 Three-Dimensional Enhanced Imaging

The 1990s saw important developments in C-arm-based 3D reconstruction imaging using projection data acquired with a digital X-ray IITV system [100]. With such systems, extensive data processing was required to correct for cosmetic defects in the acquired data, before clinically acceptable images could be reconstructed. These defects included nonuniformities in the image field, variations in spatial resolution across the image field, and, above all, geometrical distortion. Significantly, the pattern of S-distortion varied with the projection angle due to the changing influence of the earth's magnetic field, as the image intensifier rotated around the patient [101]. For the reasons discussed in ► Sect. 11.9, dynamic FDs represent a much more uniform, stable, and distortion-free platform for implementing 3D X-ray imaging than the digital X-ray IITV system. As a result, the new FDs yield 3D reconstructions of high-contrast angiographic structures of greater spatial resolution [102, 103] and with fewer artifacts [104, 105]. Corrections may still however be needed for any mechanical flexing of the C-arm under gravity as it is rotated around the patient. 3D reconstruction imaging is now used to improve the visualization of complex networks of blood vessels, particularly in neurovascular



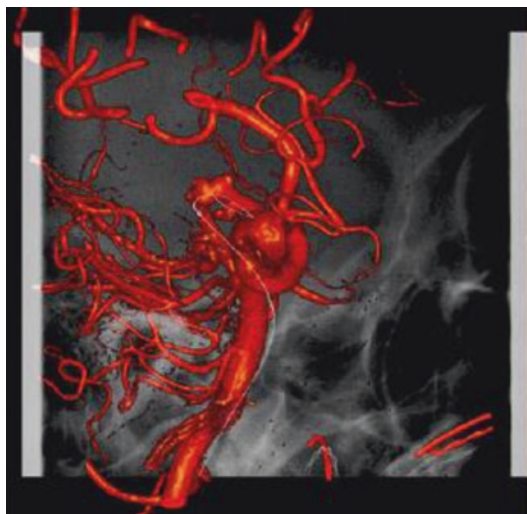
procedures [106]. Reportedly, this can ease some of the difficulties experienced in navigating a device through a web of tortuous vessels prior to the intervention. Use of 3D reconstructed images can reduce the duration of vascular procedures and contrast medium load [103, 107]. Patient radiation dose can be reduced significantly by replacing multiple DSA runs by a single rotational acquisition; this has been confirmed in a number of neurovascular dose surveys [108–110].

3D angiographic images reconstructed from data acquired using a dynamic FD mounted on a C-arm are now widely used in interventional cardiovascular imaging. In principle, C-arm cone-beam CT (CBCT) can exhibit superior spatial resolution to multislice CT. For an MSCT scanner, the spatial resolution (in high-resolution mode) can measure  $\sim 1.5$  lp  $\text{mm}^{-1}$ . At full pixel resolution, C-arm CBCT typically reaches a spatial resolution limit of 4 lp  $\text{mm}^{-1}$  (given a realistic degree of geometrical magnification). In practice, binned mode operation is normally used in 3D reconstructive imaging, either with  $[2 \times 2]$  or  $[4 \times 4]$  pixel binning. The corresponding spatial resolution limits in these modes typically reduce to 2 and 1 lp  $\text{mm}^{-1}$ , respectively. The dynamic range of an MSCT scanner can measure up to  $10^6:1$ . This value can be compared with  $10^4:1$  for an FD-based (direct-conversion type) CBCT system [107]. The large area of the FD ensures that in CBCT, a substantial volume of anatomy is covered in a single rotation of the C-arm. On the other hand, the wide-angle, open X-ray beam geometry that is used with CBCT makes the projection data much more susceptible to scattered X-rays than with MSCT scanner geometry. This limits the low-contrast performance of CBCT, as discussed in ► Sect. 11.6.4. The minimum contrast sensitivity of a modern MSCT scanner, expressed as the minimum detectable difference in Hounsfield units (HUs), typically measures  $\sim 2$ – $3$  HUs. Under laboratory conditions, the contrast sensitivity of FD-based CBCT reportedly measures 5 HUs [111]. In clinical practice, the contrast sensitivity will normally be poorer than this value (10 HUs or greater) [112–114]. Reportedly, the contrast sensitivity of CBCT is sufficient to visualize intracranial hemorrhage (albeit not with the precision achieved with an MSCT scanner) [115, 116].

Digital X-ray IITV systems lacked the dynamic range and  $\Delta\text{SNR}$  required to reliably reconstruct low-contrast soft-tissue structures

using CBCT. The improvement in technical performance afforded by the dynamic FD has made it possible to reconstruct high-quality 3D and (CT-like) 2D slice images of not only contrast medium-enhanced vasculature but also the surrounding brain [117]. Soft-tissue (low-contrast) CBCT reconstruction demands the acquisition of a set of projections with a finer angular interval than is required for high-contrast vascular imaging. This is essential to minimize artifacts in the reconstructed images due to angular under-sampling. Typically, the number of projections acquired has to be increased by a factor of 3–6 (or so) to achieve a 3D soft-tissue reconstruction of acceptable quality. As a result, soft-tissue scan times increase, typically to 20–25 s or so duration; this compares with the more usual 4–5 s used in high-contrast (angiographic) reconstructions [118]. In addition, the dose per projection may also be increased by a factor of  $\sim 2$ – $4\times$  to boost the SNR. The  $[4 \times 4]$  pixel binning mode is also often used in soft-tissue reconstructions to further reduce image noise. Interventionalists are finding that the immediacy, flexibility, and convenience of C-arm-based 3D reconstructive imaging in its various forms make it a valuable adjunct to standard 2D imaging. It must be noted however that soft-tissue CBCT comes with an overhead in the patient dose compared with high-contrast (angiographic) CBCT, potentially exceeding that used in MSCT [119].

To illustrate the high quality of C-arm-based CBCT images achievable with an FD, we will consider one specific 3D digital image-processing technique known as *dynamic 3D road mapping* [120, 121]. Standard-projection (2D) road mapping has been around for over 20 years and has proved to be a useful digital image-processing tool, particularly in neurovascular interventions [44, 122]. Here a grayscale (or possibly subtractive) image of the vascular region of interest is acquired and is then used as a road map for the live fluoroscopy image. The road map is used to aid navigation of guide wires, catheters, or other devices through irregular and tortuous sections of vessels. A major drawback of 2D road mapping however is that each time the interventionalist repositions the C-arm, as the procedure progresses, a new reference road map has to be acquired. The additional road maps take time to acquire and result in an increase in the contrast medium load and radiation dose to the patient (and staff).



■ Fig. 11.22 Example of dynamic three-dimensional road mapping in neurovascular imaging. (See «Acknowledgments»)

Dynamic 3D road mapping utilizes a 3D representation of the opacified vessels, again reconstructed from a set of RA projection images. The composite image presented to the clinician comprises the 3D road map of the relevant vasculature along with an overlay of live fluoroscopy. These two data sets are registered within a calibrated space; therefore, changes in the C-arm projection angle during ongoing fluoroscopy are automatically compensated for. This algorithm also automatically takes account of changes in geometrical magnification and detector FOV. An example of a dynamic 3D road map of cerebral vessels (plus a guide wire) along with the fluoroscopy overlay is shown in ■ Fig. 11.22. A 3D vascular reconstruction can also be merged with 2D sectional images through the brain—for example, to check for parenchyma bleeds. ■ Figure 11.23 shows a 3D reconstruction of the internal carotid and vertebral arteries merged with a CBCT sectional image through the brain. Again, the component data sets have been automatically registered and displayed as a visual composition [123]. It must be noted that dynamic 3D road mapping is not restricted to neurovascular applications, but also has roles in abdominal and hepatic interventional angiography. 3D imaging facilities can be integrated with automated tracking and navigation tools to further improve clinical functionality during interventional procedures [123].



■ Fig. 11.23 Three-dimensional vascular reconstruction registered with a slice image of the brain acquired with C-arm cone-beam computed tomography (CT). (See «Acknowledgments»)

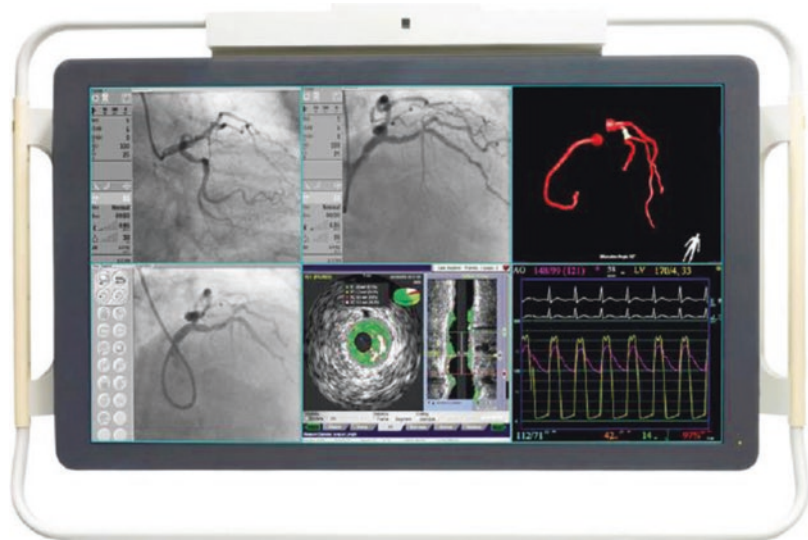
## 11.11 Flat-Screen Displays

Certain organic compounds are described as liquid crystals (LCs). An LC is a phase of matter that exhibits the (apparently) contradictory properties of being both a liquid and a (crystalline) solid at the same time. Significantly, the optical properties of a thin layer of an LC material can be altered in a systematic way by applying an electric field across it (via a bias voltage). Exploitation of this interesting physical phenomenon has led to the development of today's FS computer displays, domestic televisions, displays for games consoles and mobile phones, etc. FS displays have replaced traditional cathode ray tube (CRT) displays [124] in modern cardiovascular imaging and intervention facilities, as seen in ■ Fig. 11.16.

The FS displays used in modern digital fluoroscopy systems are based upon an LC layer combined with an active matrix array (AMA) [124]. The AMA typically comprises a 2D array of TFT elements, fabricated in a thin layer of amorphous silicon. Overall, the display screen has a multilayer construction incorporating an intense (fluorescent) backlight, front and rear polarizing filters, and a large-area (LC + AMA) optical modulator. Each pixel in the AMA can be addressed individually via an integrated superstructure of vertical and horizontal control lines. Application of a pattern of electrical voltage to the



■ **Fig. 11.24** Large-area (56") FlexVision color flat-screen (FS) display: typical multi-image composition seen in a cardiac interventional room. (See «Acknowledgments»)



AMA suitably modulates the light transmission of the LC layer. As a result, the device generates a pattern of light output, which forms the displayed image. Presentation of a time-varying sequence of image frames generates a dynamic display suitable for viewing fluoroscopy and other types of dynamic X-ray image.

Modern FS displays offer excellent spatial resolution, minimum contrast loss (veiling glare), and a wide dynamic range. The recommended maximum and minimum specification values of output luminance for diagnostic FS display devices are typically 500 and  $>170 \text{ cd m}^{-2}$ , respectively [125]. FS displays are electrically and thermally stable and, under normal circumstances, require minimal operator or service engineer adjustment. They are also much less bulky and more energy efficient than the CRT. The geometry and uniformity of FS displays are excellent and are immune to distortions and interference due to extraneous magnetic fields. Early designs of FS display could have a restricted angle of view; however, this is no longer seen as a major issue. Reportedly, some FS displays can exhibit a degree of lag (temporal unsharpness); in principle, however, this might benefit the display of fluoroscopic images, particularly those produced at low dose rates.

FS displays come with a variety of (diagonal) sizes, typically ranging from 18" to 22" for individual image displays. The equivalent pixel resolutions of these FS displays typically range from  $[1024 \times 1280]$  to  $[1200 \times 1600]$ , corresponding to 1.3- to 2-megapixel arrays, respectively. Rather

than relying upon multiple displays, a (very) large-screen FS display (56" in size) was recently introduced to provide the interventionalist with a more flexible viewing environment. This large-screen color display features a  $[2160 \times 3840]$  or 8.3-megapixel array. This so-called *FlexVision* display [126] enables clinical staff to compose, inspect, and evaluate images and data from multiple signal sources. ■ Figure 11.24 shows a typical FlexVision display composition seen in a cardiac interventional room. This display system also features a so-called *superzoom* facility, incorporating an advanced contour enhancement algorithm, which enables selected images to be enlarged by over a factor of 4. This facility is used to improve the visualization and interpretation of particularly complex, fine-detail cardiovascular structures.

## 11.12 Technique Considerations

Knowledge and understanding of X-ray coronary angiography and fluoroscopy equipment provide a base for the development of imaging concepts applicable to the clinical setting. Relevant technical concepts have been reviewed in ► Sects. 11.2, 11.3, 11.4, 11.5, 11.6, 11.7, 11.8, 11.9, 11.10, and 11.11. High image quality is always critical for adequate depiction of coronary morphology and consequently for accurate clinical interpretation. Inevitably, there are potential radiation hazards associated with achieving this aim. The operator-dependent technique factors that impact upon

image quality and radiation dose are now considered. Experience has been drawn from X-ray imaging in interventional coronary angiography (ICA); however, the principles carry over to many other cardiovascular applications.

### 11.12.1 Projections

First and foremost, ICA must provide accurate visualization of the target coronary anatomy. The target site must be fully visualized, and the target lesion must be optimally depicted throughout the entire course of the intervention. The target sites are imaged typically in two perpendicular projections free of crossing vessels. The reference images are stored on the display and updated as needed. Additional projections may be required to visualize coronary ostia, bifurcations, branching points, or other complex anatomical locations. Although steep angulations may be required to resolve ambiguities, a significant penalty in terms of radiation exposure should be taken into account (see also ► Chap. 15), limiting their use to absolute necessities [127].

### 11.12.2 Field of View and Magnification

The optimum FOV and image magnification are both important to keep track of the target site (large FOV, low or moderate magnification) and the target lesion (small FOV, high magnification). The FOV is defined by the image detector electronic zoom, the geometrical magnifications, and the shape of the X-ray beam, which is determined by the size of the collimation. Typical FOV sizes in ICA are 14 cm (smallest FOV, greatest magnification), 17 cm (medium FOV and magnification), and 23 cm (largest FOV, least magnification). To remove distracting structures from the image, the operator may further reduce the FOV by screening out the peripheral parts of the image by filters. Focusing on the relevant parts of the image allows the operator to concentrate fully on the site of action.

Besides the detector electronic zoom selection, the degree of magnification can, to an extent, be adjusted by the operator. The magnification factor, defined by the ratio of the

source-to-image-detector distance (SID) to the source-to-object distance (SOD), indicates the operator's options to adjust the geometrical magnification (see ► Sect. 11.4.5). In practice, however, SOD adjustability is limited by acceptable distance between the source and the patient's table, and patient skin dose considerations. SID is governed by mandating the distance between the flat-panel (image) detector and the patient (object) to reduce radiation exposure and image noise. The clinical usefulness of geometrical magnification is limited due to the skin dose increase with decreased SOD and increased SID (and the difference  $\Delta = \text{SID} - \text{SOD}$ ).

### 11.12.3 Zoom Mode and Detail Resolution

To improve visualization of the detail features of the target sites, the operator has the option to select an FD zoom mode, which increases the magnification of the image on the display. Depending on the equipment design, typically up to four different resolution modes are available in cardiac FDs and eight in (large-FOV) vascular FDs. However, due to the considerable increase in the radiation dose (by up to 100% or so) in high-resolution zoom modes, these should be used judiciously.

### 11.12.4 Spectral Filters and Wedge Filters

Diagnostic image quality can be further improved and the radiation exposure reduced by employing metal X-ray spectral beam filters and semi-transparent wedge filters to suppress peripheral highlights in the image. Copper spectral filters play a very important role in reducing patient skin dose in modern fluoroscopy. Wedge filters prevent image saturation effects, homogenizing the image field by increasing the X-ray absorbance of translucent regions (particularly the lungs) and hence increasing the dynamic range of the image. While performing interventional actions, strictly limiting the FOV to the target lesion appears to be a critical step in focusing the operator's cognitive resources onto the key features of the intervention.

### 11.12.5 Motion Artifacts and Positioning

Voluntary movements and repositioning of the patient during PCI should be avoided. Involuntary movements include the beating heart and breathing. Cardiac motion is complex, comprising rotational, concentric, and vertical components. Considering that in modern imaging systems, pulsed fluoroscopy is used with X-ray exposure pulse times of 10 ms or so, given the cycle times of the heart beat and respiration, image degradation due to involuntary motion is usually negligible. Therefore, breath holds, which potentially cause considerable discomfort to the patient, should be limited to selected sequences and mainly to remove the background of the diaphragm by deep inspiration. In some cases, repositioning of the patient on the table and altering the position of the shoulders or arms might be required to improve engagements of the guide at the ostia, particularly when internal mammary grafts are imaged or overlaps in extremely angulated projections must be avoided.

### 11.12.6 Recommended Approach

To keep the radiation exposure as low as reasonably achievable while assuring optimum image quality, the operator should be thoroughly familiar with the principles of efficient and professional coronary image acquisition, particularly the unavoidable trade-offs between image quality and radiation exposure. Principal recommendations for good radiological practice include the following:

- Select the *lowest ADRC dose rate* setting as appropriate.
- Keep the duration of fluoroscopy and cine acquisition runs to a minimum.
- If possible, use fluoroscopy instead of cine acquisition.
- When feasible, keep fluoroscopy and cine acquisition pulse rates as low as possible.
- Keep the distance between the patient and the image detector (FD or IITV) as short as possible.
- Use high geometrical magnification judiciously.
- Use high-resolution FD zoom mode selections sparingly.
- Use copper spectral filters and semitransparent wedge filters at all times (as appropriate).

- Keep angulations of projections as flat as possible; use steep angulations only when justified.
- When feasible (e.g., for pediatric studies), remove the antiscatter grid.
- When available, use digital storage and processing facilities such as last image hold, fluoroscopy store, virtual collimation, and road mapping (in its various forms) to minimize X-ray beam-on time.

Use of these recommendations is consistent with the ALARA principle and is critical to both radiation protection and optimum image quality.

### 11.12.7 Case Documentation

To allow reproducible case analysis, standards of case documentation are recommended. The suggested standard for basic documentation of PCI procedures includes acquisition of the following short digital image sequences with two optimum perpendicular projections, viz.:

- **Baseline**
  - Full view of the target site (large FOV, low resolution)
  - Focused view of the target lesion (small FOV, high resolution)
- **Main interventional cycle**
  - Full views and focused views as needed, following each relevant interventional action
- **Last interventional cycle**
  - Full view of the target site with a guide wire in place (large FOV, low resolution)
  - Focused view of the target lesion with a guide wire in place (small FOV, high resolution)
- **Termination**
  - Full view of the target site with all instrumentation removed (large FOV, low resolution)
  - Full view of the target site (large FOV, low resolution)
  - Focused view of the target lesion with all instrumentation removed (small FOV, high resolution)

Standardized documentation allows development of a library of teaching cases and aids systematic case analysis.

### 11.12.8 Contrast Media

The degree and homogeneity of opacification of the coronary artery lumen are critical for both clinical interpretation and quantitative coronary image analysis. The magnitude of the resulting contrast enhancement is determined by the rate of iodine delivery into the vascular system, which in turn is governed by the concentration of iodine in the contrast medium, the rate of injection, and the injection volume. Optimum contrast medium injection allows homogenous luminal opacification and sharp definition of the endo-luminal interface. Intraluminal objects and obstructions such as thrombi and intimal flaps, and intramural processes such as myointimal dissections and turbulent blood flow, should be also visualized. The amount and rate of contrast medium injection in coronary arteries depends upon the size of the vascular bed and coronary flow rates; typically, 4–8 ml contrast media at a rate of 4 ml s<sup>-1</sup> is administered per manual injection.

At a given rate of delivery, attenuation of the X-ray beam depends upon the attenuation characteristics and the concentration of iodine concentration in the vessel. Optimum contrast is achieved at photon energies just above 33.2 keV because of the sharp increase in X-ray absorption of iodine at that energy compared with the surrounding tissues (due the K-absorption edge of iodine). With increasing X-ray energy, the attenuation due to iodine decreases more rapidly compared with the surrounding soft tissues, which results in lower vessel contrast.

There are basically four different types of vascular iodine contrast media, all with the basic structure of a benzene ring with symmetrically coupled iodine atoms. Vascular iodine contrast media differ in important properties, including:

*Water solubility*, which determines the maximum concentration of iodine that can be achieved and, therefore, the maximum X-ray absorption, which generates coronary artery subject contrast

*Osmolality*, i.e., the osmotic pressure of the solution, determining the magnitude of water shifts between vascular and extravascular spaces

*Viscosity*, which determines the force required for intracoronary injections (warming the contrast media to 37 °C before administration sharply reduces viscosity)

*Chemotoxicity*, determined by hydro- and lipophilicity, protein binding, electrical charge,

and histamine release—factors responsible for biological incompatibility and adverse effects

Dimeric ionic and nonionic contrast media contain ~320 mg iodine ml<sup>-1</sup>, and monomeric nonionic ones contain ~370–400 mg iodine ml<sup>-1</sup>. In terms of osmolality, high- and low-osmolality contrast media (HOCMs and LOCMs) can be distinguished: HOCMs have ~1.500 mOsmol l<sup>-1</sup> and LOCMs typically have ~500–800 mOsmol l<sup>-1</sup>. *Isotonicity*—i.e., osmolality of human plasma (290 mOsmol l<sup>-1</sup>)—has been nearly achieved (~300 mOsmol l<sup>-1</sup>) in some nonionic dimeric contrast media—for example, iotrolan and iodixanol. Vascular contrast media are generally safe, and severe responses (such as hypotensive shock, laryngeal edema, or cardiac arrest) are exceedingly rare (~<0.1%). Because of their better tolerance, nonionic LOCMs are preferably used in PCI. Despite voluminous literature on the differential effects of modern contrast agents, no clear advantages of individual agents in terms of their efficacy and safety profiles have been unequivocally proven. Although low-viscosity and low-osmolality contrast media at a comparable iodine concentration might appear preferable, in practice the selection of a specific contrast agent remains in the majority of cases at the discretion of the operator. The total volume of contrast medium required for coronary artery intervention varies, averaging about 80–100 ml (approximate range 40–500 ml). To avoid adverse effects, contrast media should be used judiciously, and the total volume must be kept to a minimum.

**Acknowledgments** ▶ Section 11.12 of this chapter, titled «Technique Considerations,» was written by Peter Lanzer, MD, Health Care Center, Bitterfeld-Wolfen, Germany.

The author gratefully acknowledges many helpful discussions during the preparation of this chapter with his colleagues Amber Gislason and Andrew Davies (at the University of Leeds) and Professor Mohan Sivanathan (of the Yorkshire Heart Centre, LGI Leeds).

Amber Gislason kindly provided the X-ray spectra shown in ■ Figs. 11.1 and 11.13. Mr. Davies and Professor Sivanathan kindly provided the images used in ■ Figs. 11.20 and 11.21. The images used in ■ Figs. 11.11, 11.15, 11.16, 11.18, 11.22, 11.23, and 11.24 are reproduced courtesy of Dr. Eric A. von Reth, senior director of Clinical Sciences at Philips Healthcare (Best, the Netherlands).



## References

- Bushberg JT, Siebert JA, Boone JM, Leidholdt EM. The essential physics of medical imaging. 2nd ed. Williams & Wilkins, Philadelphia: Lippincott; 2002.
- Dowsett DJ, Kenny PA, Johnston RE. The physics of diagnostic imaging. 2nd ed. London: Hodder Arnold; 2006.
- Momose A, Takeda T, Itai Y. Blood vessels: depiction at phase contrast X-ray imaging with contrast agents in the mouse and rat—feasibility study. *Radiology*. 2000;217:593–6.
- Partridge MJ, McGahan G, Causton S, Bowers M, Mason M, Dalby M, Mitchell A. Radiation dose reduction without compromise of image quality in cardiac angiography and intervention with the use of a flat panel detector without an antiscatter grid. *Heart*. 2006;92:507–10.
- Boone JM, Seibert JA. A figure of merit comparison between bremsstrahlung and monoenergetic X-ray sources for angiography. *J Xray Sci Technol*. 1994;4:334–45.
- Gislason AJ, Davies AG, Cowen AR. Dose optimization in paediatric cardiac X-ray imaging. *Med Phys*. 2010;37(10):5258–69.
- Lin PJ. Technical advances of interventional and flat panel image receptor. *Health Phys*. 2008;95(5):650–7.
- Seibert JA. Flat-panel detectors: how much better are they? *Pediatr Radiol*. 2006;36(Suppl 2):173–81.
- Holmes DR, Laskey WK, Wondrow MA, Cusma JT. Flat-panel detectors in the cardiac catheterization laboratory: revolution or evolution—what are the issues? *Catheter Cardiovasc Interv*. 2004;63:324–30.
- Balter S. *Interventional fluoroscopy: physics, technology and safety*. New York: Wiley-Liss; 2001.
- Mistretta CA, Crummy AB. Diagnosis of cardiovascular disease by digital subtraction angiography. *Science*. 1981;214:761–5.
- Mistretta CA, Kruger RA, Ergun DL, Shaw CG, Crummy AB, Strother CM, Sackett JF, Myerowitz PD, Turnipseed WD, Zarnstorff WC, van Lysel MS, Lancaster JC, Ruzicka FF. Digital vascular imaging. *Medicamundi*. 1981;26(1):1–10.
- Ludwig JW, Verhoeven LHJ, Engels PHC. Digital video subtraction angiography (DVSA) equipment: angiographic technique in comparison with conventional angiography in different in different vascular areas. *Br J Radiol*. 1982;55:545–53.
- Verhoeven LAJ. DSA imaging: some physical and technical aspects. *Medicamundi*. 1985;30:46–55.
- Brody WR. Hybrid subtraction for improved arteriography. *Radiology*. 1981;141:828–31.
- Hoff DJ, Wallace MC, ter Brugge KG, Gentili F. Rotational angiography assessment of cerebral aneurysms. *AJNR Am J Neuroradiol*. 1994;15(10):1945–8.
- Tu RT, Cohen WA, Maravilla KR, Bush WH, Patel NH, Eskridge J, Winn HR. Digital subtraction rotational angiography for aneurysms of the intracranial anterior circulation: injection method and optimization. *AJNR Am J Neuroradiol*. 1996;17:1127–36.
- Seymour HR, Matson MB, Belli A-M, Morgan R, Kyriou J, Patel U. Rotational digital subtraction angiography of the renal arteries: technique and evaluation in the study of native and transplant renal arteries. *Br J Radiol*. 2001;74:134–41.
- Maddux JT, Wink O, Messenger JC, Groves BM, Liao R, Strzelczyk J, Chen S-YJ, Carroll JD. Randomized study of the safety and clinical utility of rotational angiography versus standard angiography in the diagnosis of coronary artery disease. *Catheter Cardiovasc Interv*. 2004;62:167–74.
- Raman SV, Morford R, Neff M, Attar TT, Kukielka G, Magorien RD, Bush CA. Rotational X-ray coronary angiography. *Catheter Cardiovasc Interv*. 2004;63:201–7.
- Akhtar M, Vakharia KT, Mishell J, Gera A, Ports TA, Yeghiazarians Y, Michaels AD. Randomized study of the safety and clinical utility of rotational vs standard coronary angiography using a flat-panel detector. *Catheter Cardiovasc Interv*. 2005;66:43–9.
- Moret J, Kemkers R, Op de Beek J, Koppe R, Klotz E, Grass M. 2D rotational angiography: clinical value in endovascular treatment. *Medicamundi*. 1998;42(3):8–14.
- Hochmuth A, Spetzger U, Schumacher M. Comparison of three dimensional rotational angiography with digital subtraction angiography in the assessment of ruptured cerebral aneurysms. *AJNR Am J Neuroradiol*. 2002;23:1199–205.
- Feldkamp LA, Davis LC, Kress JW. Practical cone beam algorithm. *J Opt Soc Am*. 1984;1(6):612–9.
- Scott D, Davies AG, Cowen AR, Workman A. Technique for 3D reconstruction of arteries from angiographic projections. In: Lemke HU, Inamura K, Jaffe CC, Felix R, editors. *Proceedings computer assisted radiology*. Berlin: Springer; 1993. p. 541–6.
- Grass M, Koppe R, Klotz PR, Kuhn MH, Aerts H, Op de Beek J, Kemkers R. Three-dimensional reconstruction of high contrast objects using C-arm image intensifier projection data. *Comput Med Imaging Graph*. 1999;23:311–21.
- Siewerdsen JH, Jaffrey DA. Cone-beam computed tomography with a flat-panel imager: magnitude and effects of scatter. *Med Phys*. 2004;28:22–3.
- Muijderman EA, Roelandse CD, Vetter A, Schreiber P. A diagnostic X-ray tube with spiral-groove bearings. *Philips Tech Rev*. 1989;44(11/12):357–63.
- Schmidt T, Behling R. MRC: a successful platform for future X-ray tube development. *Medicamundi*. 2000;44(2):50–5.
- Hahn H, Farber D, Allmendinger H, Brendler J. Grid-controlled fluoroscopy in pediatric radiology. *Medicamundi*. 1997;41(1):12–7.
- Hernandez RJ, Goodsitt MM. Reduction of radiation dose in pediatric patients using pulsed fluoroscopy. *Am J Roentgenol*. 1996;167(5):1247–53.
- Sobol WT. High frequency X-ray generator basics. *Med Phys*. 2002;29(2):132–44.
- Den Boer AD, de Feyter PJ, Hummel WA, Keane D, Roelandt JRTC. Reduction of radiation exposure while maintaining high-quality fluoroscopic images during interventional cardiology using novel X-ray tube technology extra beam filtering. *Circulation*. 1994;89:2710–4.
- Gagne RM, Quinn PW. X-ray spectral considerations in fluoroscopy. In: Balter S, Shope TB, editors. *RSNA*

- categorical course in physics. Oak Brook: RSNA; 1995. p. 49–58.
35. Baldazzi G, Corazza I, Rossi PL, Testoni G, Bernardi T, Zannoli R. In vivo effectiveness of gadolinium filter for paediatric cardiac angiography in terms of image quality and radiation exposure. *Phys Med*. 2002;28:109–13.
  36. Rossi PL, Mariselli M, Corazza I, Bianchini D, Biffi M, Martignani C, Zannoli R, Boriani G. Decrease in patient radiation exposure by a tantalum filter during electrophysiological procedures. *Pacing Clin Electrophysiol*. 2009;32(Suppl 1):S109–12.
  37. Geise RA. Fluoroscopy: recording of fluoroscopic images and automatic exposure control. *Radiographics*. 2001;21:227–36.
  38. Lin PP. The operation logic of automatic dose control of fluoroscopy system in conjunction with spectral filters. *Med Phys*. 2007;34:3169–72.
  39. Krohmer JS. Radiography and fluoroscopy, 1920 to the present. *Radiographics*. 1989;9:1129–53.
  40. Schueler BA. General overview of fluoroscopic imaging. *Radiographics*. 2000;20:1115–26.
  41. Wang J, Blackburn TJ. X-ray image intensifiers for fluoroscopy. *Radiographics*. 2000;20:1471–7.
  42. Van Lysel MS. Fluoroscopy: optical coupling and the video system. *Radiographics*. 2000;20:1769–86.
  43. Snoeren RM, ten Caat RB, Dillen BGM, Gieles P, van der Veen JCT. Solid state image sensor in X-ray television. *Medicamundi*. 1991;36:203–11.
  44. Pooley RA, McKinney JM, Miller DA. Digital fluoroscopy. *Radiographics*. 2001;21:521–34.
  45. Neitzel U. Recent technological developments and their influence. *Radiat Prot Dosim*. 2000;90(1–2):15–20.
  46. Powell A, Katzen B. First experiences with a CCD system in interventional radiology: the Integris V5000. *Medicamundi*. 1999;43(4):38–44.
  47. Cowen AR, Kengyelics SM, Davies AG. Solid-state flat-panel digital radiography detectors and their physical imaging characteristics. *Clin Radiol*. 2008;63:487–98.
  48. Schiebel U, Conrads N, Jung N, Weibrecht M, Wiczorek H, Zaengel T. Fluoroscopic X-ray imaging with amorphous silicon thin-film arrays. *SPIE Proc Phys Med Imaging*. 1994;2162:129–40.
  49. Antonuk LE, Yorkston J, Huang W, Siewerdsen JH, Boudry JM, El-Mohri Y. A real-time, flat-panel amorphous silicon digital X-ray imager. *Radiographics*. 1995;15:993–1000.
  50. Chabbal J, Chaussat T, Ducourant T, Fritsch L, Michailos J, Spinnler V, Vieux G, Arques M, Hahm G, Hoheisel M, Horbaschek H, Schulz RF, Spahn MF. Amorphous silicon X-ray image sensor. *SPIE Proc Phys Med Imaging*. 1996;2708:499–510.
  51. Colbeth RE, Allen MJ, Day DJ, Gilblom DL, Klaus Meijer-Brown ME, Pavkovich J, Seppi EJ, Shapiro EG. Characterisation of an amorphous silicon fluoroscopic imager. *SPIE Proc Phys Med Imaging*. 1997;3032:42–51.
  52. Colbeth RE, Allen MJ, Day DJ, Gilblom DL, Harris R, Job ID, Klausmeier-Brown ME, Pavkovich JM, Seppi EJ, Shapiro EG, Wright MD, Yu J. Flat panel imaging system for fluoroscopy applications. *SPIE Proc Phys Med Imaging*. 1998;3336:376–87.
  53. Bruijns TJ, Alving PL, Baker EL, Bury RF, Cowen AR, Jung N, Luijendijk HA, Meulenbrugge HJ, Stouten HJ. Technical and clinical results of an experimental flat dynamic (digital) X-ray image detector (FDXD) systems with real-time correction. *SPIE Proc Phys Med Imaging*. 1998;3336:33–44.
  54. Bury RF, Cowen AR, Davies AG, Baker EL, Hawkrigde P, Bruijns AJC, Reitsma H. Technical report: initial experiences with an experimental solid-state universal digital X-ray detector. *Clin Radiol*. 1998;53:923–8.
  55. Bruijns AJC, Bury R, Busse F, Davies AG, Cowen AR, Rutten W, Reitsma H. Technical and clinical assessments of an experimental flat dynamic X-ray image detector system. *SPIE Proc Phys Med Imaging*. 1999;3659:324–35.
  56. Jung N, Alving PL, Busse F, Conrads N, Meulenbrugge HM, Rutten W, Schiebel UW, Weibrecht M, Wiczorek HK. Dynamic X-ray imaging based on an amorphous silicon thin-film array. *SPIE Proc Phys Med Imaging*. 1998;3336:974–85.
  57. Busse F, Rutten W, Sandkamp B, Alving PL, Bastiaens RJM, Ducourant T. Design and performance of a high quality cardiac flat panel detector. *SPIE Proc Phys Med Imaging*. 2002;4682:819–27.
  58. Granfors PR, Aufrichtig R, Netel H, Brunst G, Boudry JM, Luo D, Albagli D, Tkaczyk JE. Performance of a flat cardiac detector. *SPIE Proc Phys Med Imaging*. 2001;4320:77–86.
  59. Sivananthan UM, Moore J, Cowan JC, Pepper CB, Hunter S, Cowen AR, Davies AG, Kengyelics SM. A flat-detector cardiac cath lab system in clinical practice. *Medicamundi*. 2004;48:4–12.
  60. Granfors PR, Aufrichtig R, Possin GE, Giambattista BW, Huang ZS, Liu J, Ma B. Performance of a 41 × 41 cm<sup>2</sup> amorphous silicon flat panel X-ray detector designed for angiographic and R&F imaging applications. *Med Phys*. 2003;30:2715–26.
  61. Ducourant T, Couder D, Wirth T, Trochet JC, Bastiaens R, Bruijns T, Luijendijk HA, Sandkamp B, Davies AG, Didier D, Gonzalez A, Terraz S, Ruefenacht D, et al. Image quality of digital subtraction angiography using flat detector technology. *SPIE Proc Phys Med Imaging*. 2003;5030:203–14.
  62. Bruijns AJC, Bastiaens R, Hoornaert B, von Reth E, Busse F, Heer VK, Ducourant T, Cowen AR, Davies AG, Terrier F. Image quality of a large-area dynamic flat detector: comparison with a state-of-the-art IITV system. *SPIE Proc Phys Med Imaging*. 2002;4682:332–43.
  63. Colbeth RE, Boyce S, Fong R, Gray K, Harris R, Job ID, Mollov IP, Nepo B, Pakovich JM, Taie-Nobarie N, Seppi EJ, Shapiro EG, Wright MD, Webb C, Yu JM. 40 × 30 cm<sup>2</sup> flat imager for angiography, R&F and cone-beam CT applications. *SPIE Proc Phys Med Imaging*. 2001;4320:94–102.
  64. Choquette M, Demers Y, Shukri Z, Tousignant O, Aoki K, Honda M, Takahashi A, Tsukamoto A. Real time performance of a selenium based detector for fluoroscopy. *SPIE Proc Phys Med Imaging*. 2001;4320:501–8.
  65. Tousignant O, Demers Y, Laperriere L, Nishiki M, Nagai S, Tomisaki T, Takahashi A, Aoki K. Clinical performances of a 14" × 14" real time amorphous selenium flat panel detector. *SPIE Proc Phys Med Imaging*. 2003;5030:71–6.
  66. Asahina H. Selenium-based flat panel X-ray detector for digital fluoroscopy and radiography. *Toshiba Med Rev*. 1999;69:1–7.



67. Tousignant O, Demers Y, Lapierre L, Marcovici S. (2007). A-Se flat panel detectors for medical applications. Sensors applications symposium IEEE, San Diego, California USA.
68. Spahn M. Flat detectors and their clinical applications. *Eur Radiol.* 2005;15:1934–47.
69. Nikoloff EL. Survey of modern fluoroscopy imaging: flat-panel detectors versus image intensifiers and more. *Radiographics.* 2011;31:591–602.
70. Roos PG, Colbeth RE, Mollov I, Munro P, Pavkovich J, Seppi EJ, Shapiro EG, Tognina CA, Virshup GF, Yu M, Zentai G, Kaissi W, Matsinos A, Richters J, Riehm H. Multiple-gain-ranging readout method to extend the dynamic range of amorphous silicon flat-panel imagers. *SPIE Proc Phys Med Imaging.* 2004;5368:139–49.
71. Boyce SJ, Chawla A, Samei E. Physical evaluation of a high frame rate, extended dynamic range flat panel detector for real-time cone beam computed tomography applications. *SPIE Proc Phys Med Imaging.* 2005;5745:591–9.
72. Fahrhig R, Wen Z, Ganguly A, DeCrescenzo G, Rowlands JA, Stevens GM, Saunders RF, Pelc NJ. Performance of a static-anode/flat-panel X-ray fluoroscopy system in a diagnostic strength magnetic field: truly hybrid X-ray/MR imaging system. *Med Phys.* 2005;32:1775–84.
73. Achenbach S, Ropers D, Holle J, Muschol G, Daniel WG, Moshage W. In-plane coronary arterial motion velocity: measurement with electron-beam CT. *Radiology.* 2000;216:457–63.
74. Zhao W, DeCrescenzo G, Rowlands JA. Investigation of lag and ghosting in amorphous selenium flat-panel X-ray detectors. *SPIE Proc Phys Med Imaging.* 2003;4682:9–20.
75. Siewerdsen JH, Jaffray DA. A ghost story: spatio-temporal response characteristics of an indirect-detection flat-panel imager. *Med Phys.* 1999;26:1624–41.
76. Overdick M, Solf T, Wischmann H-A. Temporal artefacts in flat dynamic X-ray detectors. *SPIE Proc Phys Med Imaging.* 2001;4320:47–58.
77. Ducourant T, Michel M, Vieux G, Peppler T, Trochet JC, Schulz RF, Bastiaens RJM, Busse F. Optimization of key building blocks for a large area radiographic and fluoroscopic dynamic X-ray detector based on a-Si:H/CsI:TI flat panel technology. *SPIE Proc Phys Med Imaging.* 2000;3977:14–25.
78. Dainty JC, Shaw R. *Image science.* London: Academic Press; 1975.
79. Tognina CA, Mollov I, Yu JM, Webb C, Roos PG, Batts M, Trinh D, Fong R, Taie-Nobriae N, Nepo B, Job IS, Gray K, Boyce S, Colbeth RE. Design and performance of a new a-Si flat panel imager for use in cardiovascular and mobile C-arm imaging systems. *SPIE Proc Phys Med Imaging.* 2004;5368:648–56.
80. Davies AG, Cowen AR, Kengyelics SM, Bury RF, Bruijns TJ. Threshold contrast detail detectability measurement of the fluoroscopic image quality of a dynamic solid-state digital X-ray image detector. *Med Phys.* 2001;28:11–5.
81. Spekowius G, Boerner H, Eckenbach W, Quadflieg P, Laurensen GJ. Simulation of the imaging performance of X-ray image intensifier TV camera chains. *SPIE Proc Phys Med Imaging.* 1995;2432:12–23.
82. Baker EL, Cowen AR, Kemner R, Bastiaens R. A physical evaluation of a CCD-based X-ray II fluorography system for cardiac applications. *SPIE Proc Phys Med Imaging.* 1998;3336:430–41.
83. Vano E, Geiger B, Schreiner A, Back C, Beissel J. Dynamic flat panel detector versus image intensifier in cardiac: dose and image quality. *Phys Med Biol.* 2005;50:5731–42.
84. Davies AG, Cowen AR, Kengyelics SM, Moore J, Pepper C, Cowen C, Sivananthan UM. X-ray dose reduction in fluoroscopically guided electrophysiology procedures. *Pacing Clin Electrophysiol.* 2006;29:262–71.
85. Prasan AM, Ison G, Rees DM. Radiation exposure during elective coronary angioplasty: the effect of flat-panel detection. *Heart Lung Circ.* 2008;17:215–9.
86. Trianni A, Bernardi G, Padovani R. Are new technologies always reducing patient doses in cardiac procedures. *Radiat Prot Dosim.* 2005;117:97–101.
87. Tsapaki V, Kottou S, Kollaros N, Dafnomili P, Kyriakidis Z, Neofotistou V. Dose performance evaluation of charge coupled device and a flat-panel digital fluoroscopy system recently installed in an interventional cardiology laboratory. *Radiat Prot Dosim.* 2004;111(3):297–304.
88. Davies AG, Cowen AR, Kengyelics SM, Moore J, Sivananthan MU. Do flat detector cardiac X-ray systems convey advantages over image intensifier-based systems? Study comparing X-ray dose and image quality. *Eur Radiol.* 2007;17:1787–94.
89. Nikoloff EL, Lu ZF, Dutta A, So J, Balter S, Moses J. Influence of flat-panel fluoroscopic equipment variables on cardiac radiation doses. *Cardiovasc Intervent Radiol.* 2007;30:169–76.
90. Cowen AR. Image processing in digital radiography. *Imaging.* 1994;6:77–99.
91. Cowen AR, Hartley PJ, Workman A. The computer enhancement of digital grey-scale fluorography images. *Br J Radiol.* 1988;61(726):492–500.
92. Aach T, Mayntz C, Rongen P, Schmitz G, Stegehuis H. Spatiotemporal multiscale vessel enhancement for coronary angiograms. *SPIE Proc Phys Med Imaging.* 2002;4684:1010–21.
93. Wu Z, Fang M, Qian J, Schramm H. A multi-scale adaptive method for blood vessel enhancement in X-ray angiography. *SPIE Proc Phys Med Imaging.* 1997;3036:326–35.
94. Koolen JJ, Van Het Veer M, Hanekamp CEE. Stentboost image enhancement: first clinical experience. *Medicamundi.* 2005;49(2):4–8.
95. Mishell JM, Vakharia KT, Ports TA, Yeghiazians Y, Michaels AD. Determination of adequate coronary stent expansion using stentboost, a novel fluoroscopic image processing technique. *Catheter Cardiovasc Interv.* 2007;69:84–93.
96. Sivananthan UM, Blackburn M, Cowan JC, Mclenachan J, Pepper CB, Hunter S, Moore J, Cowen AR, Davies AG, Kengyelics SM. Cardiac cath lab upgrade improves efficiency and reduces dose. *Medicamundi.* 2006; 50(2):1–9.
97. Agostini P, Verheye S. Bifurcation stenting with dedicated biolimus-eluting stent: X-ray visual enhancement of the angiographic result with “StentBoost”. *Catheter Cardiovasc Interv.* 2007;70:233–6.

98. Eng MH, Klein AP, Wink O, Hansgen A, Carroll JD, Garcia JA. Enhanced stent visualization: a case series demonstrating practical applications during PCI. *Int J Cardiol.* 2010;141(1):e8–e16.
99. Schoonenberg G, Florent R. Advanced visibility enhancement for stents and other devices: image processing aspects. *Cardiol Clin.* 2009;27:477–90.
100. Fahrig R, Fox AJ, Lownie S, Holdsworth DW. Use of a C-arm system to generate true three-dimensional computed rotational angiograms: preliminary in vitro and in vivo results. *AJNR Am J Neuroradiol.* 1997;18:1507–14.
101. Fahrig R, Moreau M, Holdsworth DW. Three dimensional computed tomographic reconstruction using C-arm mounted XRRI: correction of image intensifier distortion. *Med Phys.* 1997;24:1097–106.
102. Baba R, Konno Y, Ueda K, Ikeda S. Comparison of flat-panel detector and image intensifier detector for cone-beam CT. *Comput Med Imaging Graph.* 2002;6:153–8.
103. Hirota S, Nakao N, Yamamoto S, Kobayashi K, Maeda H, Ishikura R, Miura K, Sakamoto K, Ueda K, Baba R. Cone-beam CT with flat-panel detector digital angiography system: early experiences in abdominal interventional procedures. *Cardiovasc Intervent Radiol.* 2006;29:1034–8.
104. Hirai T, Korogi Y, Ono K, Yamura M, Uemura S, Yamashita Y. Pseudostenosis phenomenon at volume-rendered three-dimensional digital angiography of intracranial arteries: frequency, location and effect on image evaluation. *Radiology.* 2004;232:882–7.
105. Kakeda S, Korogi Y, Ohnari N, Hatakeyama Y, Moriya J, Oda N, Nishino K, Miyamoto W. 3D digital subtraction angiography of intracranial aneurysms: comparison of flat panel detector with conventional IITV system using a vascular phantom. *AJNR Am J Neuroradiol.* 2007;28:839–43.
106. Sugahara T, Korogi Y, Nakashima K, Hamatake S, Honda S, Takahashi M. Comparison of 2D and 3D digital subtraction angiography in evaluation of intracranial aneurysms. *AJNR Am J Neuroradiol.* 2002;23:1545–52.
107. Hatakeyama Y, Kakeda S, Korogi Y, Ohnari N, Moriya J, Oda N, Nishino K, Miyamoto W. Intracranial 2D and 3D DSA with flat panel detector of the direct conversion type: initial experience. *Eur Radiol.* 2006;16:2594–602.
108. Schueler BA, Kallmes DF, Cloft HJ. 3D cerebral angiography: radiation dose comparison with digital subtraction angiography. *AJNR Am J Neuroradiol.* 2005;26:1898–901.
109. Bridcutt RR, Murphy E, Workman A, Flynn P, Winder RJ. Patient dose from 3D rotational neurovascular studies. *Br J Radiol.* 2007;80:362–6.
110. Tsapaki V, Vano E, Mavrikou I, Neofotistou V, Gallego JJ, Fernandez JM, Santos E, Mendez J. Comparison of patient dose in two-dimensional carotid arteriography and three-dimensional rotational angiography. *Cardiovasc Intervent Radiol.* 2008;31:477–82.
111. Gupta R, Cheung AC, Bartling SH, Lissauskas J, Grasruck M, Leidecker C, Schmidt B, Flohr T, Brady TJ. Flat-panel CT: fundamental principles, technology & applications. *Radiographics.* 2008;28:2009–22.
112. Smyth JM, Sutton DG, Houston JG. Evaluation of the quality of CT-like images obtained using a commercial flat panel detector system. *Biomed Imaging Interv J.* 2006;2(4):e48.
113. Wallace MJ, Kuo M, Glaiberman C, Binkert CA, Orth RC, Soulez G. Three dimensional C-arm cone-beam CT: applications in the interventional suite. *J Vasc Interv Radiol.* 2008;19:799–813.
114. Miracle AC, Mukherji SK. Conebeam CT of the head and neck, part 1: physical principles. *AJNR Am J Neuroradiol.* 2009;30:1088–95.
115. Orth RC, Wallace MJ, Kuo MD. C-arm cone-beam CT: general principles and technical considerations for use in interventional radiology. *J Vasc Interv Radiol.* 2008;19:814–21.
116. Struffert T, Eyopglu IY, Huttner HB, Engelhorn T, Doelken M, Saake M, Ganslandt O, Doerfler A. Clinical evaluation of flat-panel detector compared with multi-slice computed tomography in 65 patients with acute intracranial haemorrhage: initial results. *J Neurosurg.* 2010;113:901–7.
117. Heran NS, Song JK, Mamba K, Smith W, Niimi Y, Berenstein A. The utility of DynaCT in neurovascular procedures. *AJNR Am J Neuroradiol.* 2006;27:330–2.
118. Kamran M, Nagaraja S, Byrne JV. C-arm flat detector computed tomography: the technique and its application in interventional neuro-radiology. *Neuroradiology.* 2010;52:319–27.
119. Kyriakou Y, Richter DA, Kalendar WA. Neuroradiologic applications with routine C-arm flat panel detector CT: evaluation of patient dose measurements. *AJNR Am J Neuroradiol.* 2008;29:1930–6.
120. Soderman M, Babic D, Homan R, Andersson T. 3D roadmap in neuroangiography: technique and clinical interest. *Neuroradiology.* 2005;47:735–40.
121. Wilhelm K, Babic D. 3D angiography in the interventional clinical routine. *Medicamundi.* 2006;50:24–31.
122. Turski PA, Stieghorst MF, Strother CM, Crummy AB, Lieberman RP, Mistretta CA. Digital subtraction angiography “road map”. *Am J Roentgenol.* 1982;139:1233–4.
123. Racadio JM, Babic D, Homan R, Rampton JW, Patel MN, Racadio JM, Johnson ND. Live 3D guidance in the interventional radiology suite. *Am J Roentgenol.* 2007;189:357–64.
124. Badano A. AAPM/RSNA tutorial on equipment selection: PACS equipment overview. *Display systems.* *Radiographics.* 2004;24(3):879–89.
125. The Royal College of Radiologists. (2008). Picture archiving and communication systems (PACS) and guidelines on diagnostic display devices. This guidance is only available electronically from: [www.rcr.ac.uk](http://www.rcr.ac.uk) (Accessed March 2012).
126. Drost MM. Evaluation of a recently developed 56" monitor in CV interventions. *Medicamundi.* 2009;53(3):24–8.
127. Gurley JC. Flat detectors and new safety aspects of radiation safety. *Cardiol Clin.* 2009;27:385–94.